Western Graduate&PostdoctoralStudies

Western University
Scholarship@Western

Electronic Thesis and Dissertation Repository

1-15-2018 11:00 AM

Development of Force-Space Navigation for Surgical Robotics

Corey Daniel Smith
The University of Western Ontario

Supervisor
Ferreira, Louis M.
The University of Western Ontario

Graduate Program in Biomedical Engineering
A thesis submitted in partial fulfillment of the requirements for the degree in Master of Engineering Science
© Corey Daniel Smith 2018

Follow this and additional works at: https://ir.lib.uwo.ca/etd

 Part of the Biomedical Devices and Instrumentation Commons

Recommended Citation

Smith, Corey Daniel, "Development of Force-Space Navigation for Surgical Robotics" (2018). *Electronic Thesis and Dissertation Repository*. 5177.
https://ir.lib.uwo.ca/etd/5177

This Dissertation/Thesis is brought to you for free and open access by Scholarship@Western. It has been accepted for inclusion in Electronic Thesis and Dissertation Repository by an authorized administrator of Scholarship@Western. For more information, please contact wlswadmin@uwo.ca.

www.manaraa.com

ABSTRACT

Surgical robotics have been used for many years in orthopaedic procedures in the hip and knee. Robots tend to offer high accuracy and repeatability but add increased cost, complexity, time, and workflow disruption. This work outlines the design and development of a surgical robot that navigates using force feedback. Flexible components tether the patient to the robot and reaction loads are measured allowing the robot to "feel" its way around the pre-operative plan. Differences calculated between measured and desired loads are converted to Cartesian corrections that the robot used to navigate. The robot was tested first using simple square paths to test accuracy, repeatability and functionality. A pre-operative plan was established for implantation of the s a surgical setting and allowed the robot to be tested doing a complex glenoid implant path. Finally, a study was performed and compared the robot's surgical method to current surgical techniques of a trained surgical fellow on shoulder analogs. Based on this study, the robot performed as well as or better than the surgeon in almost every measurement parameter with less than 1 mm of implant placement error in many measurement metrics and less than 2° of implant orientation error in each angular measurement.

Keywords: Surgical Robotics, Reaction Forces, Stewart Platform, Load Cell, Surgical Tracking, Force Feedback Navigation.

www.manaraa.com

ACKNOWLEDGMENTS

It has been a great experience working at the HULC with some of the best colleagues that a person could ask for. Working at St. Joseph's Hospital offered a unique and rewarding experience of being able to get both an engineering and clinical perspective that most labs cannot offer.

I would like to first thank my supervisor, Dr. Louis Ferreira for all your help, guidance and knowledge you have given to me. It's been a privilege working for you and helping develop this project further.

Next, I would like to thank Dr. George Athwal for your surgical expertise. The testing could not have happened without your help doing the pre-operative plan, doing the surgical comparison tests and cementing the implants. No hard feels that my robot performed better.

A special thanks to Wright Medical. Wright Medical was crucial in allowing me to use the molds and tooling they previously used to make custom B2 Sawbone models. This saved a lot of time and money necessary for my research. As well, Wright Medical provided the surgical tooling necessary for the surgeon's testing. Thanks to Jenna Beattie who was my contact at Wright and helped organize permission for the sawbone Models and the glenoid tooling. Finally, thanks to Jonathan Tufts from Wright for delivering and setting up of the glenoid tooling for the surgeon's test.

Lastly, big thanks to my family and friends for their continued support.

www.manaraa.com

TABLE OF CONTENTS

www.manaraa.com

www.manaraa.com

www.manaraa.com

www.manaraa.com

LIST OF TABLES

www.manaraa.com

LIST OF FIGURES

www.manaraa.com

www.manaraa.com

www.manaraa.com

www.manaraa.com

CHAPTER 1

1 Introduction

OVERVIEW: *This chapter introduces the background and justification for the surgical navigation system. The relevant anatomy terms needed for this research are introduced. Background on the current robotic surgical systems are described, as well as the current tracking systems being used. Finally, the major components and fundamentals are described and how they are needed for this system.*

1.1 Shoulder Joint

The shoulder joint, also known as the gleno-humeral joint, consists of two major bones: the humerus of the upper arm and the shoulder blade called the scapula. In this joint, the proximal head of the humerus articulates within the socket of the scapula called the glenoid fossa, commonly referred to as the glenoid [1]. For this research the focus was on the glenoid.

When looking at the scapula bone it is important to note that it is not rigidly attached to the structural skeleton. Instead, the scapula is attached through soft tissues allowing for relative movements with respect to the body and as a result, the scapula is referred to as a "floating bone" [2]. The scapula has two main lateral protrusions to note, the acromion and coracoid. The coracoid is the more anterior protrusion while the acromion is more posterior. The main components of the scapula can be seen in Figure 1-1.

www.manaraa.com

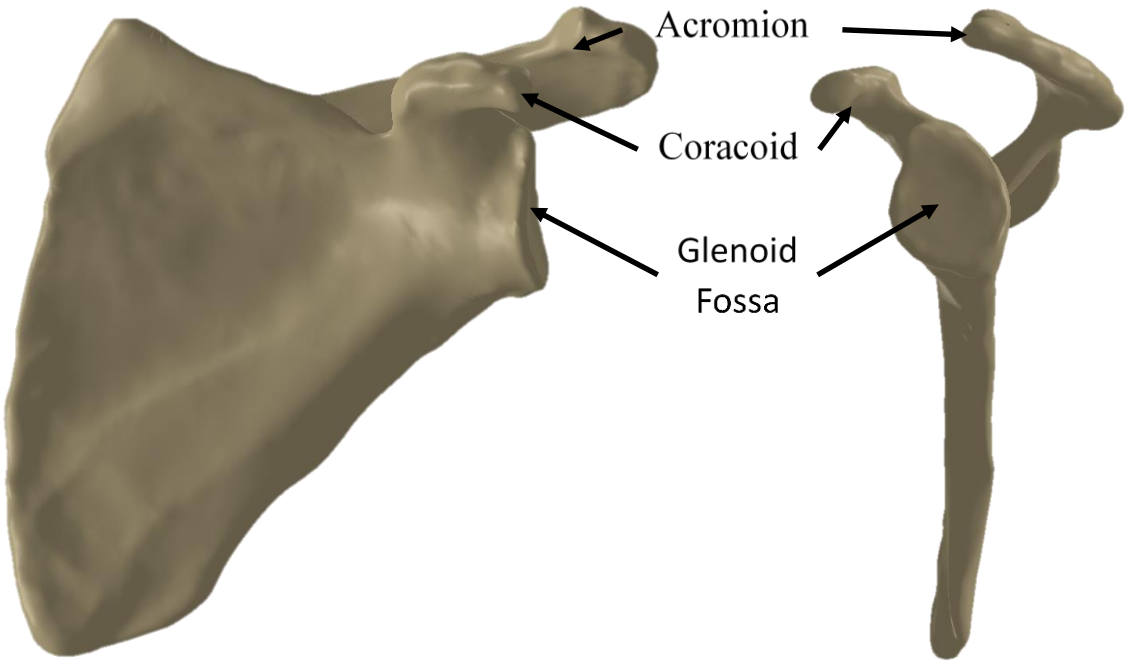

a) Anterior View *b) Lateral View*

Figure 1-1: Left scapula model

1.2 Total Shoulder Arthroplasty

Total shoulder arthroplasty (TSA) surgery involves the replacement of both the proximal head of the humerus and the glenoid with implants. TSA has become a common surgical practice [3] and has been shown to reduce pain and improve the quality of life for patients with arthritis [4]. It is reported that over 90% of TSA operations are successful and with complication rates estimated to be 15 % [5]. Of these complications, a large number of the issues arise from glenoid wear and loosening [6]–[8]. Due to these complications, joint pain and discomfort for the patient can occur and likely a revision surgery is required.

During a TSA, a surgeon manually reams the glenoid with a large spherical tool similar in size to the glenoid. Manual reaming can potentially lead to improper tilt and version of the implant, as well as bone loss from excessive reaming all of which can lead to higher risk of glenoid loosening [9]. Therefore, proper implant placement and fixation in bone is important to reduce the failure of glenoid implants [10].

www.manaraa.com

1.3 Surgical Robotics

Robotic systems have been used in orthopaedics since the 1990s with the goal of improving accuracy and repeatability of surgery [11]. In joint replacement surgeries, proper implant placement is crucial to return the joint to the proper kinematics and loading, to relieve the patient of pain, and limit the need of future revision surgeries. These robotic systems can be classified into three distinct types: passive, active and semi-active [12].

Passive robotic systems complete a prescribed portion of the surgery under direct and continuous control of the surgeon, for example a robot acting like a tool holder. Active robotic systems complete a portion of the surgery autonomously, operating based on the preoperative plan provided by the surgeon. Semi-active robotic systems are controlled by the surgeon while the system provides feedback to help guide the surgeon. These robots are often referred to as collaborative robots. Feedback can come in a variety of forms such as auditory, haptic, visual, etc. This feedback can help surgeons to stay with prescribed volumes or limit bone removal etc.

1.3.1 ROBODOC

The ROBODOC (THINK Surgical, Inc., Fremont, California), (Figure 1-2), was the first orthopaedic robot to be used clinically and first to be approved by the Food and Drug Administration (FDA) in the United States [13], [14]. The system was originally designed for total hip arthroplasty (THA), specifically to mill out a cavity in the femur for the implant. Initially, clinical trials were performed on dogs and eventually progressing to humans in 1992 and these showed the system has an accuracy of 0.4 mm around 10 times better than the conventional procedure [15]. Currently, the system has been used in over 24,000 surgeries [12]. Since then, the ROBODOC has been updated to also perform total knee arthroplasty (TKA) in certain countries. The ROBODOC surgical robot can be seen in Figure 1-2.

www.manaraa.com

Figure 1-2: ROBODOC surgical system[1]

The ROBODOC system consists of 3 major components: the robot arm and stand, the operating room (OR) screen display and the control cabinet [16]. As well, this system has software known as the ORTHODOC system which aids the surgeon in preoperative planning. The robot is 5-axis arm that holds a small, high-speed cutting tool to perform the milling.

A typical procedure using this system will begin with computed tomography (CT) scan of the joint. The CT scan data is then made into a three-dimensional (3D) model that can be used in the ORTHODOC software. In this software the surgeon can manipulate the model, as well as select an appropriate implant from a large database. The surgeon can then virtually fit the implant to the anatomy to create the preoperative plan that will be transferred to the robot. When the surgery is ready to be performed, the patient's leg will be securely fixed in place to the robot. Finally, the robot will mill out the bone autonomously under the supervision of the surgeon based on preoperative plan.

[1] Modified from ROBODOC® [Internet]. THINK® Surgical, Inc., Fremont, CA; cited [December 14, 2017]. Available from http://www.robodoc.com/professionals_howitworks.html.

www.manaraa.com

To locate the patient's bone throughout the surgery, three different methods that have been tested [13]. Originally, the ROBODOC required an additional minor surgery prior to the first CT scan. This surgery involved the placement of fiducials at specified anatomical positions. Typically, three titanium screws are placed into the bone allowing the robot to have points of reference between the patient and the virtual 3D model. The number of screws has since been reduced from three to two in 1998 [13]. However, using this method adds an additional surgery and has been reported in some cases to have pain at the fiducial sites [17]. To help eliminate these issues, a new method was created called shape-based or surface registration. In this method, virtual points are mapped to the CT model. At the start of the surgery the surgeon uses a stylist attached to the robot to map the points and an algorithm relates the points marked by the surgeon to the virtual points. In order for the registration to be accepted the digitized mapping must be within 1 mm of the virtual mapping [18]. Although this method removed the issues of an extra surgery and pain, this increased surgical time by approximately 25 minutes [18]. Finally, the third registration method uses 2D-3D or 3D-3D using intraoperative fluoroscopic images but has only been used in laboratory settings.

Although the ROBODOC has been shown to be highly accurate, it is not without its issues. In general, operating times are typically longer with this system, 25 minutes for TKA [19] and 19 minutes for THA [20]. The size and set-up time is detrimental to the workflow in OR. Finally, the initial cost in 1990 was $635,000 USD and in some cases end users have paid as much as $1.5 million USD for the ROBODOC, ORTHROBOT and all the software which can be difficult to justify versus continuing to perform the conventional manual surgery [12].

1.3.2 Robotic Arm Interactive Orthopedic System

The Robotic Arm Interactive Orthopedic System (RIO), was originally designed by MAKO Surgical Systems and has since been bought out by Stryker Corporation based in Kalamazoo, Michigan. The RIO (Figure 1-3) is a semi-active system designed for uni-compartmental knee arthroplasty, TKA and THA [21]. This system works as a collaborative system along with the surgeon. Like the ROBODOC, this robot requires a CT scan of the patient prior to the surgery. The software creates a 3D model of the patient

www.manaraa.com

which can be used by the surgeon to visualize the anatomy and fit an appropriate size implant and fit to the proper location. This creates the preoperative plan that will be loaded into the robot.

Figure 1-3: Robotic Arm Interactive Orthopedic System for total hip replacement[2]

Before the surgery begins, the surgeon registers bony landmarks of the patient to align the preoperative plan for the robot. As well, stab incisions are required in other areas of the patient, in order to place markers that can be tracked using optical cameras to adjust the cutting volume with movement of the patient [22]. Range-of-motion (ROM) tests are performed just prior to surgery to ensure the registration and tracking is correct. Once that is complete, the surgery will begin. The surgeon can then manipulate the robots tool arm to mill out the predetermined bone volume. As the surgeon performs the surgery, if they were to go near the boundary of the volume, auditory and haptic feedback is provided to

[2] Modified from MAKO Total Hip [Internet]. Stryker® Corporation., Kalamazoo, MI.; cited [December 14, 2017]. Available from https://www.stryker.com/us/en/joint-replacement/systems/mako-total-hip.html

www.manaraa.com

warn the surgeon. If the surgeon goes past these limits, the tool will stop cutting to prevent unnecessary bone removal.

Being a semi-active system, surgeons are more likely to adopt this type of robot as they have more control and input to prevent any unwanted actions from the robot. However, this system is not without its drawbacks. Addition incisions away from the joints are needed to attach the trackers to the anatomy. As well, using optical tracking can highly disrupt the surgical work flow and will be touched upon later in this chapter. The size and setup of this robot also disrupts the workflow in the OR. Finally, this system can cost up to $793,000 USD and additional cost of $140,000 USD for the software which can be a difficult price to justify [11].

1.3.3 NAVIO Surgical System

The NAVIO Surgical system (Smith & Nephew plc, London, UK) is a handheld robotic tool used to perform partial and total knee replacement surgeries. This system has three major components: the milling tool, the surgical display and the tracking camera (Figure 1-4). The tracking camera and surgical display are attached onto a portable cart that can be rolled in and out of the OR and the milling tool is attached to the stand via a power cord. The burring tool has markers that must be visible to the camera to track the tool tip.

www.manaraa.com

Figure 1-4: NAVIO tracking cart (left), burring tool with fiducials (right)[3]

This system requires two trackers to be placed on the patient, one into the tibia and one into the femur; both are about one hand's width away from the knee joint. Once attached, the surgeon runs the patient's knee through ROM tests along with digitize boney landmarks to register the knee joint. Using the landmarks, the surgeon does a surface registration of the tibia and femur with the tool tip to create a virtual model. This model is used to choose an implant and establish a pre-operative (pre-op) cutting plan. Once the plan is created, the surgeon can follow the surgical display to see where the tool tip is with respect to the cut needed and can see a colour map to see the depth of cut needed. The milling tooltip will retract into a sleeve when over an area that does not need to be cut to prevent unnecessary bone removal. Based on early studies the femoral implants were placed with 1.04° to 1.88° rotational mean error and 0.72 to 1.29 mm translational error while the tibial implant was placed with 1.48° to 1.98° rotational mean error and 0.79 to 1.27 mm translation mean error [23].

This system is advantageous in that it does not require pre-op CT scans or planning as imaging and implant fitting are done during the surgery. The surgeon can run the tool over the bone to virtually create the anatomy in the software. As well the surgeon maintains

[3]Modified from NAVIO® Surgical System [Internet]. Smith & Nephew., London, UK; cited [December 15, 2017]. Avaliable from http://www.smith-nephew.com/professional/microsites/navio

www.manaraa.com

control of the tool throughout. However, this system is still relatively large for the OR, it requires line-of-sight for the tracking cameras and additional incisions are needed away from the surgical area to place the bone trackers.

1.3.4 Da Vinci Surgical System

The da Vinci Surgical System (Surgical Intuitive, Inc., Mountain View, CA) was approved by the FDA in 2000. The da Vinci is considered a highly sophisticated surgical robotic system for minimally invasive surgery and has been used in over 1.5 million surgeries in multiple fields including cardiac, colorectal, general surgery, gynecology, head and neck, thoracic and urology [12]. There are three major components: master console, robotic arm cart (slave cart) and a vision display cart in the OR [24]. The system works by having the surgeon working at the master console to control the tools of the slave cart that scales down and mimics the movements of the surgeon. Although, it is important to recognize the da Vinci and its significance in surgery, the system is not a robot in the traditional sense but rather a surgical tool which has been designed for use in soft tissue and suturing procedures and has not been designed for use in orthopaedics.

1.4 Optical Tracking

Optical Tracking is a highly accurate and reliable tracking method and is the most common method used in medical applications [25], [26]. Optical tracking systems consist of two major components: the optical tracking camera and the trackers. The system works by having the camera stand, usual consisting of 2 or 3 cameras, getting a signal from either passive or active trackers to triangulate the position. The position of the trackers is constantly re-sampled at a specific rate to get real-time feedback. For the system to work a constant line-of-sight must be maintained between the markers and the camera. If this line-of-sight is interrupted the system will no longer be able to locate the trackers until line-of-sight is regained. Since a line-of-sight is required at all times, this can be difficult to maintain in a crowded OR and requires a special arrangement of the OR [25].

www.manaraa.com

Active Tracking

Active tracking uses trackers with light emitting diodes (LED) on them. These LEDs emit infrared light which can then be tracked by the optical cameras. These trackers tend to have 3 LEDs that create a virtual plane allowing for translations and rotation measurements. Due to the need for these to be powered, these trackers tend to more expensive and will need to be replaced periodically but last longer than passive trackers.

Passive Tracking

Unlike active trackers, passive trackers are not powered and are typically spheres that reflect an infrared signal back to the cameras. Since these trackers are not powered and just highly reflective spheres they tend to be cheaper but may not be as reliable as active systems as they may not be clean enough to reflect the signal properly and may lead to few or only one use [27]. However, if implemented properly passive trackers can be tracked as accurately as active trackers [27].

1.4.1 Northern Digital Inc.

Northern Digital Inc. (NDI) based in Waterloo, Ontario, Canada, was founded in 1981 and is medical measurement company. Their focus is medical tracking. NDI makes a variety of products primarily different types of optical tracking systems, however there are a few other different tracking method products available. Two of the main optical trackers from NDI are the Polaris and the Optotrak Certus.

Polaris

NDI makes a variety of different products in what they refer to as the “Polaris Family”. The camera mount is relatively small compared to other products with two cameras; one at each end of the mount to locate the trackers. The company states these products are used widely in implant placement, radiation therapy, ergonomic studies, neurosurgery and a variety of other medical applications and is used in over 11,000 surgical applications worldwide. These products have a relatively large working volume, typically small and portable, track either active or passive trackers and are very accurate [27].

www.manaraa.com

Optotrak Certus

The Optotrak Certus (Figure 1-5) is highly accurate, precise and repeatable product that can track up to 512 markers and because of this is often used in research settings [28]. The camera mount is slightly larger than the Polaris system, having 3 cameras; one on each end and one in the middle. The camera setup can be mounted or be on wheels for maneuverability. According to NDI's official website they state this product is in "over 45,000 locations worldwide". A validation study of the system showed the Certus to have high accuracy of 20 µm [29].

Figure 1-5: NDI Optotrak Certus camera

1.4.2 Stryker Navigation System II

Stryker Corporation mentioned earlier, has developed the Stryker Surgical Navigation System II. This system has a display screen and three cameras all on one mobile platform. The Stryker system is used in a variety of medical surgeries such as hip and knee reconstruction, computer assisted surgeries, as well as neuro, cranial and spine surgeries.

1.4.3 BrainLAB

BrainLAB is based in Munich, Germany and have developed two optical tracking system called Kick and Curve. The Kick is a rather sleek design, with the two cameras on a height

www.manaraa.com

adjustable mount on a rolling cart and another cart with the user interface and screen display. The Curve has a similar camera attached to a larger base which has long rotational arm joints for a wide range of camera locations, as well as a second cart with user interface and screen display as well. The BrainLAB was shown in patient marker tests to have 0.3 mm of resolution [30].

1.5 Electromagnetic Tracking

The other main tracking system used in medical applications is electromagnetic (EM) tracking systems. This system consists of two main components: the EM field generator or emitter and the tracked sensor coils. The sensor coils have current sent through them making them into electromagnets. There are three coils in each tracker aligned to create 3 perpendicular directions creating a coordinate system that can be tracked by the EM field generator. These systems can achieve high accuracy in the proper environment of about 0.30 mm ± 0.13 mm [31]. Unlike optical tracking systems, EM systems do not require line-of-sight however EM systems are typically less accurate and can be interfered with by ferromagnetic materials and radio signals [26]. As a result, it can be difficult to justify using EM trackers in an OR with metallic surgical tools.

1.6 Serial Linkage Arm

In many robotic applications, a serial linkage arms can be used (Figure 1-6). These arms require rotary encoders with some distance (i.e. rigid link) between them meaning they are typical not very compact and likely not suitable for a shoulder replacement application [34]. As well, a 6-DOF serial link arms can only represent a specific end-effector pose with a specific configuration of the arm which limits their efficacy for surgical procedures [35]. A seventh axis is commonly added to add redundancy to the system. However, it is unclear how this option could be implemented in a passive serial linked localizer. Without an active motor drive, a localizer without a seventh axis would collapse on itself.

www.manaraa.com

Figure 1-6: Serial linkage arms: Microscribe (left)[4], FARO GAGE arm (right)[5]

1.7 Stewart Platform

A Stewart Platform, also known as a parallel robot, was first designed in 1965 and is a closed-chain mechanism that consists of a fixed base at the bottom and a moving platform at the top with six linear actuators connecting the two components [32]. These six actuators provide 6 degrees-of-freedom (DOF) through the extension and retraction of each actuator. Also, the arrangement and design of the actuators allows the robot to remain rigid and hold position even when no power is going to the motors. This design creates high stiffness, high accuracy, high speed and high loading capacity when compared to a traditional serial linkage robots [32]. As well, parallel robots have a good force-to-weight ratio and position accuracy that surpasses the serial manipulator robots [33]. The strengths of the parallel robot design lend itself to number of applications including flight and vehicle simulators, high precision machining centres, mining machines, medical instruments, etc. [33].

[4] Modified from MicroScribe Portable CMMS [Internet]. GoMeasure3D., Amherst, VA; cited [December 18, 2017]. Available from https://gomeasure3d.com/microscribe/.

[5] Modified from FARO® GAGE [Internet]. FARO Technologies, Inc., Lake Mary, FL; cited [December 18, 2017]. Available from https://www.faro.com/en-gb/products/factory-metrology/faro-gage/.

www.manaraa.com

Figure 1-7: Stewart Platform

1.8 Coordinate System Transformation

1.8.1 Defining Coordinate Systems

A coordinate system is defined by three orthogonal axes and an origin point typically defined by the intersection of the axes. A global coordinate system is a fixed frame of reference that is used to find an object's absolute position and orientation. A local coordinate system is a relative coordinate system that is fixed to an object that will translate and rotate with the object. For example, on the Stewart platform it has a fixed global coordinate system at the base of the robot, while the coordinate system of the platform is a relative system as it translates and rotates with respect to the base coordinate system. These coordinate systems can be seen in Figure 1-8.

www.manaraa.com

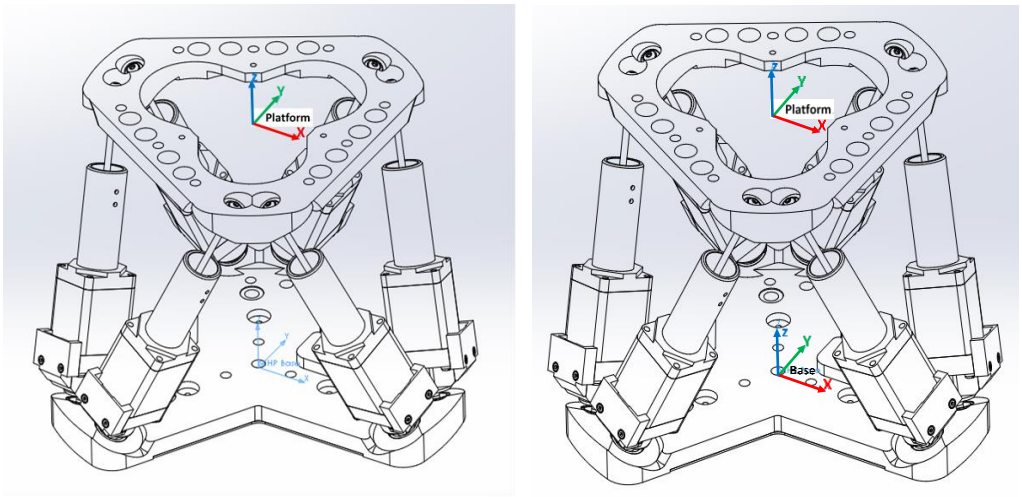

a) Local Coordinate System *b) Global Coordinate System*

Figure 1-8: Local and Global Coordinate Systems

a) Local Coordinate System centred on the top platform, moving in relation to its previous frame of reference. b) Global Coordinate System where the local coordinate system of the upper platform moves with respect to fixed base

1.8.2 Transformation Matrix

To define an object's position in 3D space, a 1 x 3 position vector is used and seen in Eq. (1-1) [36].

$$^{A}P = \begin{bmatrix} p_x \\ p_y \\ p_z \end{bmatrix} \tag{1-1}$$

where ^{A}P is defined as the point relative to coordinate system A.

www.manaraa.com

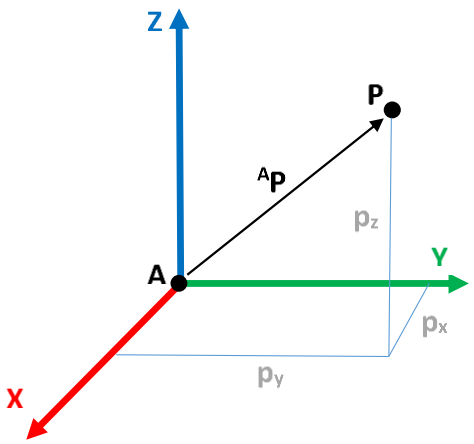

Figure 1-9: Position Vector

To completely define an object in relation to a fixed coordinate system along with the position vector, the object's orientation must also be defined. The object's orientation can be defined by a 3 x 3 rotation matrix, see Eq. (1-2) which defines the rotation of the objects coordinate system (P) with respect to a fixed coordinate system (A).

$$\prescript{A}{P}{\boldsymbol{R}} = [\prescript{A}{}{\hat{\boldsymbol{X}}}_{\boldsymbol{P}} \quad \prescript{A}{}{\hat{\boldsymbol{Y}}}_{\boldsymbol{P}} \quad \prescript{A}{}{\hat{\boldsymbol{Z}}}_{\boldsymbol{P}}] \tag{1-2}$$

where $^{A}X_{P}$, $^{A}Y_{P}$, and $^{A}Z_{P}$ represents the dot product of pairs of unit vectors and their projection onto the unit direction of reference coordinate system see Eq. (1-3).

$$\prescript{A}{P}{\boldsymbol{R}} = \begin{bmatrix} \hat{\boldsymbol{X}}_{\boldsymbol{P}}\hat{\boldsymbol{X}}_{\boldsymbol{A}} & \hat{\boldsymbol{Y}}_{\boldsymbol{P}}\hat{\boldsymbol{X}}_{\boldsymbol{A}} & \hat{\boldsymbol{Z}}_{\boldsymbol{P}}\hat{\boldsymbol{X}}_{\boldsymbol{A}} \\ \hat{\boldsymbol{X}}_{\boldsymbol{P}}\hat{\boldsymbol{Y}}_{\boldsymbol{A}} & \hat{\boldsymbol{Y}}_{\boldsymbol{P}}\hat{\boldsymbol{Y}}_{\boldsymbol{A}} & \hat{\boldsymbol{Z}}_{\boldsymbol{P}}\hat{\boldsymbol{Y}}_{\boldsymbol{A}} \\ \hat{\boldsymbol{X}}_{\boldsymbol{P}}\hat{\boldsymbol{Z}}_{\boldsymbol{A}} & \hat{\boldsymbol{Y}}_{\boldsymbol{P}}\hat{\boldsymbol{Z}}_{\boldsymbol{A}} & \hat{\boldsymbol{Z}}_{\boldsymbol{P}}\hat{\boldsymbol{Z}}_{\boldsymbol{A}} \end{bmatrix} = \begin{bmatrix} \prescript{P_x}{}{\boldsymbol{r}}_{A_x} & \prescript{P_x}{}{\boldsymbol{r}}_{A_y} & \prescript{P_x}{}{\boldsymbol{r}}_{A_z} \\ \prescript{P_y}{}{\boldsymbol{r}}_{A_x} & \prescript{P_y}{}{\boldsymbol{r}}_{A_y} & \prescript{P_y}{}{\boldsymbol{r}}_{A_z} \\ \prescript{P_z}{}{\boldsymbol{r}}_{A_x} & \prescript{P_z}{}{\boldsymbol{r}}_{A_y} & \prescript{P_z}{}{\boldsymbol{r}}_{A_z} \end{bmatrix} \tag{1-3}$$

Now to fully define an objects position and orientation in space, the position vector and rotation matrix are combined into one matrix, along with an extra row to complete a square matrix. This combined matrix is referred to as a transformation matrix in Eq. (1-4).

$$\prescript{A}{P}{\boldsymbol{T}} = \begin{bmatrix} & \prescript{A}{P}{\boldsymbol{R}} & & \prescript{A}{}{\boldsymbol{P}} \\ \boldsymbol{0} & \boldsymbol{0} & \boldsymbol{0} & \boldsymbol{1} \end{bmatrix} = \begin{bmatrix} \prescript{P_x}{}{\boldsymbol{r}}_{A_x} & \prescript{P_x}{}{\boldsymbol{r}}_{A_y} & \prescript{P_x}{}{\boldsymbol{r}}_{A_z} & \boldsymbol{p}_x \\ \prescript{P_y}{}{\boldsymbol{r}}_{A_x} & \prescript{P_y}{}{\boldsymbol{r}}_{A_y} & \prescript{P_y}{}{\boldsymbol{r}}_{A_z} & \boldsymbol{p}_y \\ \prescript{P_z}{}{\boldsymbol{r}}_{A_x} & \prescript{P_z}{}{\boldsymbol{r}}_{A_y} & \prescript{P_z}{}{\boldsymbol{r}}_{A_z} & \boldsymbol{p}_z \\ \boldsymbol{0} & \boldsymbol{0} & \boldsymbol{0} & \boldsymbol{1} \end{bmatrix} \tag{1-4}$$

www.manaraa.com

Using the transformation matrix relation, an objects orientation and location in space can be determined relative to any desired coordinate system. For example, a coordinate system P in relation to a fixed system A in Figure 1-10.

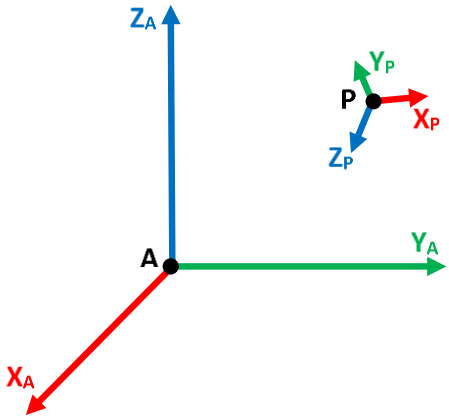

Figure 1-10: Local Coordinate System of Object (P) in Space with Respect to Fixed Coordinate System (A)

1.8.3 Multiple Transformations

In most cases, it is necessary and beneficial to define an object in relation to a specific coordinate system. However, in many of these cases a direct transformation may not be known or may be difficult to calculate directly. For example, in Figure 1-11, there is a cube on a table with a parallel robot.

www.manaraa.com

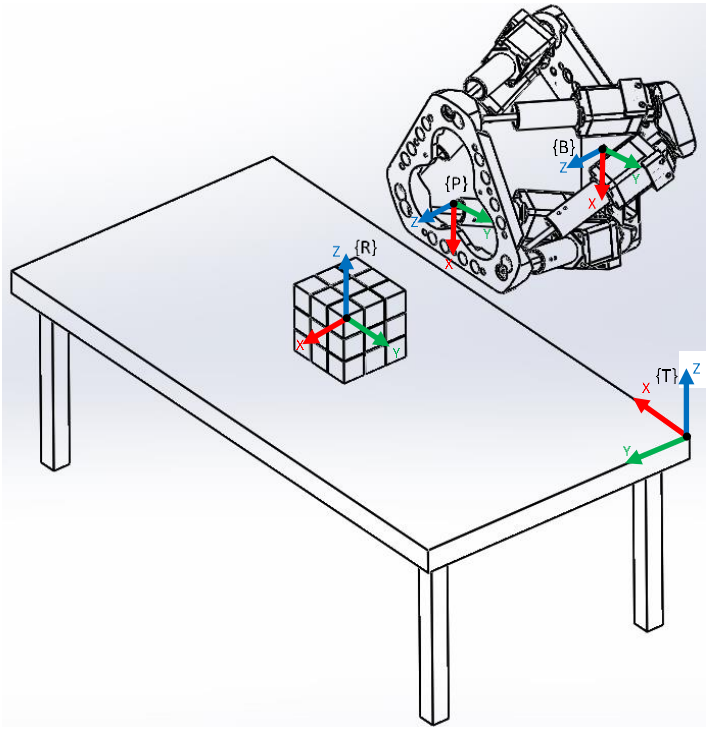

Figure 1-11: Multiple Coordinate System Transformations

{R} Cube coordinate system, {T} Table coordinate system, {P} Platform coordinate System and {B} Robot Base coordinate system which can typically be the global coordinate system

In Figure 1-11, as the platform is moving it may be beneficial to know the robots position compared to an object such as the cube. This requires a relationship to be known between the platform and the cube. A direct relationship may not be easily obtained as the robot is moving. However, one can be found using transformation matrices that describe position and orientation of an object relative to another [36]. In this case, measuring the cube's position on the table can be used. Next a fixed offset between the robot base and the table could be measured based on the components used to fix the robot to the table. Finally, the robot base and platform is easily determined through the robot's own software. Working backwards, and using transforming matrices a relationship can be established. The transformation can be written as follows:

$$\prescript{P}{C}{\boldsymbol{T}} = \prescript{B}{P}{\boldsymbol{T}}^{-1}\prescript{B}{T}{\boldsymbol{T}}\prescript{T}{C}{\boldsymbol{T}} \qquad \textbf{(1-5)}$$

www.manaraa.com

where:

${}^{P}_{R}T$ defines the cube's coordinate system with respect to the platform

${}^{B}_{P}T^{-1}$ defines the base coordinate system with respect to the platform

${}^{B}_{T}T$ defines the table coordinate system with respect to the base

${}^{T}_{R}T$ defines the cube coordinate system with respect to the table

1.9 Load Measuring Techniques

Many techniques exist to measure applied loads in an application, however commercially available load cells are typically the standard instrument used. Load cells are versatile instruments and come in a variety of sizes, shapes, load sensing ranges, resolutions and degrees of freedom in order to suit the user's needs and when implemented properly are highly accurate load sensing devices [37]. A single DOF load cell measures a uniaxial load, a two DOF load cell measures a uniaxial load as well as the corresponding torque about that load vector and a 6 DOF measures three perpendicular forces and the three torques associated with each load vector.

In a 6 DOF load cell, load measurements are reported at the local coordinate system which is typically centred on the top plate as seen in Figure 1-12. However, in many instances it is more beneficial to transform these forces to a point of interest such as a tool tip. A transformation matrix can be used to virtually transform the load cell's coordinate system to any new location.

www.manaraa.com

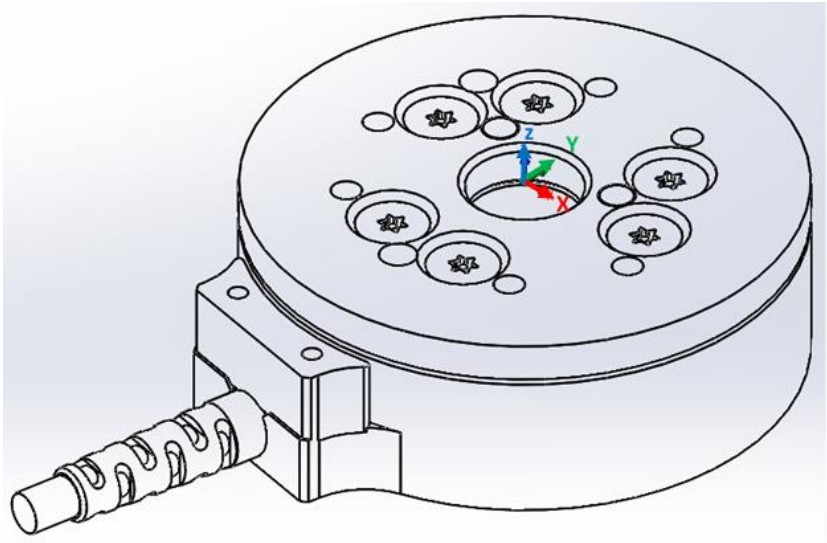

Figure 1-12: 6 DOF ATI Mini45-E Load Cell SI-580-20

Coordinate system for load cell show in the middle of the top plate

To measure loads and torques, load cells use internal strain gauges. These strain gauges measure voltages and these voltages change with different strain. The load cell is sampled at a specified rate in Hertz (Hz). Using proper calibration and transformations, the strain gauge voltages can be converted to forces and torques. It is important to note; the load cell is grounded and the strain gauges are shielded by the metal exterior that acts like a Faraday cage to protect against signal interference that could skew the data.

1.10 Rationale

The current surgical robotic systems that are available typically use optical tracking for navigation. However, these systems tend to have a low adoption rate by surgeons, which can be attributed to a few main reasons:

1. These robotic systems are typically very expensive and can cost in the hundreds of thousands even millions of dollars in some cases. The optical tracking system alone is generally over $70,000. The trackers, whether they are optical or EM need to be sterilized, maintained, inventoried and replaced from time to time, which adds cost and complexity. This reduces their suitability for most surgical centres.

www.manaraa.com

2. Optical trackers require a direct line-of-sight between the tracker and the camera, which is typically located 2 to 3 metres from the surgical field. This is obtrusive for most orthopaedic surgeries, which involve at least three staff working closely around the patient. Thus, adoption of these systems requires significant retraining and alteration of surgical workflows.

3. These robots are typically large industrial size serial link arms with excessively large ranges of motion. The robots are typically on a cart that needs to be rolled in and out of the OR along with the tracking cameras that need to be stored. The size and setup can be very disruptive to the OR workflow. Since they are floor-mounted, they require a large range of motion to bring the end-effector to within the surgical field.

These issues stem largely from the fact that current surgical robots use tracking systems that were designed for general purpose tracking, such as gait analysis. The robot controller is simply augmented with the tracking system. A navigated robotic system that is specifically designed for orthopaedic procedures is required. Ideally, it should be inexpensive, does not rely on optical tracking, be more compact robot and easier to maneuver, and limit OR setup time as much as possible. This dissertation will show the development of a new tracking system that is implemented onto a Stewart platform which will be tested in shoulder replacement procedures but could be use in a variety of surgical applications. The tracking system will not rely on optical or EM tracking. Instead load feedback will be used to navigate and a Stewart platform that will provide the actuation of the tool.

This navigation system uses a flexible component tethering the robot to the patient. This tethering allows for reaction forces and torques to propagate to the robot allowing it to "feel" its way around the programmed path in a "force space". The robot tries to maintain the proper orientation and position with the robot and will "feel" if the patient moves and compensate accordingly. This is especially important with the shoulder replacement surgery since the scapula is a float bone supported by soft tissues and can move if loaded.

www.manaraa.com

The purpose of this paper is to validate the flexible mount surgical navigation through glenoid reaming procedures.

1.11 Objectives and Hypotheses

The purpose of this work is to develop and test a flexible component navigation method that utilizes reaction forces and torques. This navigation method is paired with a 6-DOF Stewart platform as the main form of actuation. Although this navigation system will be used along with the platform robot, this is for testing and validation purposes. In theory this navigation system can be used on a variety of robots or even attached directly to a handheld tool. As well, even though the main testing will be related to shoulder replacement surgery, this navigation system can be employed for a multitude of applications.

Objectives

1. To develop reaction force and torque navigation system;
2. To design a patient specific mount that will allow for easy attachment to the patient and registration of a surgical pre-operative plan;
3. To test and validate the system using a total shoulder arthroplasty model.

Hypotheses

The navigation system will have displacement errors of the end-effector less than 2 mm, which is suitable for orthopaedic procedures. Additionally, the complete surgical robot prototype will demonstrate statistically better accuracy than a surgeon.

1.12 Thesis Overview

Chapter 2: describes the development of the force-space navigation. This includes the development of the control algorithm, as well as the setup and design of the hardware of the system. Simple milling paths are analyzed to validate the accuracy of the navigation system.

Chapter 3: describes the surgical path planning protocol that was used in the surgical force-space navigation. This includes generating the milling path based off the computer-aided

www.manaraa.com

design (CAD) model of a chosen implant. Testing was done in the open air and in Sawbone blocks, as well as the inclusion of a flexible Sawbone mount to simulate the floating motion of a scapula bone.

Chapter 4: describes the application of the force-space navigation robot in a shoulder analog. This includes following the pre-op plan laid out in Chapter 3 and implement this on the scapula models. As well, 3D printed patient-specific mounts were printed from the CT data to allow for registration of the path. Comparisons of the tests were made using post-operative (post-op) CT scans.

Chapter 5: describes the implications and conclusions of this work and describes the future worked needed to progress this work further.

www.manaraa.com

CHAPTER 2

2 Development of a Force-Space Navigation Robot for Glenoid Arthroplasty and Resurfacing

OVERVIEW: *This chapter goes through the design of the system and simple path testing. The design includes the hardware of the system: Stewart Platform, load cell, positioning arm, etc. The software design is also discussed including the control algorithm. Finally, the system was tested by using simple planned paths.*

2.1 Experimental Apparatus

2.1.1 Tool and Flexible Component Assembly

The tool and flexible component setup can be seen in Figure 2-1. The main component of the system is a Stewart Platform which is a Mini Hexapod Platform also referred to as MHP-11 (Picard Industries Albion, New York). All the main components are attached to this robot. The major components include:

www.manaraa.com

1) Flexible components (Wear-Resistant 304 Spring Steel)

2) Brass mounting brackets to load cell and robot

3) Midas Rex Stylus (Medtronic Inc. Minneapolis, Minnesota) bone burring tool

4) Mini45-E Load Cell SI-580-20 (ATI Advanced Industries, Markham, Ontario)

5) Brass mounting brackets to the patient mount

6) Tool mount holder

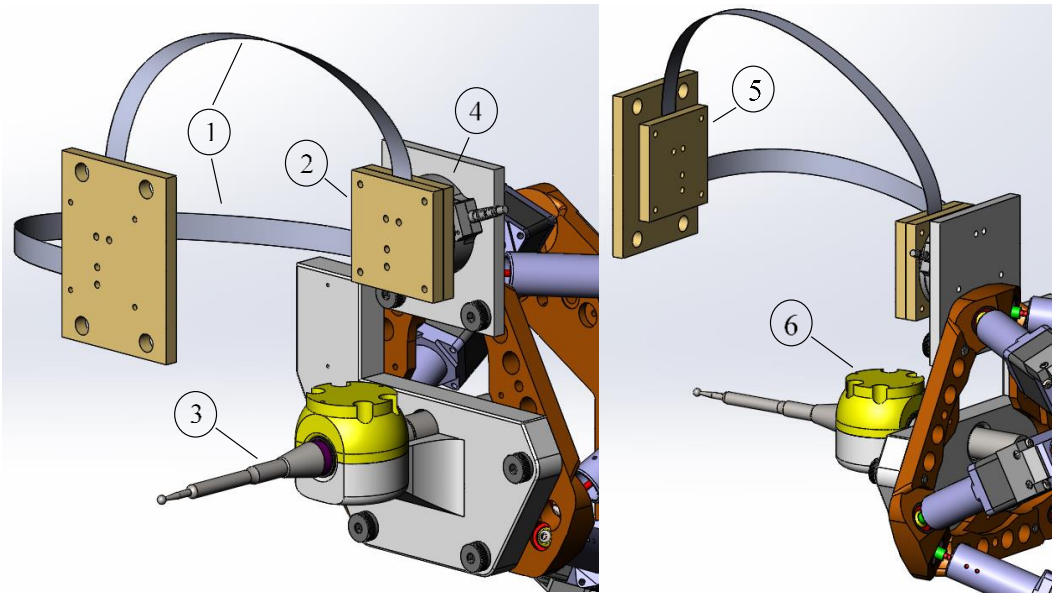

Figure 2-1: Flexible Component and Tool Assembly

2.1.2 Positioning Arm

The robot's range of motion is large enough for the surgical field, but not large enough to provide gross positioning. For this, a Spider2 Limb Positioner (Smith & Nephew Inc., Andover, Massachusetts) was selected (Figure 2-2). The Spider2 is used regularly in orthopaedic operating rooms to hold a patient's limb in place. It is easily unlocked and repositioned with a quick release foot pedal. As well, this device easily attaches to a standard OR table railing and is a normal part of surgical staff training and workflow.

www.manaraa.com

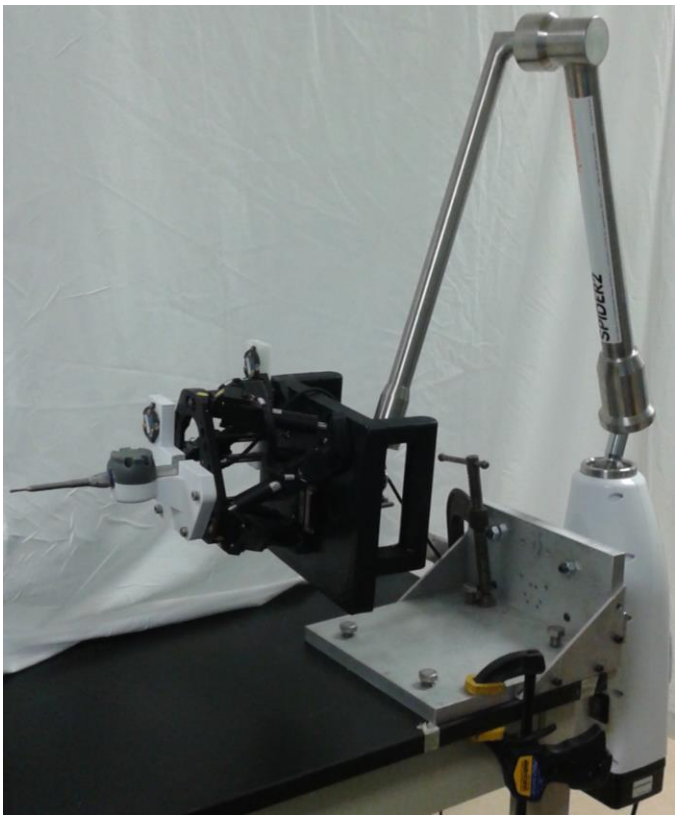

Figure 2-2: Spider2 limb positioning arm (Smith & Nephew Inc., Andover, Massachusetts) with robot attached.

2.1 Coordinate System Transformations

2.1.1 Force-Space Transformation

The flexible strips tether the robot to the object being machined. This system works by converting Cartesian coordinates into forces and torques measured by a 6-DOF load cell via the reaction forces that are transmitted through the flexible strips as the robot moves relative to the machined object [38]. To accomplish this, both the robot's Cartesian coordinate system and the load cell's coordinate system were aligned and transformed to the tool tip (Figure 2-3). With the coordinate systems aligned, path control points in Cartesian Space can be transformed into load values, in what will be referred to as the "force space". This means that a specific point in the robot's Cartesian space, which requires a specific pose of the robot (i.e., X, Y, Z, Rx, Ry, Rz) is converted to forces and torques (Fx, Fy, Fz, Tx, Ty, Tz). Since both the robot's Cartesian and Force-Space

www.manaraa.com

coordinate systems are aligned, then corrections in forces and torques made to navigate the robot, can easily be converted back into corrective displacements and rotations for the robot's positioning commands.

Virtually aligning the robot's programmable coordinate system with the load cell's measurement reference frame simplifies the rigid body transformation algebra. This is because eliminating offsets between the force feedback system and the Cartesian position control output also eliminates moment arms which would otherwise conflate displacements into torque components and vice-versa. The complete coordinate system transformations are illustrated in Figure 2-3.

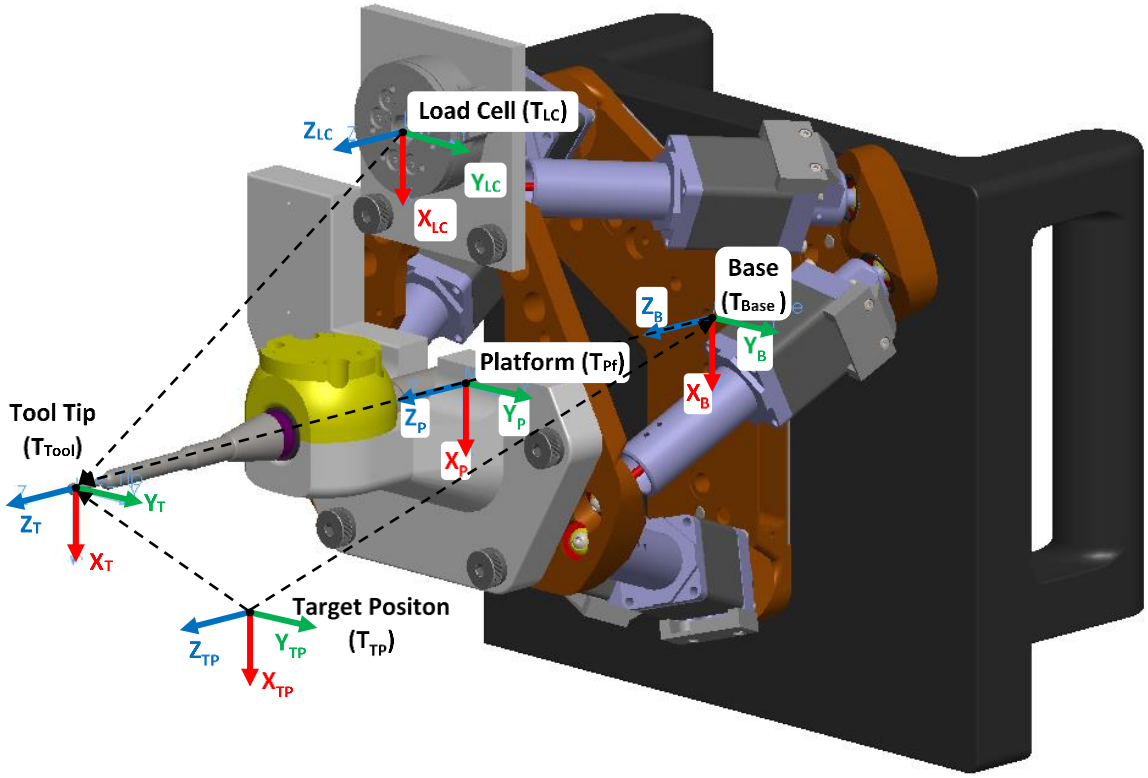

Figure 2-3: Coordinate system transformations to the tool tip

2.1.2 Tool Cartesian Coordinate Transformation

The Stewart platform had two main Cartesian coordinate systems. First there was the fixed frame of reference known as the base coordinate system. The origin of this coordinate system was located on top of the base plate centred at the middle hole with the z-axis

www.manaraa.com

normal to plate. The next frame of reference was the platform. This coordinate system was moveable based on the extensions and retractions of each stepper motor. This coordinate system was in the centre of the top platform with the z-axis normal to the platform. For the position and orientation information to be useful, a further transformation was needed to the tool tip. To simplify the transformations, the mount for the bone burring tool was designed so that the tool's long axis was collinear with the z-axis of the platform. As well, the tool orientation of the x and y axes were not crucial and was therefore aligned with the platforms x and y axes. This eliminated the need for any rotational transformations between the tool and platform. As a result, the only transformation needed was an offset in the z direction.

$$ {}^{Tool}_{TP}\boldsymbol{T} = {}^{Tool}_{Pf}\boldsymbol{T} \times {}^{Pf}_{Base}\boldsymbol{T} \times {}^{Base}_{TP}\boldsymbol{T} \quad \textbf{(2-1)} $$

${}^{Tool}_{TP}\boldsymbol{T}$ = Target Position with respect to Tool Coordinate System

${}^{Tool}_{Pf}\boldsymbol{T}$ = Robot Platform with respect to Tool Coordinate System

${}^{Pf}_{Base}\boldsymbol{T}$ = Robot Base with respect to Robot Platform

${}^{Base}_{TP}\boldsymbol{T}$ = Target Position with respect to Robot Base

2.1.3 Load Cell Coordinate Transformation

The load cell coordinate system was also transformed to the tool tip. The load cell's coordinate system was centred on top face of the load cell, with the z-axis normal to the face. To simplify transformations, the load cell was mounted to the robot's moveable platform such that its axes were orientated parallel to the robot's base coordinate system, meaning that no rotational transformations were needed. As well, the X-Z plane of the load cell and tool were parallel, meaning that only offsets in the X and Z directions were needed.

$$ {}^{Tool}_{ML}\boldsymbol{T} = {}^{Tool}_{LC}\boldsymbol{T} \times {}^{LC}_{ML}\boldsymbol{T} \quad \textbf{(2-2)} $$

${}^{Tool}_{ML}\boldsymbol{T}$ = Measured Load with respect to the Tool Coordinate System

${}^{Tool}_{LC}\boldsymbol{T}$ = Load Cell with respect to Tool Coordinate System

www.manaraa.com

$\boldsymbol{^{LC}_{ML}T}$ = Measured Load with respect to Load Cell

By transforming the load cell coordinate system to the tool tip, it is as though the navigation reaction loads via the flexible metal strips are occurring at the tool tip. This eliminates several coordinate transformations to align navigation loads to robot direction commands. Note that the burring tool is not mounted to the load cell, which means that the navigation loads are isolated from machining dynamics from the bone burring process.

2.2 Control System

2.2.1 Robot Position Controller

The Stewart platform robot uses stepper motors, which operate in an open-loop control. The load cell provides navigation feedback in the force space, and thus is used in this system to close the Cartesian space control loop. Errors in load cell measurements are converted to translation corrections for the robot. The full algorithm will be discussed further in this chapter. The control loop diagram can be seen in Figure 2-4. The proportional term Kp is a 6-term vector of scalars for the six directions that convert between Force-Space (Fx, Fy, Fz, Tx, Ty, Tz) and Cartesian positioning space (X, Y, Z, Rx, Ry, Rz) [39]. The scalars were specifically (4, 4, 4, 5, 5, 5).

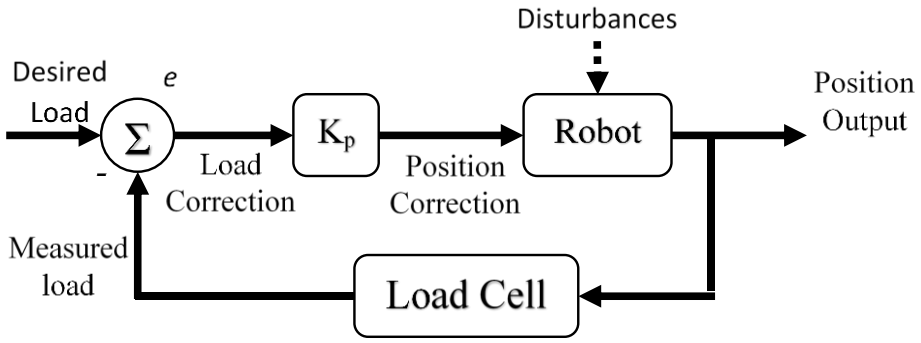

Figure 2-4: Robot Position Controller. It is based on a closed-loop proportional control design.

www.manaraa.com

2.3 Force-Space Calibration

Calibration involves converting a planned pathway in Cartesian space into a load pathway, which is a list of forces and torques that the force-space controller will target in real-time. The load pathway is simply the reaction forces transmitted by the flexible strips to the load cell (transformed to the tool tip as described previously). A computational method for generating the force-space load path has not yet been developed. Currently, system calibration is achieved by commanding the robot to move in the planned Cartesian space while recording the reaction forces with the flexible strips fixed relative to the robot's base frame. This is achieved by clamping the robot's base to a table and fixing the flexible strips relative to the table (Figure 2-5).

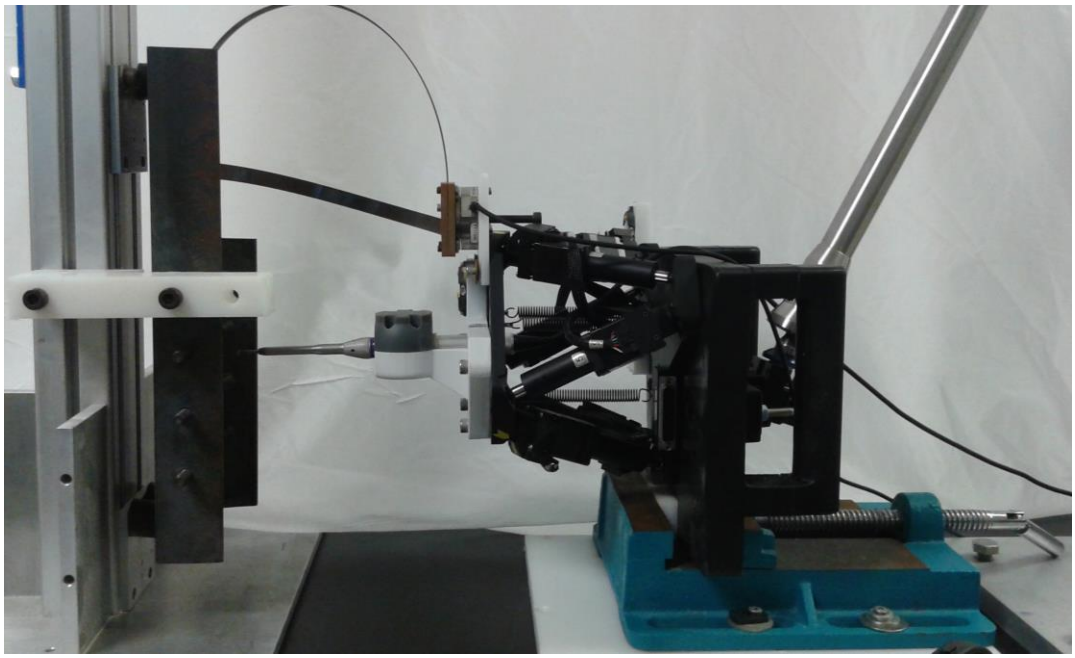

Figure 2-5: Robot clamped and tether to the post in preparation for calibration.

Of course, the planned Cartesian path coordinates are relative to the specimen rather than a global frame, and so it follows that the forces are also relative to the specimen. In practice, the planned Cartesian pathway is broken into control points less than 1 mm apart. During calibration, the robot is commanded to move to each of these point locations, where it stops while loads are recorded. The step by step process from Cartesian path to load path is illustrated in a flowchart (Figure 2-6).

www.manaraa.com

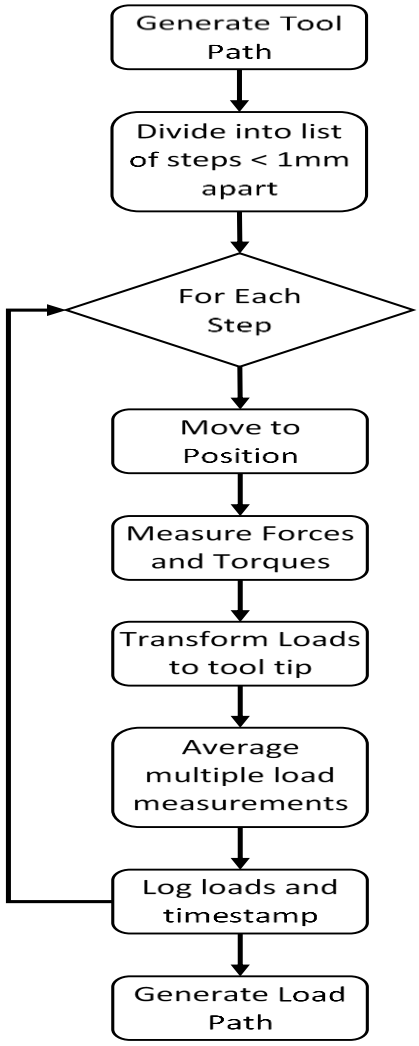

Figure 2-6: Calibration Algorithm Block Diagram

Shows the steps for generating the navigation load path from a Cartesian coordinate input path.

Once calibrated, during normal operation the robot is mounted to the Spider2 positioning arm which is not rigid, and the specimen is also not rigidly mounted. Thus, the force-space controller must correct the force-space path in real-time to compensate for unanticipated movements by minimizing errors in the relative load path targets. This type of unanticipated movement is sure to occur in a surgical application, since patient anatomy cannot generally be fixed, and given that the reaction forces from the flexible strips will surely move the anatomy. Chapter 3 describes how this calibration method can be incorporated into a surgical plan.

www.manaraa.com

2.4 Performance Evaluations

2.4.1 Robot Controller

With the load path generated, the system can be run in force-space control mode. At this point the robot is manually positioned in generally the correct starting location using the Spider2 positioning arm. The specimen being machined and the robot's mount are not fixed as they were during calibration of the relative load pathway; rather, the force-space controller corrects for any unanticipated movements of the specimen or robot by minimizing the load errors, and thus minimizing the positioning errors. In a load path navigation file, each row consists of the Fx, Fy, Fz, Tx, Ty, and Tz corresponding to the control points. The robot's controller seeks to minimize the load errors at a control point to within a threshold of ±0.1 N, ±0.1 N, ±0.07 N for Fx, Fy and Fz respectively and ±0.007 N·m for Tx, Ty and Tz before moving onto the next control point. In this way, the force-space controller simultaneously achieves both the tasks of planned path navigation and disturbance correction.

2.4.2 Pilot Cartesian Path Testing

To preliminary test the robot, a simple square path was used. The robot was attached to a fixed post for ease of testing. First, to test the repeatability of the load cell and the calibration phase, a path of three orthogonal lines following each axis was used. Each direction was different in length and the X and Z directions move in the positive direction, while the Y direction moves in the negative direction. By moving in all three axes and in both positive and negative directions, it shows the broader capabilities of the robot. The planned path was to first move +5 mm in the X direction followed by -10mm in the Y direction and finishing with +3 mm in the Z direction. Each of these linear paths were broken into 1 mm steps for the correction factors needed between points would be relative small so that the robot will not have been error correction steps while in load control. The planned path X, Y, and Z coordinates and the graphed path can be seen in Figure 2-7. This path was performed 10 times to get 10 corresponding load paths.

www.manaraa.com

	$\vec{P}$ (mm)		
Point	**X**	**Y**	**Z**
0	0	0	0
1	1	0	0
2	2	0	0
3	3	0	0
4	4	0	0
5	5	0	0
6	5	-1	0
7	5	-2	0
8	5	-3	0
9	5	-4	0
10	5	-5	0
11	5	-6	0
12	5	-7	0
13	5	-8	0
14	5	-9	0
15	5	-10	0
16	5	-10	1
17	5	-10	2
18	5	-10	3

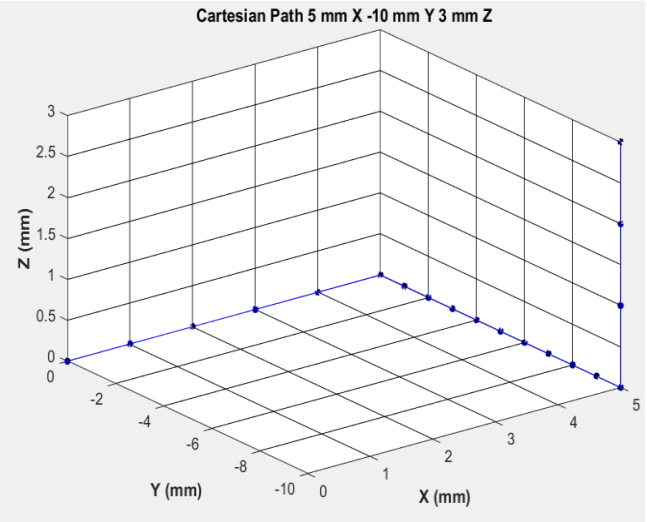

Figure 2-7: Example Cartesian path moving in 1 mm steps 5mm in X then -10 mm in Y and 3 mm in Z

X, Y, and Z coordinates (left) and shown graphically (right)

2.4.3 Results and Discussion

Once the 10 calibration paths were completed, 10 load paths were generated. The load paths were averaged and standard deviations recorded (Table 2-1). The main purpose of these calibrations was to test the repeatability of the load cell and the resulting load paths. It is important that the calibrations are consistent and create a unique load path or else when in load control the robot will not behave in a predictable manner.

www.manaraa.com

Table 2-1: Reaction Load Values Corresponding to the Cartesian Path

	Mean Load						Standard Deviation					
Point	Fx (N)	Fy (N)	Fz (N)	Tx (N·m)	Ty (N·m)	Tz (N·m)	Fx (N)	Fy (N)	Fz (N)	Tx (N·m)	Ty (N·m)	Tz (N·m)
0	0.007	0.021	0.119	0.003	0.010	-0.003	0.045	0.032	0.185	0.005	0.016	0.004
1	-0.431	-0.008	0.157	0.002	0.044	-0.048	0.046	0.033	0.185	0.006	0.017	0.004
2	-0.874	-0.028	0.202	0.003	0.079	-0.094	0.044	0.033	0.204	0.006	0.019	0.004
3	-1.312	-0.054	0.267	0.003	0.115	-0.139	0.042	0.031	0.218	0.005	0.019	0.004
4	-1.762	-0.078	0.326	0.003	0.153	-0.184	0.044	0.030	0.196	0.005	0.018	0.004
5	-2.197	-0.109	0.343	0.003	0.183	-0.228	0.044	0.031	0.212	0.005	0.019	0.004
6	-2.147	0.188	0.369	0.012	0.183	-0.300	0.041	0.032	0.206	0.005	0.018	0.004
7	-2.091	0.488	0.406	0.022	0.182	-0.372	0.044	0.030	0.204	0.005	0.017	0.004
8	-2.042	0.774	0.420	0.030	0.181	-0.442	0.043	0.031	0.200	0.005	0.018	0.004
9	-1.992	1.067	0.453	0.039	0.181	-0.513	0.044	0.034	0.215	0.006	0.018	0.004
10	-1.939	1.352	0.480	0.046	0.179	-0.582	0.043	0.035	0.195	0.006	0.017	0.004
11	-1.886	1.634	0.510	0.053	0.178	-0.651	0.045	0.034	0.202	0.006	0.018	0.004
12	-1.830	1.916	0.539	0.061	0.177	-0.719	0.045	0.034	0.215	0.006	0.018	0.005
13	-1.774	2.197	0.569	0.068	0.175	-0.787	0.044	0.034	0.199	0.006	0.018	0.004
14	-1.710	2.482	0.611	0.075	0.173	-0.856	0.045	0.033	0.202	0.006	0.018	0.004
15	-1.659	2.756	0.641	0.081	0.172	-0.922	0.047	0.032	0.213	0.005	0.020	0.005
16	-1.611	2.770	-0.002	0.116	0.088	-0.919	0.048	0.036	0.212	0.006	0.019	0.005
17	-1.562	2.787	-0.632	0.150	0.004	-0.916	0.046	0.033	0.198	0.005	0.018	0.005
18	-1.526	2.799	-1.236	0.184	-0.075	-0.913	0.046	0.035	0.194	0.006	0.018	0.005

The standard deviations were all relatively low with the maximum being 0.218 N in Z. The Fx standard deviations averaged 0.045 N while Fy standard deviations averaged 0.033 N. Since this load has resolution of 1/25 N for Fx and Fy values, this means that error was within the load cell's specifications. Fz standard deviations were higher averaging 0.203 N. Although the resolution of Fz is rated to 1/25 N, Fz has a higher sensing range which typically means larger variations in measurements can occur. Similar results occurred in the torque measurements where the standard deviations of each Tx, Ty and Tz were at or near the load cells resolution.

The results of this test indicate that only one calibration run is needed for a reliable load path to be generated.

www.manaraa.com

2.5 Load Control Navigation Testing

2.5.1 Testing Setup

To test the load control algorithm, a simple 10 mm square path was used for initial assessment. The Cartesian path was centred at the tool tip. The coordinate sequence was (5,5,0) then to (-5,5,0), (-5,-5,0), (5,-5,0) and back to (5,5,0) as illustrated in Figure 2-8.

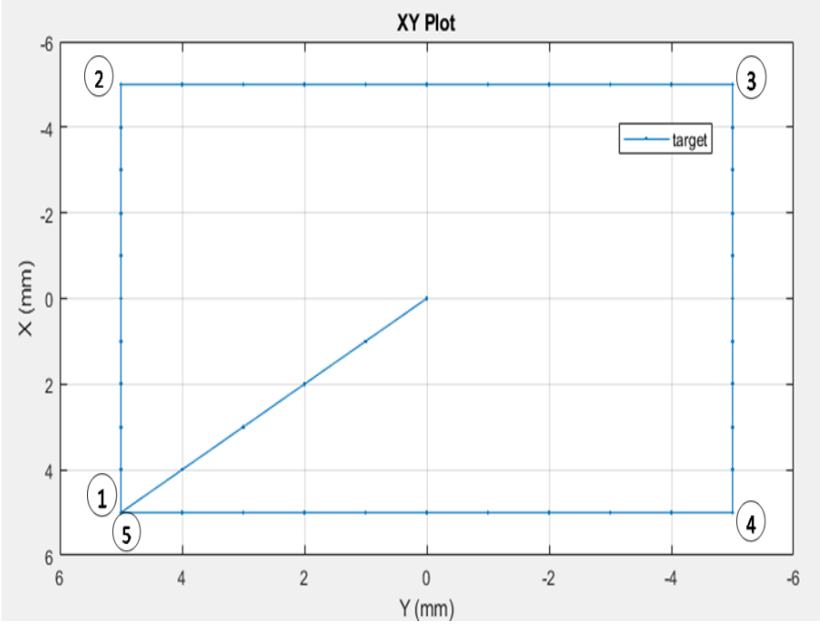

Figure 2-8: 10 mm Square Cartesian Path in XY-Plane. Control points are in 1 mm increments.

While this was a 2D square path, it was still controlled in 3D, and so a 3D performance assessment was quantified.

2.5.2 Load Control Results

Throughout both the calibration and load control runs, an Optotrak Certus was used as a gold standard for comparison [28]. One optical tracker was placed on the fixed post, while another was placed on the moving platform of the robot. The post tracker was used as a fixed frame of reference, while the platform's tracker was transformed to the tool tip. Five load control runs of the square path were performed. The Certus data for both a calibration run and load control run are shown in Figure 2-9.

www.manaraa.com

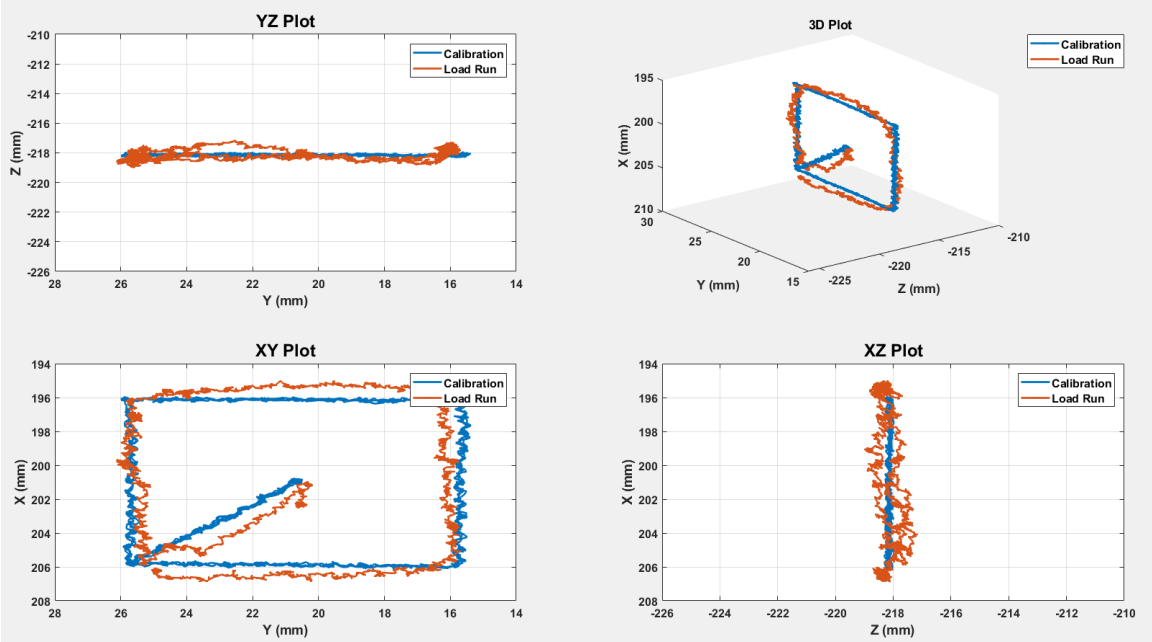

Figure 2-9: Example of Calibration Run (Blue) vs. Load Control Run (Orange)

To analyze the data, five points of interest were isolated, including all four corners and the first corner at the start and end of the run. Absolute values of X, Y and Z for each of the 5 points were averaged. This was done to prevent positive and negative terms skewing the data. The results are summarized in Figure 2-10.

www.manaraa.com

Figure 2-10: Mean position errors from the square path from Figure 2-8 where points correspond to corners and points 1 and 5 are the same.

From the load control tests, it was shown that the system had high accuracy for all points of interest. Across the five points, in the X direction showed an absolute average error of 0.14 ± 0.19 mm with the maximum error being 0.75 mm and the minimum be -0.82 mm. In the Y direction the absolute average error was 0.31 ± 0.34 mm with the maximum error being 2.01 mm and the minimum error was -1.25 mm. Finally, in the Z direction the absolute average error was 0.19 ± 0.22 mm with the maximum error being 0.52 mm and the minimum error was -1.03 mm. Overall, this mean an average Euclidean error of 0.41 ± 0.46 mm.

2.6 Discussion

Based on the data, the robotic system showed suitable accuracy and repeatability for an orthopaedic procedure. Although the entire path between corner points was not examined in detail, all paths were plotted and no anomalies or straying off course was observed since control points between the corners were used. All three directions showed relatively similar performances with X and Z being slightly better than Y.

www.manaraa.com

The effect of the load cell transformation to the tool was emphasized using a glenoid implant path (Figure 3-7) which will be discussed in more detail in Chapter 3. Figure 2-11 shows the forces measured during a glenoid path calibration of transformed and untransformed load cell coordinate system. Similarly, Figure 2-12 shows the measured torques from the same glenoid path. The linear forces were relatively unchanged which make sense as the coordinate system was only translated and not rotated. The torques were vastly different which shows the importance of aligning the load cell coordinate system and the tool tip coordinate system.

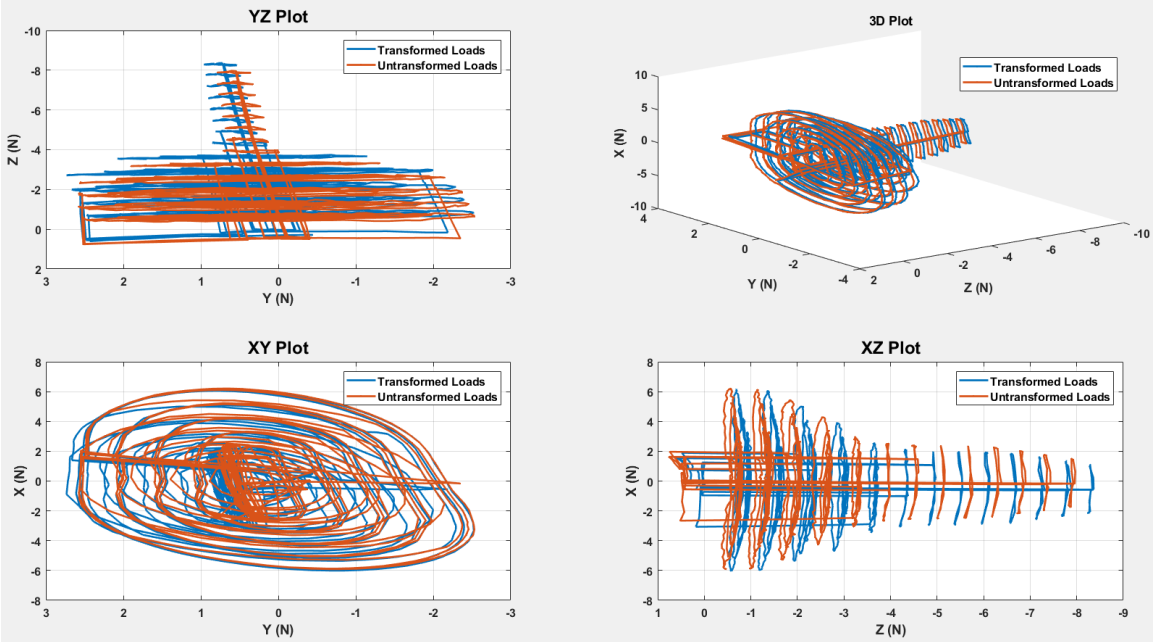

Figure 2-11: Forces transformed and untransformed load cell coordinate system

www.manaraa.com

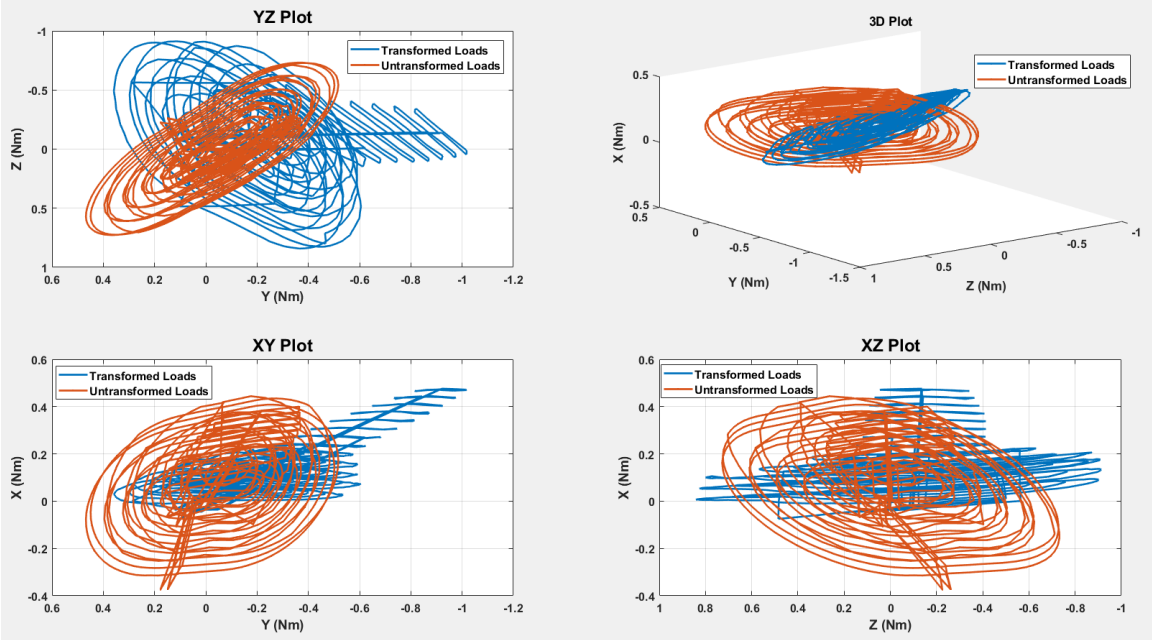

Figure 2-12: Torques transformed and untransformed load cell coordinate system

2.7 Chapter Summary

The design of the system used a Stewart Platform as the main form of actuation. Flexible components tethered the robot to a fixed post for the purposes of testing and translated reaction forces and torques between the post and robot. The reaction loads were measured by the load cell and used later as tracking and navigation feedback.

The system worked by first generating a load path in the calibration phase. These loads were transformed to the tool tip to align both the Cartesian coordinates and force space coordinates. The calibration phase moved in Cartesian space while measuring reaction loads at control points. Calibration path proved to be highly repeatable and showed a consistent load path. As a result, multiple calibration runs are not needed for future testing in load control.

After the reliability of the calibration process was validated, load control testing was performed. To test the load control navigation method, a simple square shape was used. The corner points of the square where analyzed to determine the accuracy and repeatability of the system. The load control method proved to be highly accurate and repeatable with

www.manaraa.com

Euclidean error of 0.41 ± 0.46 mm. This validated this system as a reliable navigation method and allowed for more testing to continue. The next stages of testing include testing more complex paths, creating paths from glenoid implants and adapting the system for human scapula analog models which will be explored in future chapters.

www.manaraa.com

CHAPTER 3

3 Development of a Surgical Path Planning Protocol for Surgical Force-Space Navigation

OVERVIEW: *This chapter presents the process developed to apply the Force-Space Navigation method to a shoulder arthroplasty procedure. The workflow is described, beginning with a patient's diagnostic CT scan.*

3.1 Pre-Operative Planning

Along with the newly developed robotic surgical system, a step by step procedure was developed to take a scapula and create the force-space navigation path that would be used to create the glenoid implant cavity. The pre-op plan steps include:

1. Create 3D scapula model from scan
2. Virtually place implant onto scapula model
3. Design and 3D print patient specific mount for flexible components
4. Generate Cartesian path based on the implant placement
5. Generate the force-space path (i.e. Calibration)
6. Perform force-space navigation

3.2 Scapula Model

For the pilot studies of the robot doing complex paths, a scapula model from Sawbones® (Vashon Island, WA, USA) was used. The model was of a left shoulder with a hard-outer layer to mimic cortical and subchondral bone, and a soft foam interior to mimic trabecular bone. The sawbone model was then reverse-engineered by laser scanning (Space Spider,

www.manaraa.com

Artec3D, Santa Clara, CA) (Figure 1-1) [40]. For patients, CT scans would be used to create a similar 3D scapula model. CT scans are already done prior to these procedures and would not add any additional costs.

Figure 3-1: Normal Shoulder Sawbone Model

3.3 Implant Placement

Once the scapula model was created, a trained surgeon selected an appropriate implant for the anatomy. A small AEQUALIS™ PERFORM keeled glenoid implant with a 30 mm radius from Wright Medical was chosen. The surgeon virtually placed the implant in the appropriate anatomical position. The implant position can be seen in Figure 3-2.

www.manaraa.com

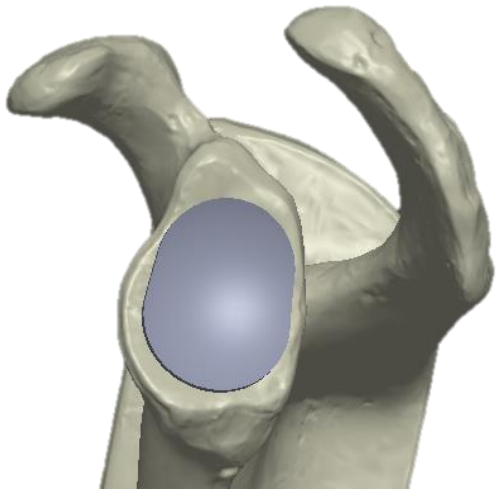

Figure 3-2: Virtual Implant Placement.

Pre-operatively, a surgeon plans and confirms placement of the implant.

3.4 Patient Specific Mount

3.4.1 Scapula Mount

Next, a mount was designed to secure to the scapula model. This mount served as a location to attach the flexible components; tethering the scapula model and the robot. The mount was designed to have an upright portion that allowed for the flexible mount bracket to be attached. As well, pedestals were aligned to a point near the lateral end of the acromion and two points along the coracoid. The pedestals were hollow and allowed for bones screws to go through them screwing the mount to the model.

The scapula model was then Boolean subtracted from the patient specific mount. The subtraction creates a mount that was shaped to fit directly onto the scapula model. This process can be adapted to any patient's CT scan to allow for patient specific mounts. This component was 3D printed for simplicity, cost and fast prototyping. The model was printed in stiff material to prevent any unpredictable mount movements. The patient specific mount can be seen in Figure 3-3.

www.manaraa.com

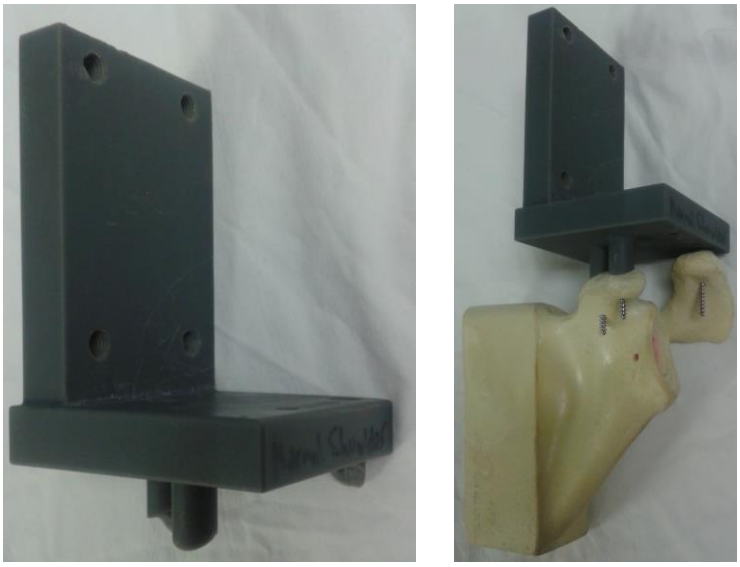

Figure 3-3: Patient Specific Scapula Mount.

The 3D printed scapula mount is designed to attach percutaneously with three bone screws to the coracoid and acromion.

3.4.2 Glenoid Attachment

Proper location of the scapula mount is crucial, since registration of the pre-operative planned pathway is achieved solely by this placement. Improper placement will result in the cuts being misaligned with the glenoid. To facilitate locating the scapula mount, an additional glenoid mount is 3D printed, which temporarily engages to both the scapula mount and the native glenoid bone (Figure 3-4). The mount was created using the Boolean subtraction feature to subtract the native glenoid from a general CAD model of the mount. Once in place, pilot holes were drilled using the legs of the scapula mount as guides and then the bones screws were used to secure the mount. The attachment of scapula mount registers the robot to the scapula model.

www.manaraa.com

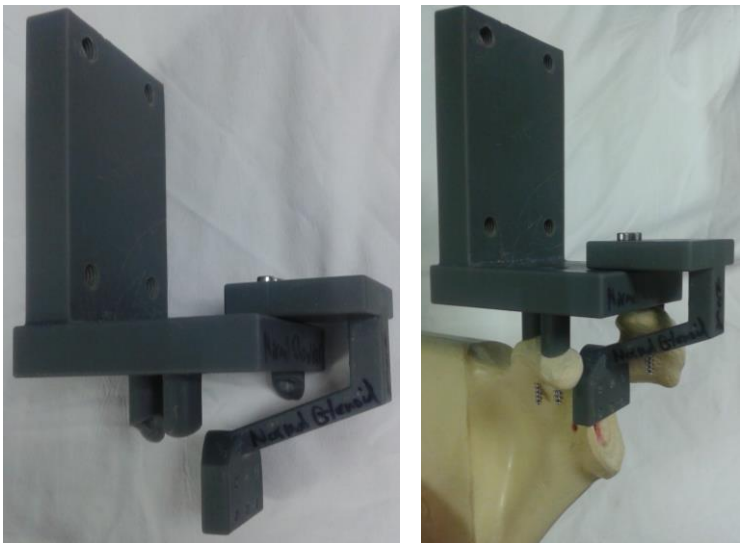

Figure 3-4: Patient specific mount assembly and attached to the sawbone model

The glenoid mount attaches to the scapula mount using pegs to align the part properly and was then screwed onto the scapula mount. This allows the glenoid mount to be removed separately from the assembly once the scapula mount was in place. Fiducial dimples on the glenoid mount were designed to be engaged by the spherical burr cutter for the robot to confirm the pre-op plan registration by localizing these fiducial, in a process that will be discussed later. The glenoid attachment can be seen in Figure 3-5.

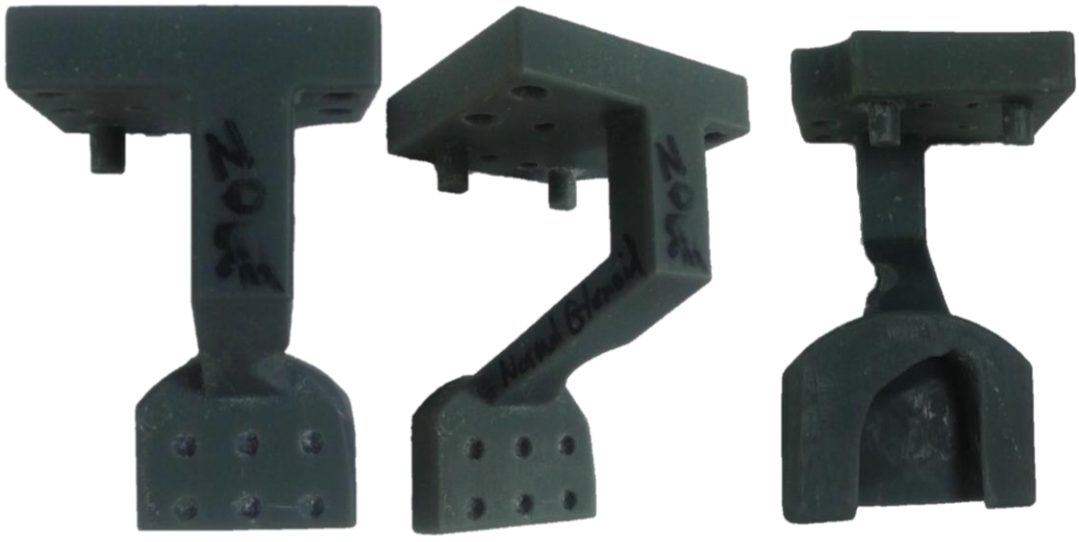

Figure 3-5: 3D printed glenoid attachment

www.manaraa.com

3.5 Cartesian Implant Path

3.5.1 CAD Implant Preparation

To generate a path for the desired implant, the CAD of the implant was first simplified. As, well, an extra 0.5 mm of clearance in all directions was added around the implant's fixation keel to allow room for polymethylmethacrylate (PMMA) bone cement. Then the new simplified CAD was Boolean subtracted from a block to create a negative cutout of the model (Figure 3-6).

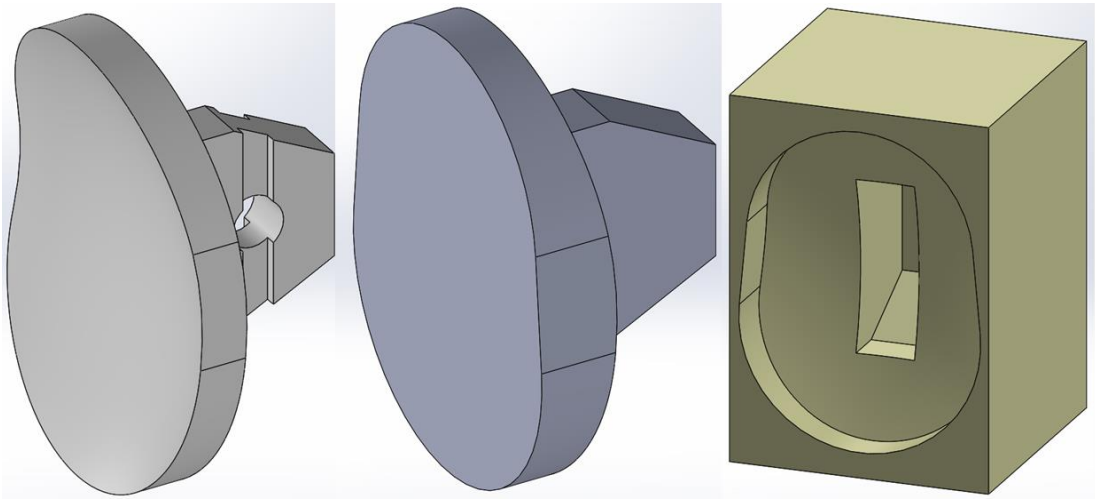

Figure 3-6: Preparing negative of implant for path generation.

A glenoid model is simplified and used to create a negative of the model that will be used to create a Cartesian Path.

3.5.2 Generating G-Code

The negative model was imported to BobCAD software to generate g-code for a CNC machine based on the 4 mm diameter tool size, boundaries and type of tool motion. The g-code generated produces Cartesian coordinates which can be used to calibrate the robot; however, the g-code may include step sizes that exceed 1 mm, so a separate MATLAB code was created to reduce step sizes to 1 mm. A graphic of the path generated for the glenoid model can be seen in Figure 3-7. This process is completely adaptable to any implant. With further development, a database of implant paths could be created and saved for ease of access to a surgeon.

www.manaraa.com

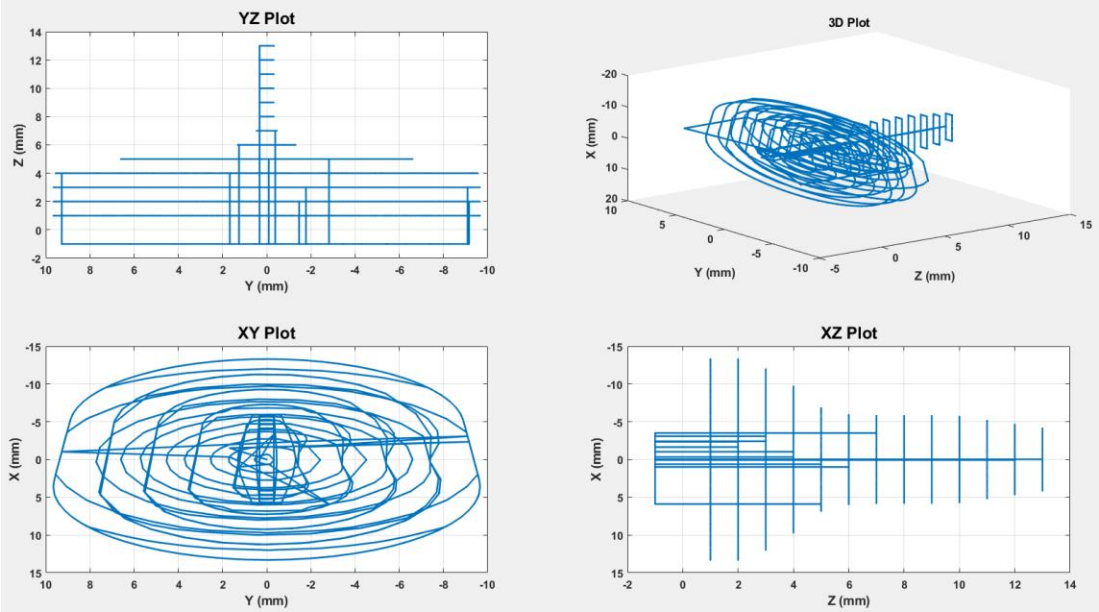

Figure 3-7: Cartesian Generated Path of a Keeled Glenoid Implant

3.5.3 Transforming G-Code to Robot Coordinates

Initially the BobCAD software creates the path coincident with the robots coordinate system. Thus, the implant needs to be transformed to the correct surgical location according to the pre-operative plan. The required transformation matrix is determined in CAD relative to the tool tip coordinate system (Figure 3-8).

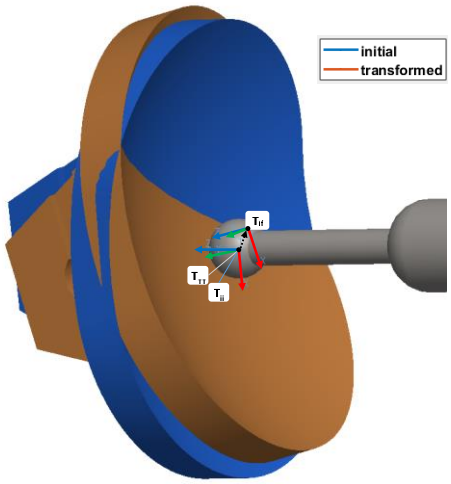

Figure 3-8: Alignment of implant placement.

The implant placement predicted by the initial g-code in robot coordinates (blue) is transformed to the pre-op planned pose (orange).

www.manaraa.com

The transformation matrix is then used to transform every point of the g-code path to the surgical orientation. An example is illustrated in Figure 3-9.

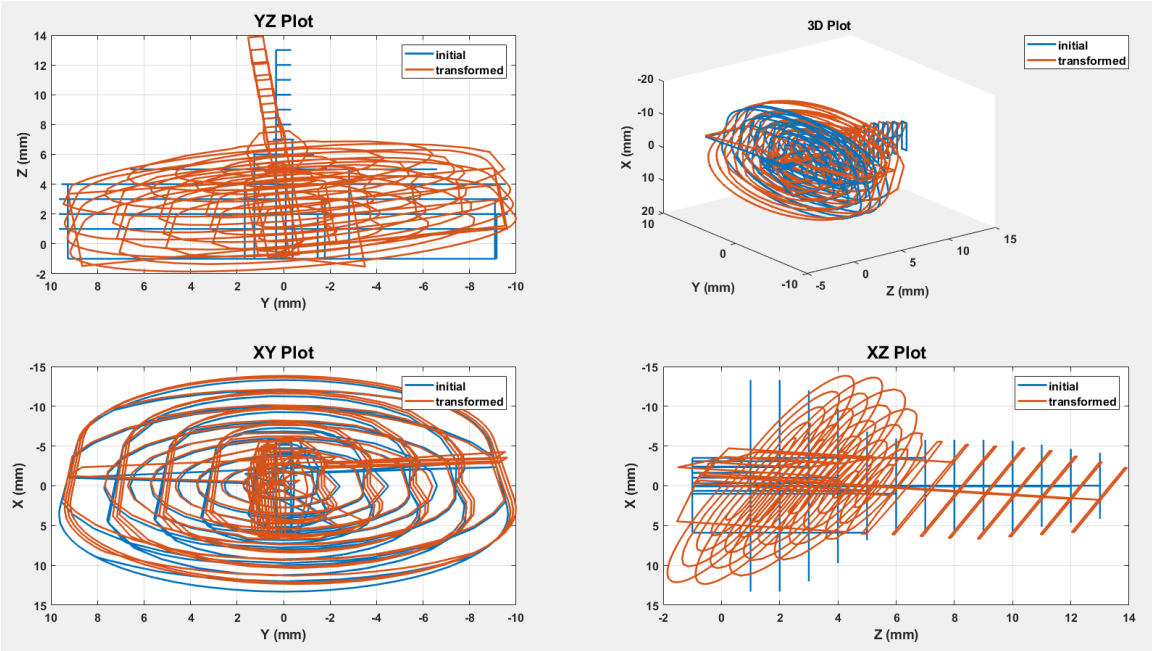

Figure 3-9: Alignment of Robot Pathway.

The initial g-code path (blue) is transformed according to the pre-op planned implant placement (orange).

3.6 Cartesian Calibration

3.6.1 Calibration Setup

With the patient specific mount secured to the scapula model, the scapula model was secured in place. The robot was attached to the Spider2 positioning arm. Next the flexible mount clamps are attached; one end to the robot right on top of the load cell and the other to the patient specific mount. Everything was bolted together to ensure the clamps could not move and so the flexible components could not move within the clamps. These attachment points can be seen in Figure 3-10.

www.manaraa.com

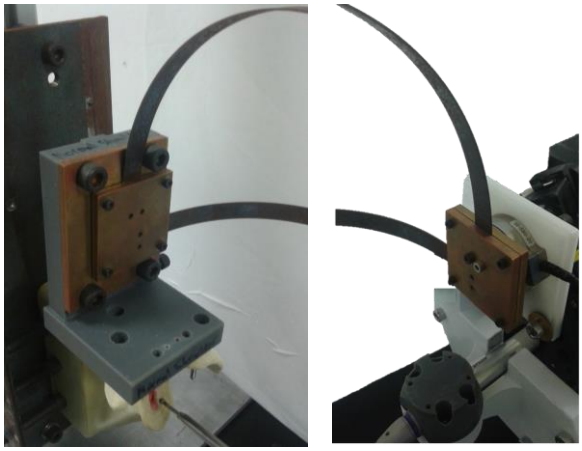

Figure 3-10: Flexible Mount Attachments

Flexible mount attachment to scapula (left), flexible mount attachment to robot (right)

The robot was then positioned in the approximate pre-determined surgical position and then clamped in position. It was important to secure all components of the set-up to ensure the only relative movements occurred from the platform moving the tool tip relative to the scapula. Since only the platform was moving relative to the tool tip, all the loads that were measured are based on the tool tip's position relative to the scapula. If the setup was not rigid, movements of other components would alter the loads causing unknown errors that could not be repeatable. The calibration setup can be seen in Figure 3-11.

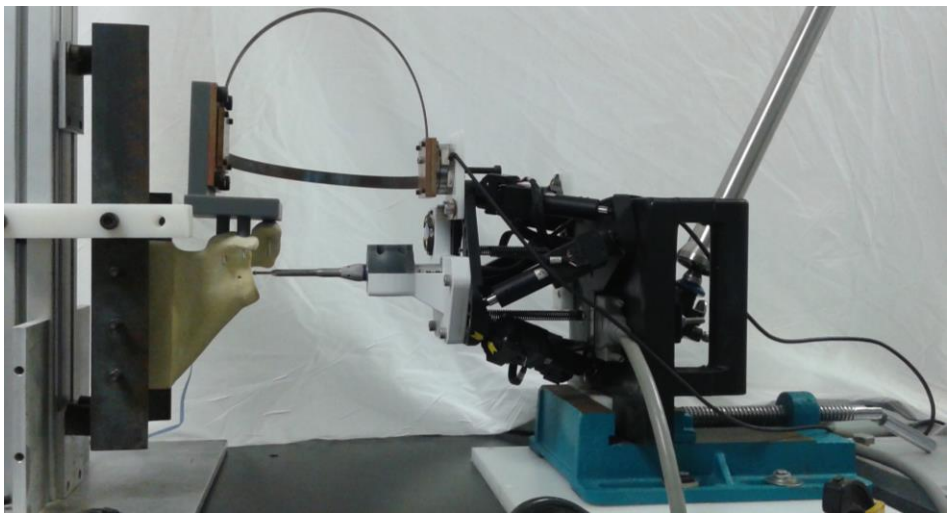

Figure 3-11: Calibration Set-up.

Both the robot and the shoulder analog are fixed in position for the calibration procedure, as described in Chapter 2.

www.manaraa.com

3.6.2 Optical Tracking

To help validate the tool tip's position throughout testing, a NDI OPTOTRAK Certus was used. A reference tracker was attached to a rigid post that the scapula model will be mounted to. A second tracker was attached to the robot platform that tracks the tool tip as the platform moves. Finally, a third tracker was attached to the base of the robot to track any movements that occurs for the base of the robot.

3.6.3 Digitization

To ensure the robot was in the correct location relative to the scapula model before calibrating, a digitization process was performed. This was facilitated by the use of spherical dimples that were added into the glenoid mount at certain pre-determined locations relative to the tool tip. The face of the glenoid mount can be seen in Figure 3-12.

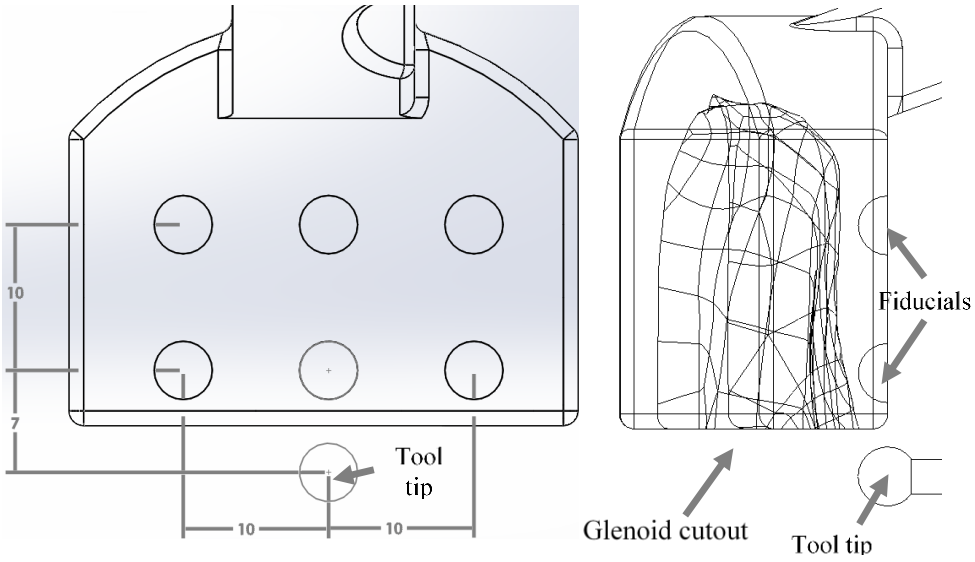

Figure 3-12: Glenoid implant fiducials relative to tool tip front view (left) and side view (right), dimensions in mm

Once the robot was reasonably positioned by the positioning arm, the robot platform was manually jogged using a joystick like control algorithm. The tool tip was moved to each dimple of the glenoid mount as seen in Figure 3-13 and the positions at each were outputted. Using the position data, the robot or scapula model were moved accordingly as needed and re-digitized until position error was minimal [41].

www.manaraa.com

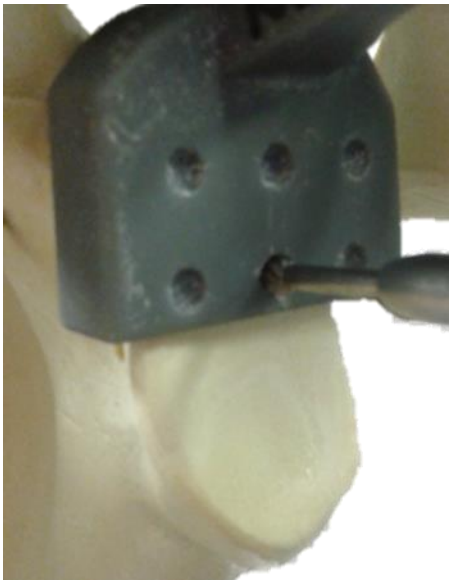

Figure 3-13: Intra-operative Robot Registration Confirmation.

Fiducial dimples on the 3D printed component were localized with the robot via the tool tip, to confirm proper coordinate registration of the pre-operative plan onto the anatomy.

Once the robot and scapula models were aligned, the glenoid mount was removed from the patient specific mount assembly. Next the burring tool was removed from the robot assembly to avoid the robot cutting the scapula model during the calibration run. Next the robot positioned was zeroed. Once zeroed, the load cell was zeroed. After these steps were complete, the Cartesian path was executed. During the calibration run, loads were recorded at each control point and used to create the corresponding load path.

A corresponding load path that represents the keeled glenoid implant can be seen in Figure 3-14. Looking at load path that was generated, the path does look like the Cartesian path. However, the load path looks like the glenoid has been warped. An important take away from this is that a load path does not represent the implant as a rigid body like the Cartesian path does.

www.manaraa.com

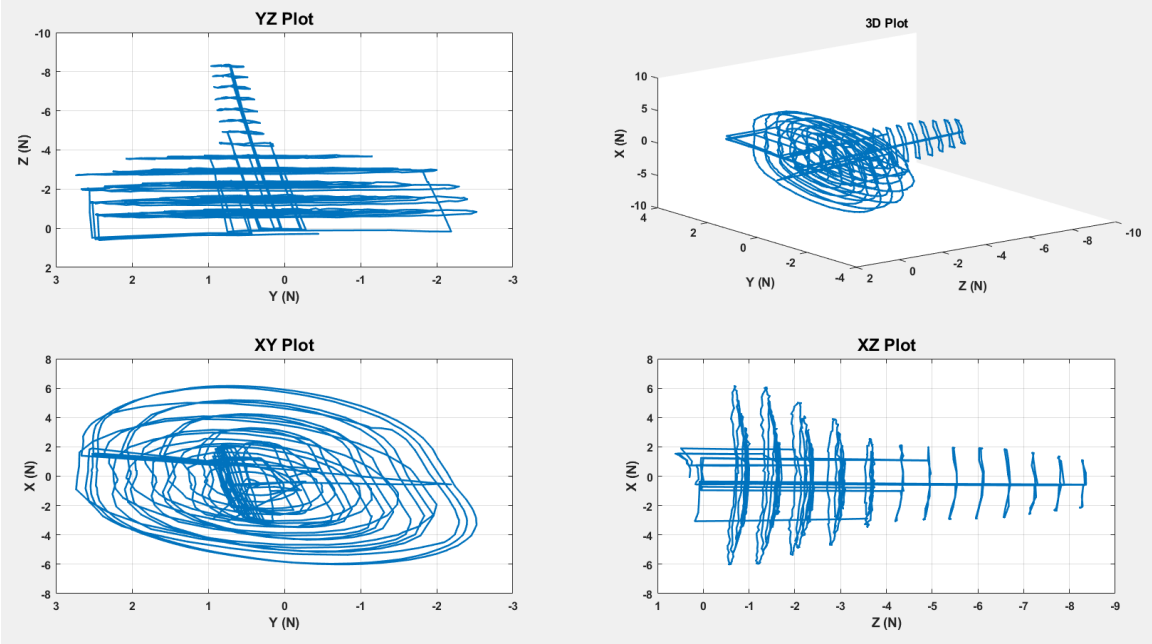

Figure 3-14: Corresponding Load Path of Glenoid Keeled Implant

3.7 Force-Space Navigation

3.7.1 Flexible Mount

To test the force-space navigation properly, it was important to try and mimic the relative movements of the scapula due to it being a floating bone in the body. As a result, it was important that this surgical system could compensate and adjust if the scapula were to move. To simulate the relative motion, a flexible mount was designed that allowed some movement of the scapula model when testing.

These rubber mounts were bolted to a fixed aluminum tower. One rubber mount in each corner of the steel C channel proved to be too stiff. As a result, only two rubber stand-off mounts were used in diagonally opposite corners. The flexible mount assembly can be seen in Figure 3-15. During the robot calibration, an additional bracket made of delrin was attached to the side of the post and the flexible mount to ensure the set-up was rigid and no relative motion occurred to that could cause errors in the calibration.

www.manaraa.com

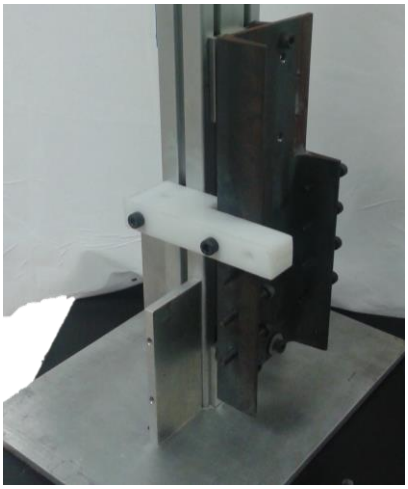

Figure 3-15: Flexible Mount Assembly

3.7.2 Load Path Set-Up

Once the load path was generated, the robot was set-up in similar fashion to the calibration set-up. The robot was positioned in the approximate pre-determined location. The tool tip was re-inserted into the assembly. The same digitization and re-positioning cycle was used in the calibration phase was used again to get the robot in the same location.

3.7.3 Load Path Execution

Once the robot was positioned correctly and everything was secured, the load cell was zeroed. The zeroing insures the force-space coordinate system was aligned with how the force space coordinate system was during the calibration. The same location was important to ensure the load space was consistent for both runs. Errors in positioning will cause an offset error in the cut.

Next, since the system was calibrated with all component rigidly fixed, all the loads correspond to the movements of the tool tip relative to the scapula. This means that if either the robot or the scapula moves a change in loads would be measured and the difference of that load from the target would be used as a correction. As a result, both the robot and the scapula do not need to be rigidly fixed. The robot was unclamped and was only supported by the Spider2. As well, the bracket on the flexible mount was removed allowing the mount to be able to wiggle. The final setup for load path navigation can be seen in Figure 3-16.

www.manaraa.com

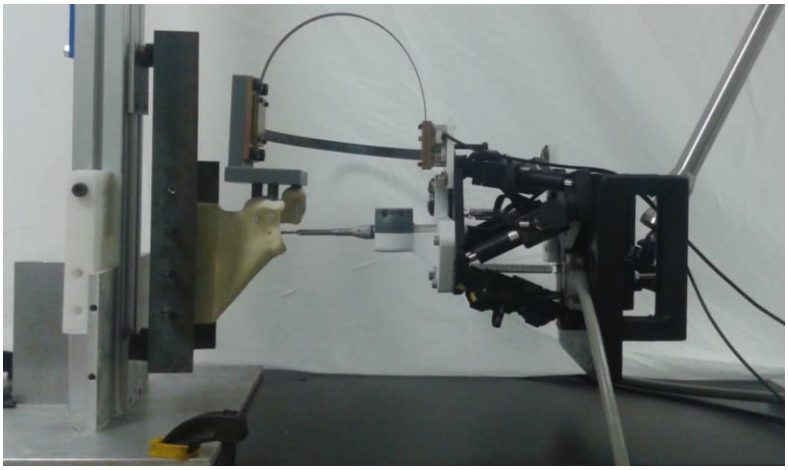

Figure 3-16: Load Path Set-up

A summary of the entire process force navigation process from pre-operative planning, to creating and running a load path can be seen in Figure 3-17.

www.manaraa.com

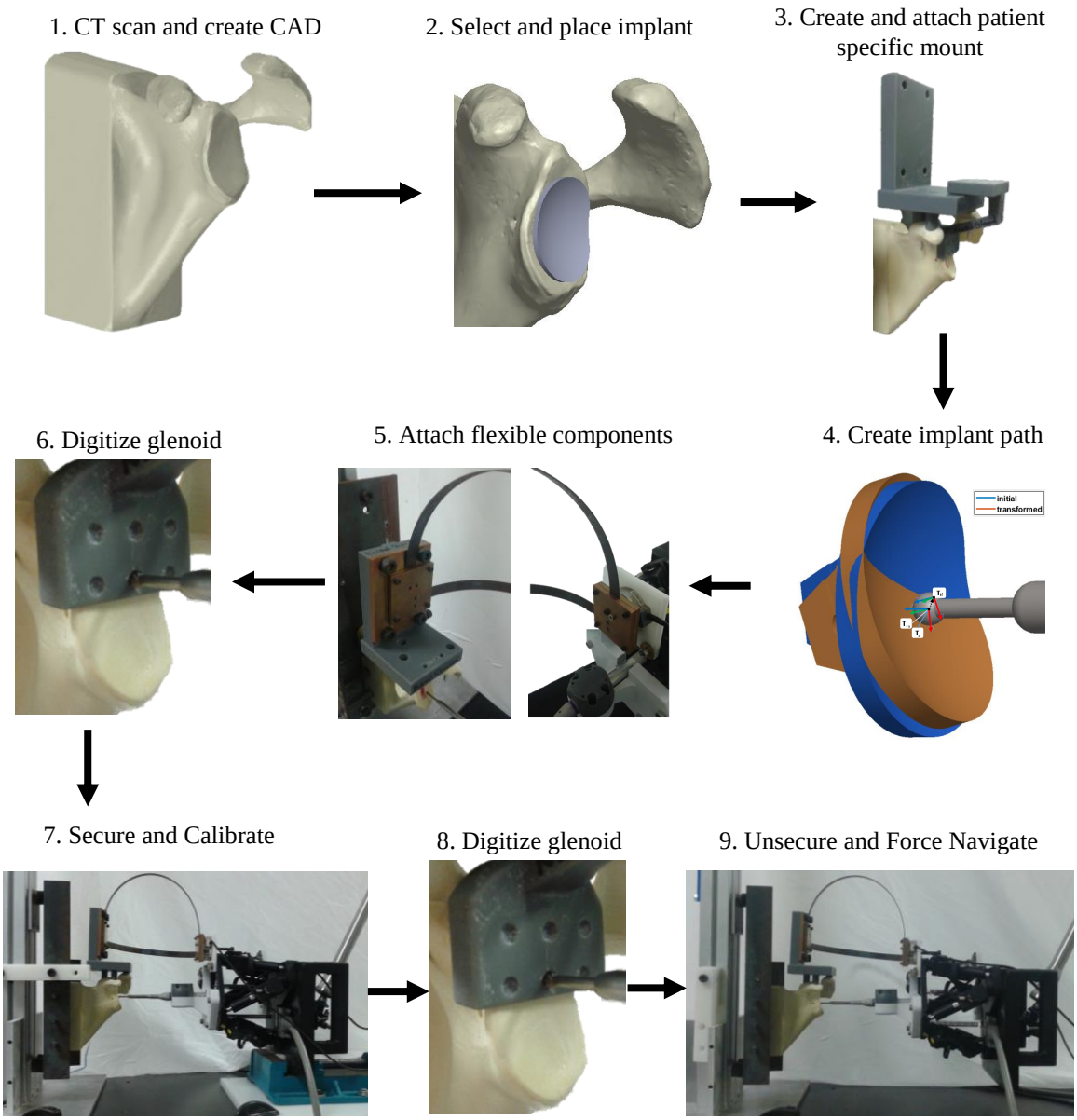

Figure 3-17: Process Summary

3.8 Performance Assessment Results

3.8.1 Calibration versus Force Space Results

The robot was tested using the previously mentioned methodologies and was run through a glenoid path. The test was performed on a Sawbone model but without the burring tool on the robot as cutting was not necessary to validate the control system as this will be address in the Chapter 4. To validate the robots position, a Certus tracker was used like in

www.manaraa.com

Chapter 2 for simple path testing. The robot was first calibrated in Cartesian space. Throughout the calibration, the robot position was tracked based on where the tool tip would be. The robot was then run through the load path and tracked in a similar fashion. The corresponding calibration and load run Certus tracking data can be seen in Figure 3-18.

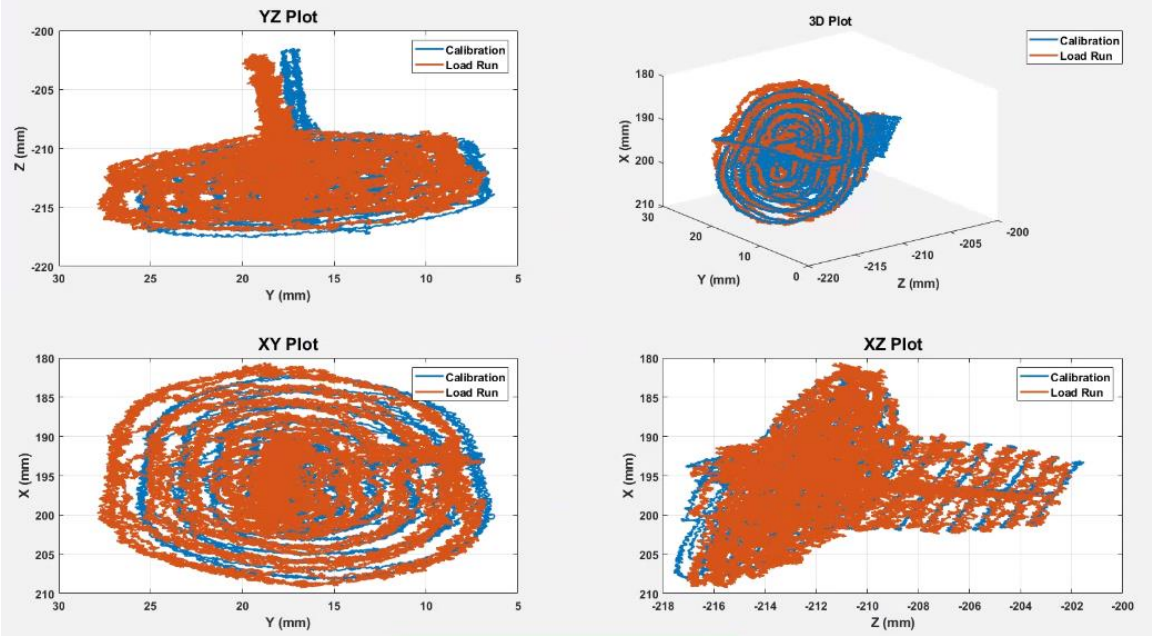

Figure 3-18: Certus Tracking Data of Calibration and Load Run

Each point of the load path was compared to its closest corresponding point of the calibration path. The resulting error in each direction and overall Euler distance is summarized in Table 3-1. Overall, the averaged Euler error was 0.65 ± 0.38 mm with the maximum error being 2.23 mm.

Table 3-1: Displacement error measured by Optotrak Certus.

	Average (mm)	St. Dev (mm)	Max Error (mm)
X	0.26	0.24	1.72
Y	0.43	0.39	2.14
Z	0.25	0.20	1.61
Euler	0.65	0.38	2.23

3.8.2 Object Tracking

As briefly mentioned in Chapters 1 and 2, the scapula is a floating bone, meaning that it is supported by soft tissues. Thus, reaction forces from the flexible strips, or cutting forces

www.manaraa.com

imparted on the glenoid by the burr, may cause unknown deflections of the anatomy. Additionally, the Spider2 orthopaedic positioning arm is not rigid. Moreover, these stiffnesses are not known. Therefore, the Force-Space Navigation controller must compensate for motion artifact via 6dof object tracking. To simulate unknown anatomical stiffness, the specimen mount was fitted with rubber standoffs. The robot and scapular mount were fitted with optical trackers (Optotrak Certus, NDI, Waterloo, ON) to provide gold standard measurements, as was done in Chapter 2. The optical tracker coordinate systems were transformed to the sawbone glenoid and robot tool tip to provide relevant motion tracking, and the stiffness of the flexible specimen mount and Spider2 arm were measured by the Certus over the complete range of motion for the operative plan (Table 3-2). Additionally, the corresponding Force-Space loads were also measured (Table 3-3).

Table 3-2: Displacement and rotation deviations for non-rigid components measured by Optotrak Certus

	X (mm)		Y (mm)		Z (mm)		Rx (°)		Ry (°)		Rz (°)	
	Max	Min	Max	Min	Max	Min	Max	Min	Max	Min	Max	Min
Flex Mount	0.46	-1.51	3.54	-0.47	0.59	-1.16	1.21	-0.39	0.37	-0.13	0.06	-0.07
Spider2	2.43	-2.91	2.20	-1.04	0.89	-1.43	0.86	-0.04	0.90	-0.36	0.19	-0.09

Table 3-3: Load deviations measured by 6-DOF load cell

X (N)		Y (N)		Z (N)		Rx (N·m)		Ry (N·m)		Rz (N·m)	
Max	Min	Max	Min	Max	Min	Max	Min	Max	Min	Max	Min
10.51	-9.58	5.12	-4.86	5.89	-8.44	0.53	-0.27	0.81	-1.11	1.22	-1.15

The relationship between the navigation forces and the displacements unaccounted by the planned path are essentially a measure of the system's stiffness. For example, 5.12 N in the Y direction caused a maximum of 5.74 mm of undue motion, which the Force-Space controller must compensate for to meet the targeted path.

3.9 Discussion

From the glenoid path analyzed, the robot system was shown to be highly accurate. On average, there was sub-millimeter accuracy in all directions and overall. The maximum error that was experienced was just over 2 mm which is still relatively small error.

The more interesting result of the test was the circumstances that the robotic system could maintain its accuracy. During the load run, the system was not rigid and relative

www.manaraa.com

movements of the scapula and/or the robot base occurred. However, since the system was calibrated with everything rigid and the loads measured being relative to the scapula, the system can "feel" when an unforeseen relative movement occurs and will correct for it.

Correcting for unforeseen relative movements, like movements of the bone or the robot being bumped is an issue that current robotic system cannot account for. The current robotic systems may be able to detect that the robot or bone has moved but cannot immediately compensate. These systems likely need to be stopped and the bone needs to be re-digitized. In this test, the robot could correct for the robot base and the flexible mount making relative movements throughout the run. In shoulder replacement surgeries, the scapula is suspended by soft tissues and can move during glenoid reaming. Therefore, it is crucial that this system can correct for these inevitable movements.

3.10 Chapter Summary

In this chapter, the pre-operative plan necessary to complete a glenoid replacement of a Sawbone scapula was outlined. The pre-operative plan begins with taking a laser scan of the scapula and creating a 3D CAD model. Using the CAD model, a surgeon selected an appropriate implant and places the implant virtually in the correct surgical location. A path corresponding to the glenoid was created based on the surgeon's selection. The robot was then calibrated with this path in Cartesian space to get the corresponding load path. The robot was run through the load path.

During the load run the robot was unclamped and the flexible mount was free to move. Optical tracking data was used to validate the robots positioning and showed the relative movements of the base and the flexible mount. The tracking data showed the robot to be highly accurate, averaging sub-millimeter accuracy throughout even with large relative movements of the robot base and scapula. This shows the robot could adjust for unforeseen movements during the procedure. Allowing compliance in the system will be beneficial as trying to maintain a completely rigid system in an OR would be difficult; the robot could be bumped and the scapula moves with in the body.

www.manaraa.com

CHAPTER 4

4 Application of the Force-Space Navigation Robot in a Shoulder Analog

OVERVIEW: *This chapter examines a study that was performed that looked to compare the robot to a trained surgical fellow. Two different scapula models were used with each model having its own pre-op plan prepared by the surgeon. Based on the pre-op plan the robot did six cuts of each model using the steps outlines in Chapter 3. The surgeon also performed six cuts of each model using standard practices.*

4.1 Experimental Design

To test the reliability and accuracy of the robot, a pilot study was designed that compared the surgical results of the robot to a trained surgeon. The study used the scapula models from Sawbones like in Chapter 3. Two different scapula models were selected for testing. Both models were left shoulders. The first model had normal bone geometry. The second model had erosion of the posterior edge of the glenoid otherwise known as Walch B2 type erosion [42]. Using two different models added diversity to the study and different aspects and challenges. For the tests, both the surgeon and the robot did glenoid replacement for six normal and six B2 models each. The two different scapula models can be seen in Figure 4-1.

www.manaraa.com

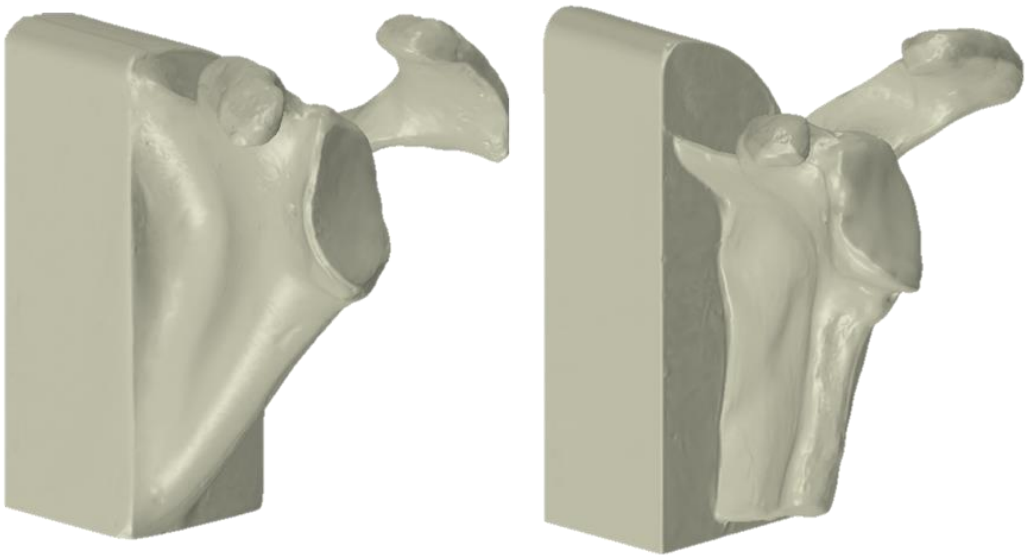

Figure 4-1: Normal Shoulder Model (left) and B2 Shoulder Model (right).
These surface models were reverse-engineered from the Sawbone analogs using a 3D laser scanner (Space Spider, Artec3D, Santa Clara, CA).

4.2 Pre-operative Plan

4.2.1 Implant Selection

With 3D models created for each shoulder model, the surgeon chose corresponding implants for each model in the same fashion that would be done in an OR setting. For the normal shoulder model, a small AEQUALIS™ PERFORM keeled glenoid implant with a 30-mm radius from Wright Medical was chosen. For the B2 shoulder model, a medium AEQUALIS™ PERFORM+ CORTILOC glenoid implant with a 25-degree wedge from Wright Medical was chosen. The implants can be seen in Figure 4-2.

www.manaraa.com

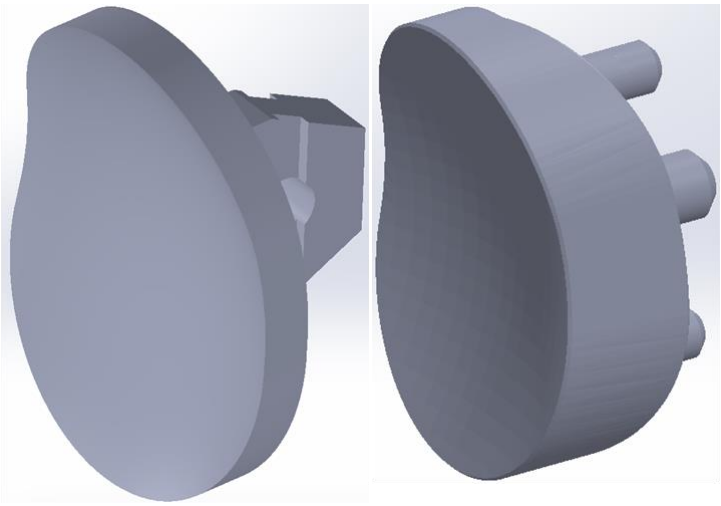

Figure 4-2: Normal Implant (left) and B2 Implant (right)

4.2.2 Implant Placement

Using models of the implants, the surgeon virtually placed each implant onto its corresponding scapula model in an appropriate surgical location. Coordinate systems were created for the scapula models by having the surgeon select four points for each model. These points corresponded to a superior, inferior, anterior and posterior positions on the glenoid face. Using these points, two vectors were created: a superior/inferior (S-I) axis and anterior/posterior (A-P) axis. The cross product of these two vectors created the medial/lateral (M-L) axis which was aligned to the midpoint of the S-I axis. The cross product of the S-I axis and the M-L axis, created a new A-P axis. The S-I axis, new A-P axis, M-L axis defined the coordinate systems x, y and z axes respectively, which was located at the midpoint of the S-I vector. The glenoid coordinate system was defined in the same manner using four points along the implant's face. The defined coordinate systems can be seen in Figure 4-3.

www.manaraa.com

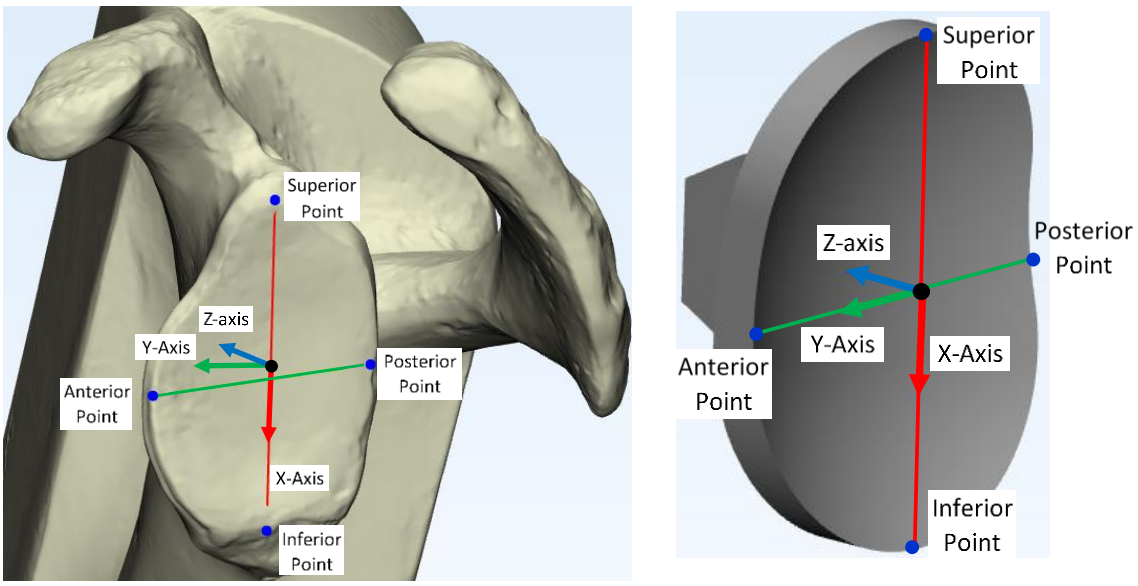

Figure 4-3: Standard scapula coordinate system (left), standard keel implant (right)

Each model's corresponding implant was placed virtually by the surgeon and was used as the target for both the surgeon's tests and the robot's tests. The implant placements for both shoulder models can be seen in Figure 4-4.

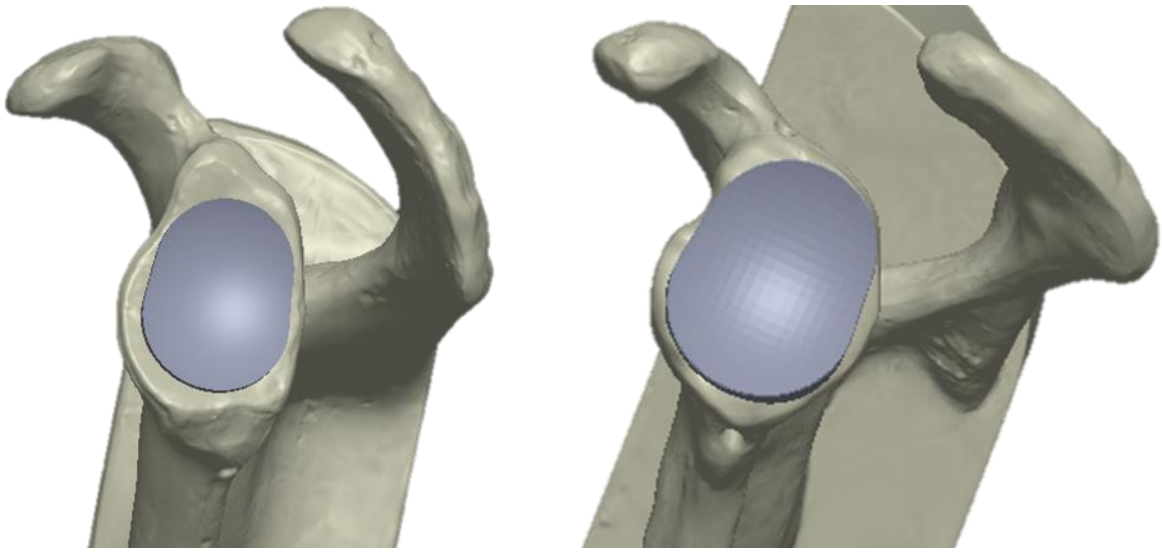

Figure 4-4: Normal Implant Placement (left) B2 Implant Placement (right)

For the purposes of this work directions were adjusted based on anatomical standards. The X direction was defined along the superior-inferior axis with superior direction defined as

www.manaraa.com

positive X. Rotation about X was defined as the version angle. The Y direction was defined along the anterior-posterior axis with the anterior direction defined as positive Y. Rotation about Y was defined the inclination angle. The Z direction was defined along the lateral-medial axis with the lateral direction defined as positive Z. Rotation about Z was defined as face rotation with counter-clockwise being positive. The coordinate system definitions can be seen in Figure 4-5. The corresponding anatomical placements can be seen in Table 4-1.

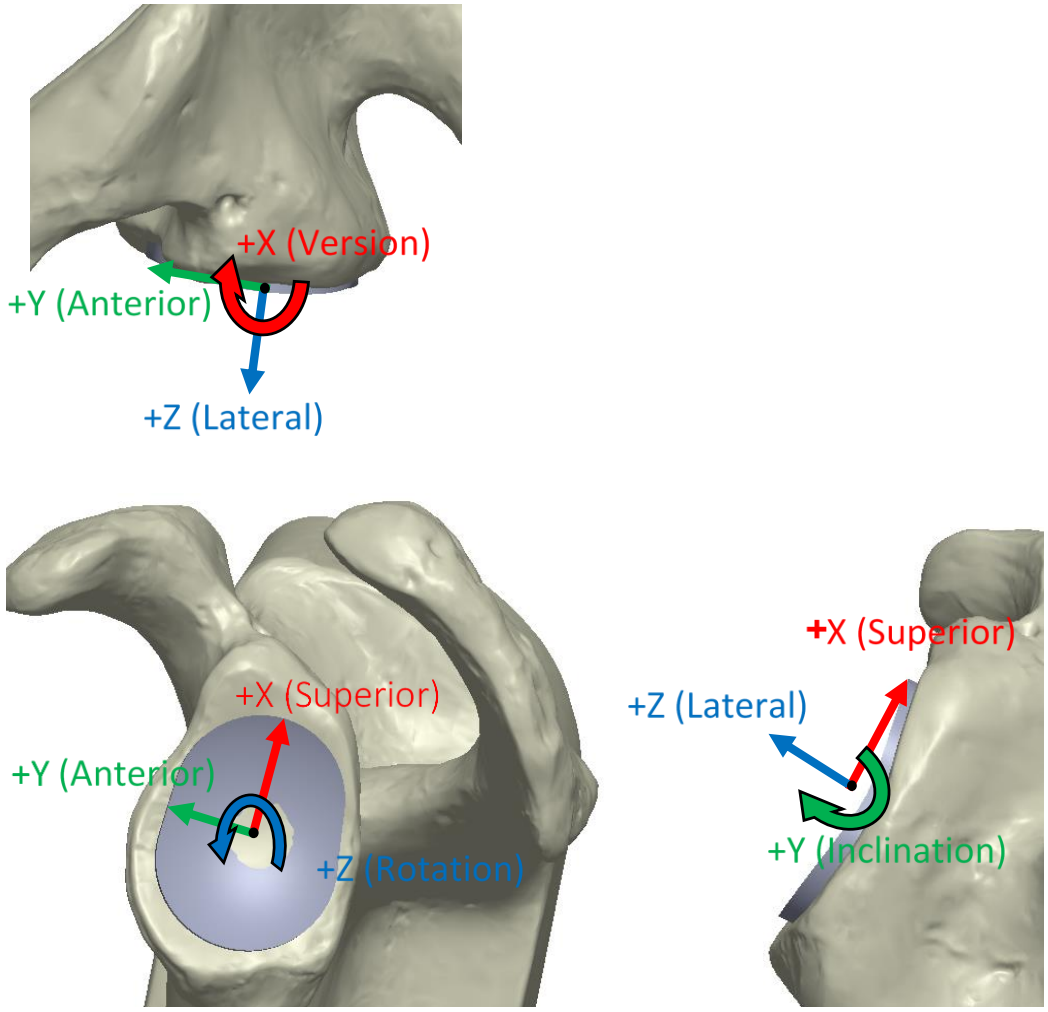

Figure 4-5: Glenoid Implant Direction Definitions

Table 4-1: Anatomical pre-op placement of implants relative to scapulae

	S-I (mm)	A-P (mm)	M-L (mm)	Version (°)	Inclination (°)	Rotation (°)
Standard	-1.55	-0.79	1.24	1.70	2.12	-10.15
B2	0.95	-0.66	4.68	7.18	-1.09	-14.94

www.manaraa.com

4.3 Surgical Methodologies

4.3.1 Robot Methodology

The robot used the methodology laid out in Chapter 3. Scapula mounts were made specifically for each scapula model. As well, specific Cartesian paths were developed for each implant. For the normal implants, 0.5 mm of clearance around the keel was used. As well, for the B2 implants the peg radius was increased by 0.5mm. These clearances were added to allow space for bone cement after the procedure. All 12 scapula models were calibrated individually with their respective Cartesian paths. The corresponding load path was then used to mill the glenoid cavity of each scapula model.

4.3.2 Surgeon Methodology

For the surgeon's testing, the appropriate surgical tools for both normal implants and B2 implants were provided by Wright Medical. The tooling needed for a standard keel implant can be seen in Figure 4-6. Note, the figures show tooling for different sizes of implants, so not all these tools shown are needed for one procedure. The procedure was performed based on the Wright Medical Group surgical guidelines [43].

Figure 4-6: Standard keel replacement tooling[6]

As well, the tooling needed for a B2 pegged implant can be seen in Figure 4-7. Note, the figure shows tooling for different size and different angles of B2 pegged implants, so not

[6] Modified from AEQUALIS™ PERFORM™ Glenoid Implant [Internet]. Wright Medical Group Inc., Memphis, TN; cited [December 18, 2017]. Available from: http://www.wright.com/products-upper/aequalis-perform-shoulder-system

www.manaraa.com

all tools shown are needed for one procedure. The procedure was performed based on Wright Medical Group surgical technique guidelines [44].

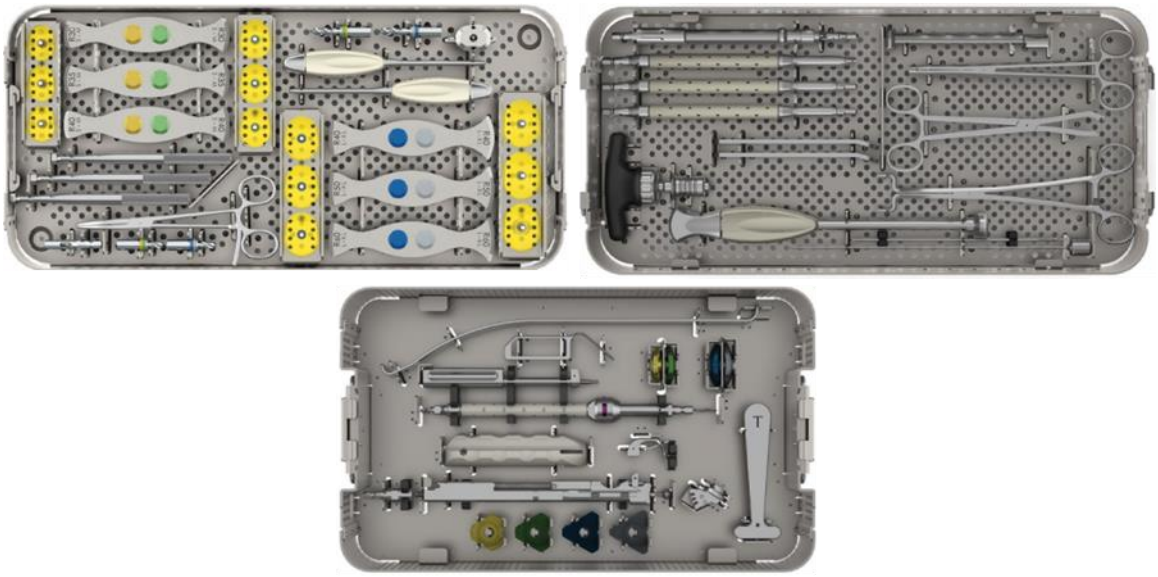

Figure 4-7: B2 pegged implant replacement tooling[7]

To make the surgeon's testing more realistic, a rubber shoulder was added to mimic the skin around the scapula model. This helped to limit the field of view and hide some of the bony landmarks that would not be visible during a real procedure. Since the robot does not technically see the skin, it was not necessary to add rubber model to the robot testing. With the rubber model surrounding the scapula model, the scapula was clamped to a table in the approximate surgical orientation. The surgeon's test set-up can be seen in Figure 4-8. The surgeon did an initial surgical incision on the rubber shoulder and this was held open with retractors. The same rubber shoulder was used for all 12 of the surgeon's cuts. The surgeon followed the same procedures that would be followed in the OR and described by Wright Medical.

[7] Modified from AEQUALIS™ PERFORM™+ Shoulder System [Internet]. Wright Medical Group Inc., Memphis, TN; cited [December 18, 2017]. Available from: http://www.wright.com/products-upper/aequalis-perform-augmented-glenoid

www.manaraa.com

Figure 4-8: Simulated Surgical Exposure for Surgeon.

The surgeon's experimental setup was made to mimic a typical anterior approach for shoulder arthroplasty.

4.4 Processing Results

Once all 24 shoulder models (12 by the robot, 12 by the surgeon) were complete, many steps were taken in order to analyze the results of the study. These steps included:

1. CT scan all scapula models with the implants in place but uncemented
2. Surgeon cements implants in place for all scapula models
3. CT scan all scapula models with implants cemented
4. Segment and create 3D computer models from CT scans

www.manaraa.com

5. Register post-op scapula cuts to the pre-op scapula
6. Transform post-op implants to their corresponding registered post-op scapula
7. Register a pre-defined implant to the post-op implants
8. Export transformation matrix of pre-op

4.4.1 Uncemented CT Scans

After the testing, implants based on the normal and B2 implants were 3D printed. The corresponding implant for each scapula model was pressed into placed and was clinical CT scanned. An example of a CT scan of a normal shoulder model can be seen in Figure 4-9. In the scan the scapula and implants are clearly visible which was beneficial for segmenting the two components.

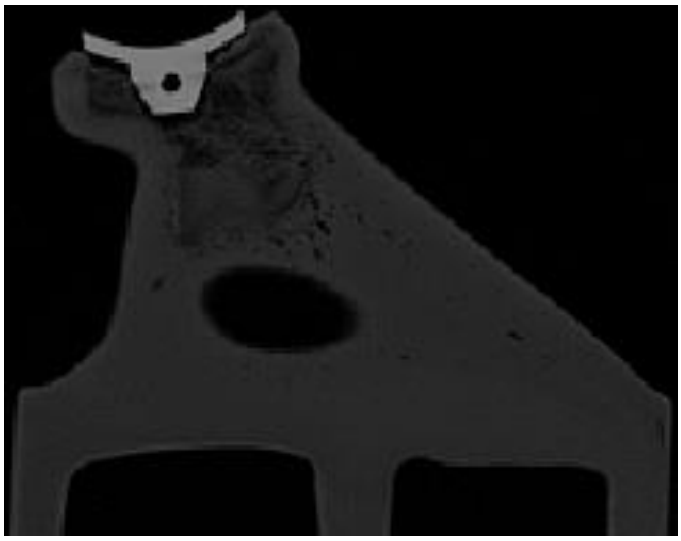

Figure 4-9: CT scan for robot prepared uncemented standard keel implant

It was noticed that some of the B2 implants in the models for both the surgeon and the robot were not seated properly. Due to the robot's limited range-of-motion, extra depth to the peg cuts could not be added as it should have been to allow for some tolerance. To help with this, the peg holes for all B2 scapula were manually milled slightly deeper to allow both the robot and surgeon implants to sit on the prepared glenoid face. The B2 scapulae were scanned again after the pegs were drilled to see if there were any changes.

www.manaraa.com

4.4.2 Cement Implants

After the uncemented implants were scanned, the same surgeon that did the reaming tests earlier, helped cement the implants for the shoulder models. Cement was placed into the keel cavity and into the peg holes for the normal and B2 implants respectively. The implants were held in place with pressure until the cement dried.

4.4.3 Cemented CT Scans

Once the implants were cemented, all the models were CT scanned again. A cemented CT scan be seen in Figure 4-10. From the scan, the scapula model, cement and implant were all clearly visible allowing for easy segmentation.

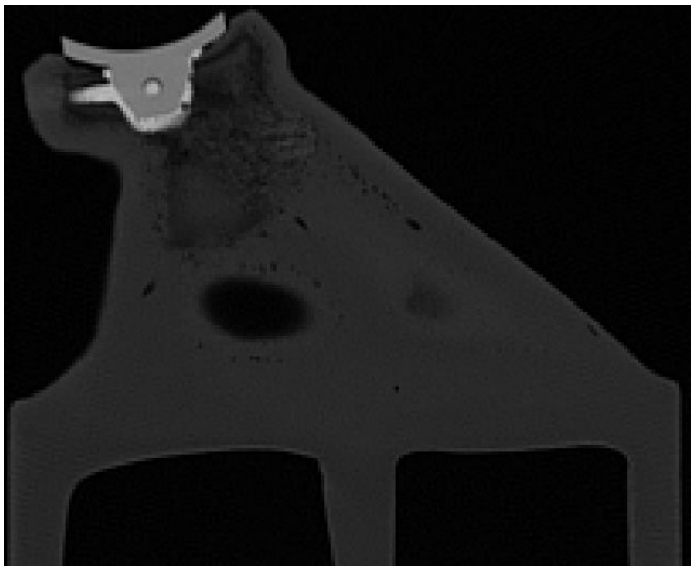

Figure 4-10: CT scan for robot prepared cemented standard keel implant.
Cement mantel can be seen in the bright white around the keel of the implant.

4.4.4 Segmentation and 3D models

Using the CT scans, both the scapulae and implants were segmented. Using the segmentations, separate 3D scapula models for each cut model and their corresponding implants were created. The segmentation and creation of 3D models were done using Mimics. A segmented scapula and implant along with the corresponding 3D models can be seen in Figure 4-11.

www.manaraa.com

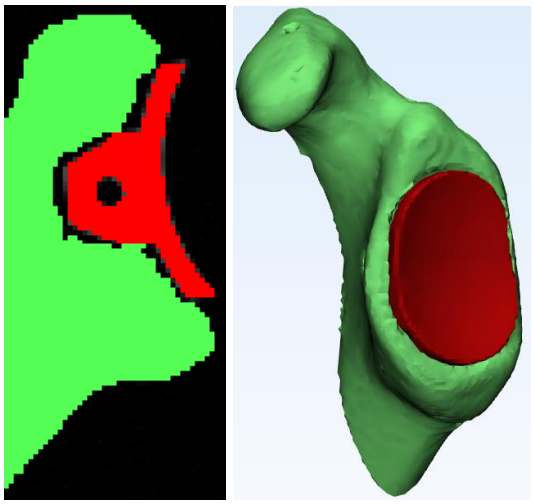

Figure 4-11: Post-Experiment CT scan of Robot Placement for Keeled Implant.
A segmented DICOM cross section (left) shows final cemented placement of the implant (red) in the scapula (green). A 3D model (right) was exported to facilitate placement measurements. The cement mantle (black region between implant and scapula) was not segmented since it was not needed for measurements.

4.4.5 Global Registration

Once all the post-op scapula and implant models were created, the post-op models were copied to 3-Matic. Next the pre-op plan scapula and implant models were brought into 3-Matic as well. In 3-Matic, there is a function called “global registration” which allows for a model to be overlaid and aligned to a similar model [45], [46]. The registration function, was used to align each post-op scapula model to the pre-op scapula. An example of a global registration can be seen in Figure 4-12.

www.manaraa.com

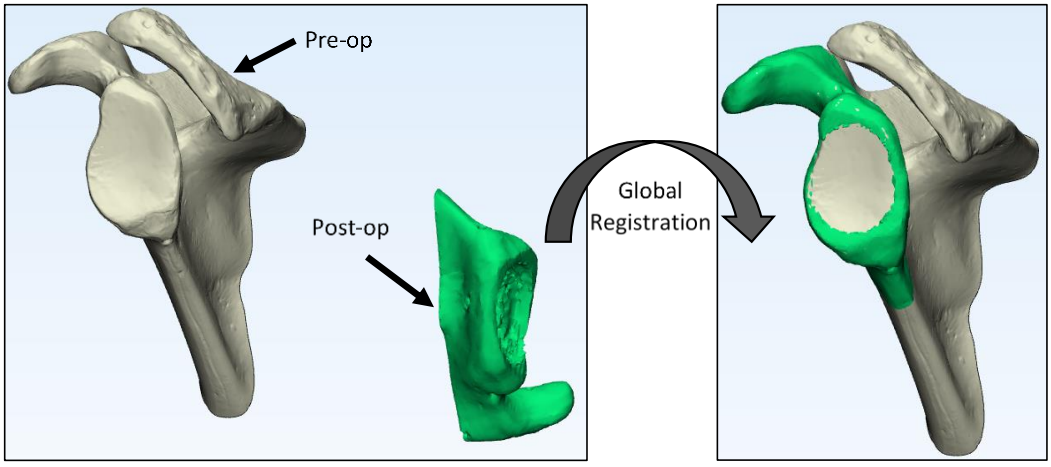

Figure 4-12: Pre-op scapula and unregistered robot post-op scapula (left), corresponding registered robot post-op scapula (right)

4.4.6 Transform Post-Operative Implants

After a post-op scapula was registered, the transformation matrix that the program used to move post-op scapula from its original position to its final position was exported. This transformation matrix was then applied to the corresponding post-op implant to move the implant into the same relative position with respect to its post-op scapula. An example of a transformed post-op implant can be seen in

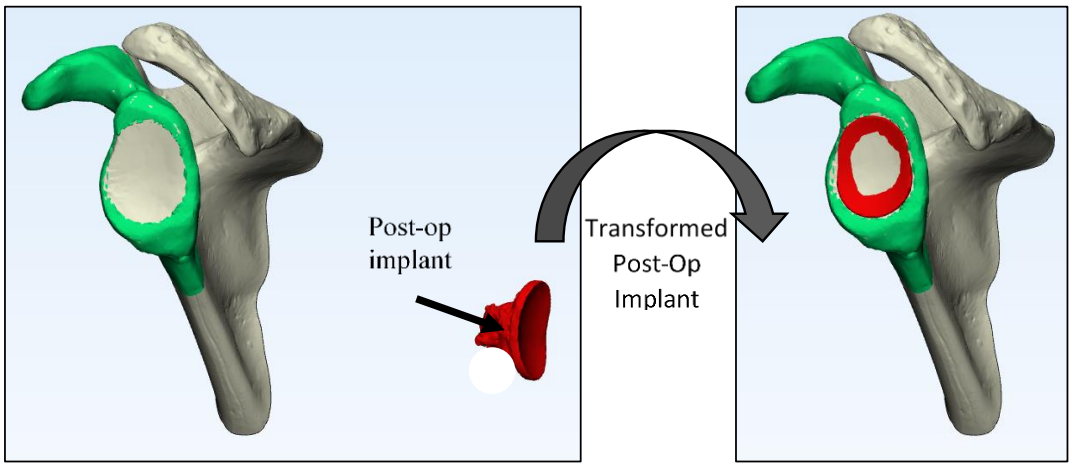

Figure 4-13: Untransformed robot post-op keeled implant (left), transformed keeled implant (right)

www.manaraa.com

4.4.7 Register Known Implant

When the post-op implants were created, 3-Matic creates a generic coordinate for the 3D model. To properly compare the location of a post-op implant to the pre-op implant, well-defined coordinate systems were needed. The pre-op implant model already had a known coordinate system. To have the post-op implants have the same oriented coordinate system as the pre-op implants, a pre-op implant part was globally registered to the post-op implant. A post-op implant with a registered implant with a known coordinate system can be seen in Figure 4-14.

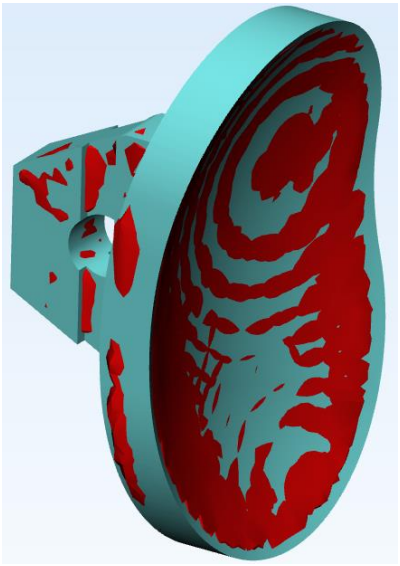

Figure 4-14: Post-op robot keeled implant (red), registered implant (turquoise)

4.4.8 Post-Op Implant Transformation to Pre-Op Implant

Now with post-op and pre-op implants positioned with correctly defined coordinate systems, a transformation matrix can be defined to determine placement and orientation error. The pre-op implant was used as the fixed coordinate system and the post-op implant coordinate system was measured relative to that fixed coordinate system. This allowed measurements of error in three orthogonal directions and the rotations about these directions. An example of a pre-op implant and post-op implant can be seen in Figure 4-15.

www.manaraa.com

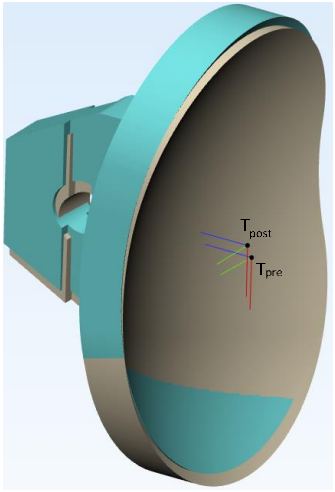

Figure 4-15: Pre-op target (Beige), Post-op position (Turquoise)

4.5 Normal Shoulder Test Results

4.5.1 Cut Results

Looking at the normal keeled glenoid implants, there were many visual differences that were apparent. Firstly, the robot's cuts in general appeared to be deeper into the bone than the surgeon this can be seen from the pink trabecular bone that was visible in the robot's cuts. As well, due to the larger cutting head of the reamer used by the surgeon, the entire glenoid face was cut away, while the robot only cuts the shape of the glenoid with a small burring tool leaving a border of bone all around the cut. Finally, the surgeon's large reaming tool meant a relatively smooth cut surface, while the robot using a small burring tool meant a rougher cut surface. Examples of a normal robot cut and the surgeon's cut can be seen in Figure 4-16.

www.manaraa.com

Figure 4-16: Normal keeled glenoid implant cut comparison

Robot (left) versus surgeon (right)

Next, looking at the models after the implants were placed, one major difference was noticed. Firstly, because the robot leaves the border of bone and cuts the shape of the implant, the implant has a press fit when placed. The implant could be pressed in place and even without cement the implant was difficult to remove. Examples of the glenoid implants in place can be seen in Figure 4-17.

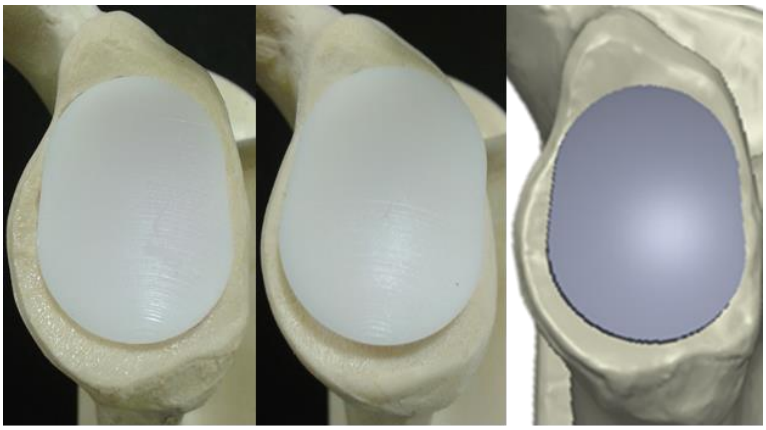

Figure 4-17: Normal keeled glenoid implant placement

Robot placement (left), surgeon placement (centre), pre-op plan placement (right)

www.manaraa.com

Similar differences in the B2 pegged implant cuts, like the normal cuts, were noted. The surface of the surgeon's cuts were much smoother due to the large reaming to that was used. Since the robot used the small burring tool, it could cut the shape of the implant and leave a ridge of bone around the implant. As well, the surfaces of the robot tended to be rougher from the small burring tool. The robot's cut appeared to be cut deeper into the bone. Finally, the surgeon's cut required an extra hole in the bone for tool alignment that was not necessary for the robot. An example of a robot B2 cut and a surgeon B2 cut can be seen in Figure 4-18.

Figure 4-18: B2 pegged implant cut comparison

Robot cut (left) and surgeon cut (right)

Once the implants were in place, the robot's cuts seemed to sit deeper into the bone. The rough cuts of the robot made it slightly difficult to press the implant in place. This can easily be solved with a larger robot that can provide more range of motion to allow some clearance around the implant. A different cutting tool on the robot may allow a smoother cut surface that would prevent higher areas of the surface from lifting the implant off. An example of a robot's B2 pegged implant placement and a surgeon B2 pegged implant placement can be seen in

www.manaraa.com

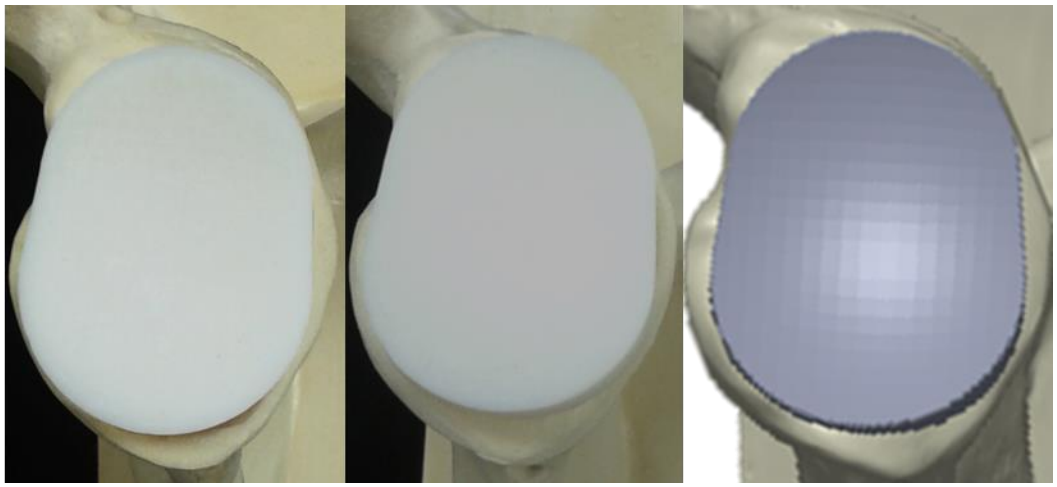

Figure 4-19: Comparison of B2 pegged implant placement

Robot placement (left), Surgeon placement (centre), Pre-op planned placement (right)

4.5.2 Angle and Displacement Error

Data from all 12 normal shoulders (six robot, six surgeon) were gathered from the CT scans. For the purposes of this chapter, only the cemented results will be shown and analyzed. The angle error of for both the surgeon and the robot's cuts relative to the pre-op plan can be seen in Figure 4-20. The corresponding displacement error can be seen in Figure 4-21. The rest of the data gathered pertaining to uncemented scans can be seen in APPENDIX E:.

www.manaraa.com

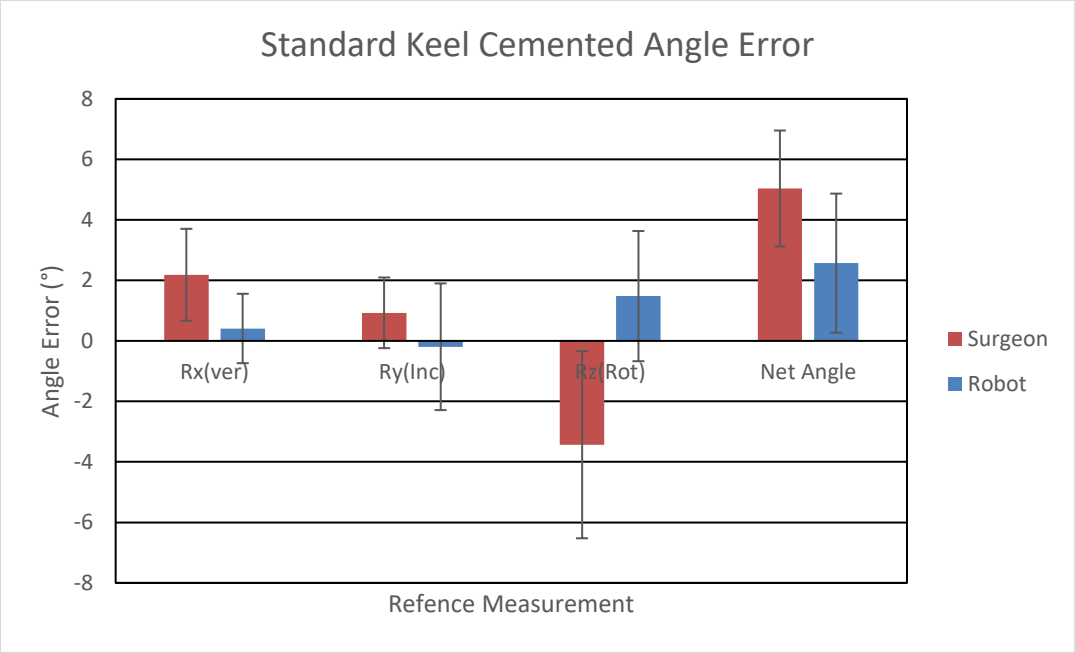

Figure 4-20: Average angle error relative to pre-op implant

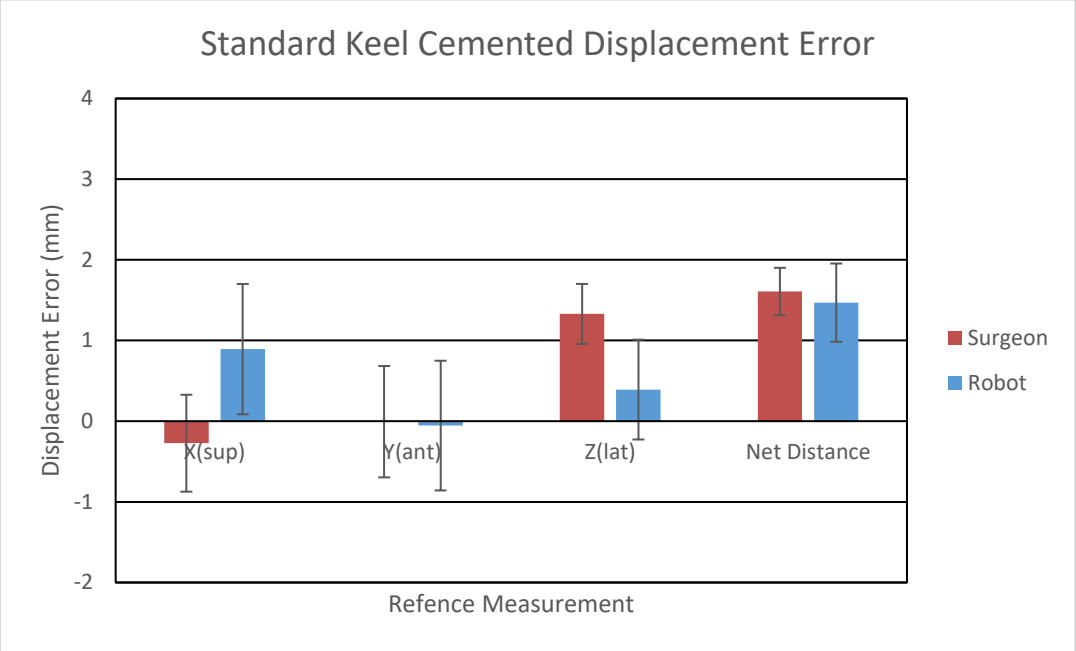

Figure 4-21: Average displacement error relative to pre-op implant

4.6 B2 Shoulder Test Results

Data from all 12 B2 models (six robot, six surgeon) was gathered from the CT data. For the purposes of this chapter, only the cemented data was shown. The angle error for both

www.manaraa.com

the surgeon and the robot's cuts relative to the pre-op plan can be seen in Figure 4-22. The corresponding displacement error can be seen in Figure 4-23. The rest of the B2 data pertaining to the uncemented scans can be seen in APPENDIX E:.

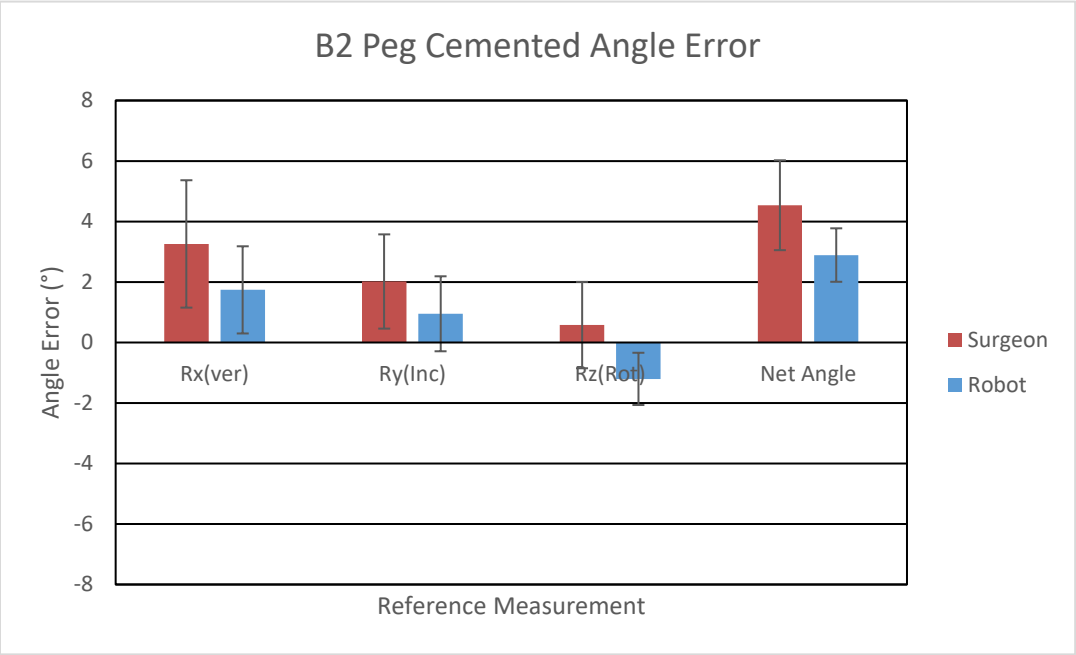

Figure 4-22: Average angle error relative to pre-op implant

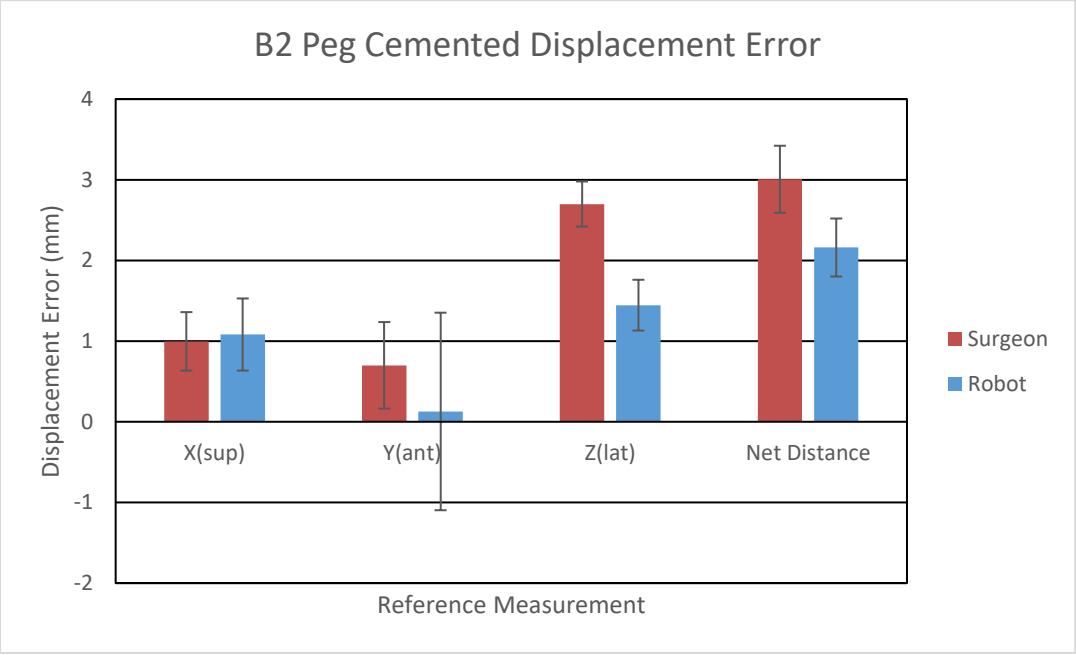

Figure 4-23: Average displacement error relative to pre-op implant

www.manaraa.com

4.6.1 Statistical Comparison

To compare the robot and the surgeon's data, repeated measures MANOVA tests were performed. The tests used a significance of $p < 0.05$ and a Bonferroni correction to reduce the likelihood of a Type 1 error occurring. MANOVA results of the cemented normal shoulder can be seen in Table 4-2. MANOVA results of the cemented B2 shoulder can be seen in Table 4-2. Additional statistics of uncemented data can be seen in APPENDIX E:.

Table 4-2: Robot vs Surgeon Standard Cemented MANOVA Test Results

Measure	Robot (I)	Surgeon (J)	Mean Difference (I-J)	Std. Error	Significance (p<0.05)*	95% Confidence Interval for Difference	
						Lower Bound	Upper Bound
Rx	1	2	-1.775	0.770	0.069	-3.755	0.205
	2	1	1.775	0.770	0.069	-0.205	3.755
Ry	1	2	-1.122	1.277	0.42	-4.406	2.161
	2	1	1.122	1.277	0.42	-2.161	4.406
Rz	1	2	4.913	1.600	0.028*	0.799	9.026
	2	1	-4.913	1.600	0.028*	-9.026	-0.799
Net Angle	1	2	-2.469	1.038	0.063	-5.136	0.199
	2	1	2.469	1.038	0.063	-0.199	5.136
X	1	2	1.166	0.387	0.03*	0.172	2.16
	2	1	-1.166	0.387	0.03*	-2.16	-0.172
Y	1	2	-0.048	0.480	0.924	-1.281	1.185
	2	1	0.048	0.480	0.924	-1.185	1.281
Z	1	2	-0.938	0.156	0.002*	-1.339	-0.536
	2	1	0.938	0.156	0.002*	0.536	1.339
Net Distance	1	2	-0.138	0.309	0.674	-0.934	0.658
	2	1	0.138	0.309	0.674	-0.658	0.934

Table 4-3: Robot vs Surgeon B2 Cemented MANOVA Test Results

Measure	Robot (I)	Surgeon (J)	Mean Difference (I-J)	Std. Error	Significance (p<0.05)*	95% Confidence Interval for Difference	
						Lower Bound	Upper Bound
Rx	1	2	-1.519	1.071	0.215	-4.271	1.234
	2	1	1.519	1.071	0.215	-1.234	4.271
Ry	1	2	-1.067	0.839	0.259	-3.225	1.09
	2	1	1.067	0.839	0.259	-1.09	3.225
Rz	1	2	-1.780	0.823	0.083	-3.894	0.335
	2	1	1.780	0.823	0.083	-0.335	3.894
Net Angle	1	2	-1.647	0.882	0.121	-3.914	0.619
	2	1	1.647	0.882	0.121	-0.619	3.914
X	1	2	0.085	0.259	0.755	-0.579	0.75
	2	1	-0.085	0.259	0.755	-0.75	0.579
Y	1	2	-0.572	0.542	0.340	-1.964	0.821
	2	1	0.572	0.542	0.340	-0.821	1.964
Z	1	2	-1.254	0.164	0.001*	-1.674	-0.833
	2	1	1.254	0.164	0.001*	0.833	1.674
Net Distance	1	2	-0.846	0.139	0.002*	-1.205	-0.488
	2	1	0.846	0.139	0.002*	0.488	1.205

www.manaraa.com

Next the robot and surgeon were compared to zero, i.e. the target position and orientation. A one-sample t-test was performed with a target value of zero and a significance of $p < 0.05$. The cemented normal shoulder t-test can be seen in Table 4-4. The cemented B2 shoulder t-test can be seen in Table 4-5.

Table 4-4: Robot and Surgeon Standard Cemented T-Test

Measure	t	df	Significance (2-tailed) (p<0.05)*	Mean Difference	95% Confidence Interval of the Difference	
					Lower	Upper
Robot Rx	0.877	5	0.420	0.411	-0.793	1.615
Surgeon Rx	3.524	5	0.017*	2.186	0.592	3.781
Robot Ry	-0.226	5	0.830	-0.193	-2.391	2.004
Surgeon Ry	1.948	5	0.109	0.929	-0.297	2.155
Robot Rz	1.686	5	0.153	1.481	-0.777	3.740
Surgeon Rz	-2.717	5	0.042*	-3.432	-6.678	-0.185
Robot Net Angle	2.741	5	0.041*	2.571	0.159	4.982
Surgeon Net Angle	6.445	5	0.001*	5.040	3.030	7.050
Robot X	2.707	5	0.042*	0.893	0.045	1.740
Surgeon X	-1.115	5	0.316	-0.273	-0.904	0.357
Robot Y	-0.167	5	0.874	-0.055	-0.899	0.789
Surgeon Y	-0.023	5	0.982	-0.007	-0.731	0.718
Robot Z	1.55	5	0.182	0.392	-0.258	1.041
Surgeon Z	8.75	5	0.000*	1.329	0.939	1.720
Robot Net Distance	7.421	5	0.001*	1.469	0.960	1.978
Surgeon Net Distance	13.393	5	0.000*	1.607	1.299	1.916

Table 4-5: Robot and Surgeon B2 Cemented T-Test

Measure	t	df	Significance (2-tailed) (p<0.05)*	Mean Difference	95% Confidence Interval of the Difference	
					Lower	Upper
Robot Rx	2.957	5	0.032*	1.740	0.227	3.252
Surgeon Rx	3.791	5	0.013*	3.258	1.049	5.468
Robot Ry	1.875	5	0.120	0.949	-0.352	2.250
Surgeon Ry	3.171	5	0.025*	2.017	0.382	3.651
Robot Rz	-3.414	5	0.019*	-1.203	-2.109	-0.297
Surgeon Rz	0.989	5	0.368	0.576	-0.922	2.074
Robot Net Angle	8.012	5	0.000*	2.891	1.963	3.818
Surgeon Net Angle	7.482	5	0.001*	4.538	2.979	6.097
Robot X	5.922	5	0.002*	1.081	0.612	1.551
Surgeon X	6.725	5	0.001*	0.996	0.615	1.377
Robot Y	0.256	5	0.808	0.128	-1.157	1.413
Surgeon Y	3.194	5	0.024*	0.699	0.136	1.262
Robot Z	11.243	5	0.000*	1.445	1.115	1.776
Surgeon Z	23.638	5	0.000*	2.699	2.405	2.992
Robot Net Distance	14.714	5	0.000*	2.160	1.783	2.537
Surgeon Net Distance	17.725	5	0.000	3.006	2.570	3.442

المنارة للاستشارات
www.manaraa.com

4.7 Discussion

4.7.1 Cemented Normal Shoulder Models

For this surgical system to be a viable addition to a shoulder replacement surgery, it was important that the robot was either as good as or better than the surgeon in general. Based on the statistical tests performed, the robot results were significantly different from the surgeon for the rotation about Z, translation in X, and translation in Z. Based on the graphical data, the robot had smaller error for both rotation and translation in Z. The robot had a 1.48 ± 2.15° and 0.39 ± 0.62 mm in z versus the surgeon's -3.43 ± 3.09° and 1.33 ± 0.37 mm in Z. This error for the surgeon was not surprising as the surgeon has no guide to know what depth they are reaming at. As well, the rotation error in z for the surgeon was not surprising, as the cutting tool is spherical and therefore gives no way to reference the rotation.

For translations in X the robot had slightly more error of 0.89 ± 0.81 mm versus the surgeon's -0.27 ± 0.60 mm. Although the x translation was statistically significant it would not be clinically significant as both methods had sub-millimeter accuracy.

Based on the t-test data, the surgeon error was significantly different from the pre-op implant target for rotation in X, Z and net angle, as well as translation in Z and the net displacement. This shows the most significant errors for the surgeon were the version angle, face rotation, and the depth of the glenoid. The surgeon had an average version angle of 2.19 ± 1.52°, an average face rotation of -3.43 ± 3.09 mm and a depth of 1.33 ± 0.37 mm. This means the implants were typically based with a positive version angle, a negative face rotation and the glenoid sitting proud. For the robot, it was significantly different from the pre-operative plan in only the X translation, net angle and net displacement. The X translation was relatively minimal and both the net angle and net displacement.

Overall, the robot performed very well and generally had as good as or better results than the surgeon. The robot could maintain an average angular error in X and Y of less than 0.5° and less than 1.5° in Z. In translations, the robot maintained sub-millimeter accuracy on average in each direction and overall displacement error of less than 1.5 mm.

www.manaraa.com

4.7.2 Cemented B2 Shoulder Models

Analyzing the cemented B2 results showed that the robot was only significantly different from the surgeon in the translation in Z and the net displacement. In the Z direction, the robot had error of 1.44 ± 0.32 mm while the surgeon had error of 2.70 ± 0.28 mm. As a result, the robot performed better in this aspect. It is important to note, both methods had the implant sitting proud. In terms of net displacement, the significant difference occurred due to the difference in Z error.

Based on the t-test data, the surgeon error was significantly different from the pre-op implant in all cases except for the rotation in Z. For the robot error, it was significantly different the pre-op implant in all cases except for the translation in Y and rotations in Y. This was not surprising as B2 models are more complex and are therefore more difficult to work on. In the case of Z rotation, although the robot was significantly different from the target there was only error of -1.20 ± 0.86° which would not be clinically significant.

Interestingly to note the surgeon always had a positive version angle, with a couple specimens having greater than +5° of version and an average of 3.26 ± 2.11° while the robot had an error of 1.74 ± 1.44° and a max error of 3.61°. Overall, the robot the robot was averaged angle errors below 2° for all three rotations, as well as less than 1.5 mm errors in each direction. The net angle averaged was less than 3° while the net displacement was less than 2.2 mm.

4.7.3 Implications

The robot performed as good as or better than the surgeon. This system would not look to replace the surgeon but provide an additional tool for the surgeon during a shoulder replacement procedure. The system still requires the surgeon to pre-operatively plan the procedure and oversee the robot's setup and milling. However, while the robot is milling the surgeon can prepare other steps of the surgery.

Another benefit to this system, is that it can replace the large number of tools required for a surgical procedure. The robot used the same bone burring tool for both the standard keel and the augmented B2 implant. In current procedures, multiple tools are required, and as

www.manaraa.com

the geometry of the implants becomes more complex so too does the tools required. These tools need to be inventoried and sanitized after each procedure. For this surgical system only one tool is required and the burring tool can be sanitized or replaced after each procedure.

4.8 Chapter Summary

The robot surgical system was tested against a surgical fellow. Both the robot and the surgeon performed their respective glenoid replacement surgical procedure on the two different types of shoulder models. The two types of shoulder models that were used were a normal anatomy scapula and a scapula with posterior edge erosion of the glenoid. Six of each shoulder model was operated by both the robot and the surgeon.

Once all the procedures were complete, the models were CT scanned with the implants uncemented and the cemented in place. 3D models were created from the CT scans. The scapula 3D models were registered to the pre-operative plan. From there, the offsets of the post-operative to the pre-operative implants were recorded.

The robot's results were compared to the surgeon's and both were compared to the target to see if any significance occurred. Generally, the robot proved to be as good as or better than the surgeon in every translation and rotation metric for both shoulder types. Overall, the robot averaged near sub-millimeter accuracy in each translation direction and averaged less than 2° rotation errors in each direction.

www.manaraa.com

CHAPTER 5

5 Discussion and Future Work

OVERVIEW: *This chapter examines the results in the context of the hypothesis outlined in Chapter 1, as well as a summary of the control algorithm used to transform from Cartesian space to force space. The strengths and limitations of this system are discussed, based on the pilot testing and comparison tests with a surgeon. Finally, future work pertaining to cadaveric testing is proposed.*

5.1 Summary

As glenoid implant designs become more intricate, the process and tooling required for the surgeon to accommodate the designs becomes more complex. Even for current implant designs, many different tools are required for each surgery. Orthopaedic robotic systems (Mako, ROBODOC) have been used for many years for hip and knee replacements for improved accuracy [11]. However, these surgical robots typically use optical tracking which is hindered by the need for line-of-sight, additional tracker incisions and additional maintenance costs.

A new surgical navigation system was designed, which utilized a Stewart platform for actuation and a 6 DOF load cell to measure the reaction forces and torques from flexible components tethered to the patient. By running the robot through a Cartesian path and measuring the reaction loads at control points, a corresponding force-space path was created. Utilizing the force-space path, allowed the robot to "feel" its way through the desired path.

With typical tracking, rigid body transformations to the pre-op plan can be done, and the plan path remains relatively unchanged (i.e., same shape). But with the Force-Space Navigation method, a rotation of the pre-op plan results in a new load path that is slightly

www.manaraa.com

morphed compared to the unrotated plan. This is different from object tracking during navigation. If there is unanticipated movement of the anatomy, then the load navigation path is not recalculated. Rather, the proportional controller corrects for these small errors.

A rigid body transformation cannot be directly applied to a load path. For example, two load paths were generated from the same Cartesian path with the post the robot is tethered to normal to the robot and then again with the post rotated 20 degrees about its vertical axis. These load paths can be seen in Figure 5-1 and Figure 5-2. This shows the load path is not based solely on the Cartesian path, the entire set-up can alter the load path that would be generated.

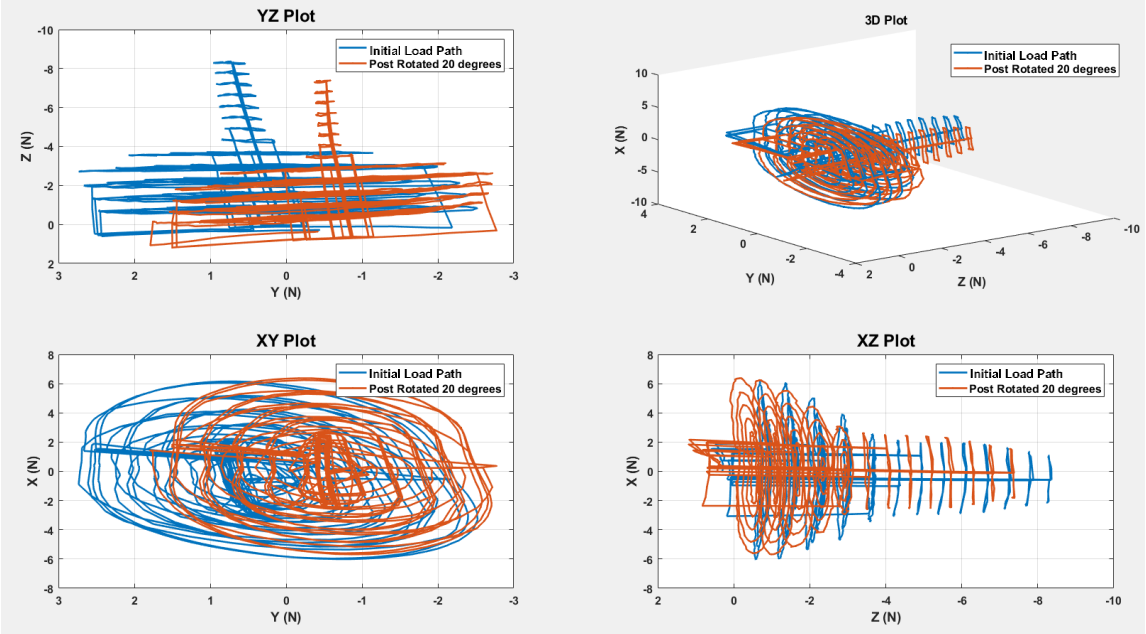

Figure 5-1: Force comparison of normal and rotated post

www.manaraa.com

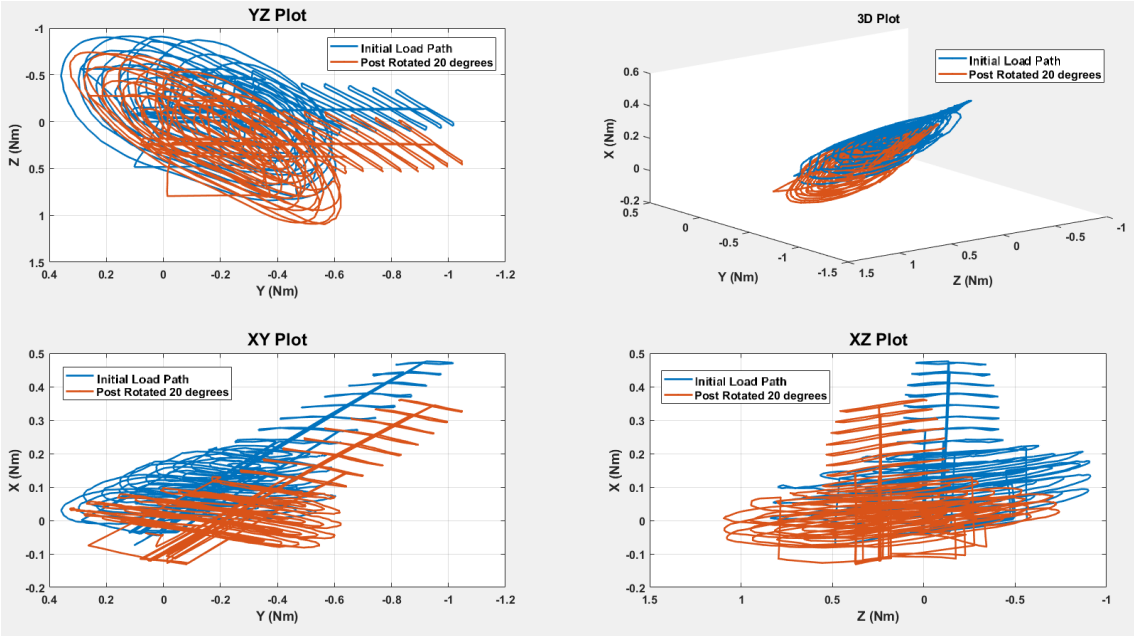

Figure 5-2: Torque comparison of normal and rotated post

Once the proof of concept testing was complete, an entire step by step workflow from anatomical scan and pre-operative planning was outlined in Chapter 3. The corresponding Cartesian path was created and calibrated to a force-space path. An experiment was setup with the robot mounted in a manner consistent with operating room protocols and a shoulder analog was designed to simulate unaccounted for scapular motion for the controller to compensate in real-time. Performance tests based on a glenoid implant again resulted in error less than the 2-mm hypothesized.

Finally, the completed system was tested against a fellowship trained shoulder surgeon in a series of shoulder analogs using two types of glenoid implants. Final implant placements were measured from CT scans and compared to the pre-operative plans determined by the surgeon. The robot was more accurate than the surgeon in almost every direction metric with statistical significance.

5.2 Strengths

Standard surgical technique requires complex tool sets which are specific to implant designs. Each of the two glenoid implants tested require a specific tool set which costs

www.manaraa.com

approximately $300,000 each. Due to this cost, it is typical for an industry representative to deliver the sets to medical centres within his/her region. This business model raises costs and causes delays in our healthcare system. In comparison, the robot required only one tool which was suitable for both implants, and the same workflow was used for both implant types. Rather than sterilizing dozens of tools after surgery, the robotic system is designed so that the burr and all the patient-specific parts are low-cost and disposable. The robot itself is designed to be shrouded using a standard surgical shrouding bag to avoid the need for post-surgical sterilization.

Compared to surgical robotic systems in clinical use, the proposed surgical robot has many advantages. Firstly, the Stewart platform robot is much smaller than current systems, which are floor-mounted and take up valuable OR space. Current systems are typically very expensive, costing hundreds of thousands, even into the millions of dollars, whereas this first prototype robot cost $20,000 and the load cell cost $13,000.

Current systems use optical tracking which require additional incisions for tracker far from the surgical working volume that could become infected which are not required for the purposed system. Optical tracking needs constant line-of-sight which is not an issue with reaction force navigation. As well, optical tracking adds additional costs of the camera system and the trackers. Costs are also incurred from cleaning, replacing and cataloging the trackers and the labor costs associated with these tasks. The robots tracking system is all contained between the patient and the robot. The flexible components and patient specific mounts would be replaced every surgery and are relatively inexpensive.

5.3 Limitations

Additional pre-operative planning compared to traditional manual techniques was required, although existing robotic systems in clinical use also require pre-operative planning. The calibration can be done prior to surgery but still requires time to set-up and generate the load path. This would require either a second robot to perform calibration or for the surgical robot to be moved out of the OR. Additionally, a 3D print model of the patient's scapula will be needed for calibration.

www.manaraa.com

The Stewart platform used for testing was limited by its range of motion. The working volume for the robot could only fit small glenoid models and only in one specific orientation. This meant the robot had to be positioned precisely relative to the scapula model to perform the cut properly. Ideally, the robot would be positioned and the digitization of the glenoid would be used to transform the implant path instead using it to move the robot into the correct position.

5.4 Future Work

A new larger and faster Stewart platform will be utilized. Range of motion can be analyzed based on method outlined in 2015 by Chkhartishvili & Suryamurthy [47]. This will allow for larger implant sizes to be cut and different orientations of the robot to be utilized such as an anterior approach to the glenoid which is a more natural angle based on the surgical opening.

Reducing OR time is a major factor when implementing new tools and procedures. Milling time of the robot was not a major consideration when developing the system. Now that the system was shown to be accurate, a faster Stewart platform would be used as well as refinements to the code to improve efficiency could be explored. Different style cutter heads should be tested to see if they help remove material faster or in a smoother fashion [48], [49].

CAE simulation software could be utilized to eliminate the need of the calibration phase. With a properly defined CAD that matches the surgical setup, the robot could virtually be moved through the Cartesian path to instantly generate a load path. This would eliminate the entire calibration set-up and run time.

Currently, two flexible strips are used and they meet at one load cell. A second load cell could be added so that one flexible strip went to one load cell. By having each load cell measure only one separate flexible strip, redundancies could be built into the system. The load cell measurements would need to agree and adjustments could be made when they do not. This would help to identify if either flexible strip is being pushed on by soft tissue for example.

www.manaraa.com

Next logical steps are to perform similar tests to Chapter 4 in cadaveric scapulae to validate the surgical system on actual bone. This will likely require further development of the patient specific mount. Adjustments of the design based on the anatomy and the surgical field of view will need to be considered of a patient specific mount that would be used in a surgical setting.

Finally, the robotic system design will need to comply with Health Canada and Food and Drug Administration guidelines. Similar steps can be taken as outline by Qin et al., in 2016 [50] to ensure compliance with medical guidelines. This will include shrouding the robot, load cell and positioning arm. The flexible components, while not going into the body, would be beneficial to be made of rust resistant material such a nickel-titanium. With the cadaveric testing and improvements to the design, it is hoped that this surgical system can eventually be adopted into the OR and used for total shoulder replacement procedures.

www.manaraa.com

REFERENCES

[1] T. Wilkes, W. Ben Kibler, and A. D. Sciascia, “Anatomy of the Scapula BT - Disorders of the Scapula and Their Role in Shoulder Injury: A Clinical Guide to Evaluation and Management,” W. Ben Kibler and A. D. Sciascia, Eds. Cham: Springer International Publishing, 2017, pp. 3–6.

[2] I. A. F. Stokes, *Research Into Spinal Deformities 2*, no. v. 2. IOS Press, 1999.

[3] E. M. Padegimas, “Future patient demand for shoulder arthroplasty by younger patients: national projections.,” *Clin. Orthop. Relat. Res.*, vol. 473, no. 6, pp. 1860–1867, Jun. 2015.

[4] M. J. Carter, T. R. Mikuls, S. Nayak, E. V Fehringer, and K. Michaud, “Impact of Total Shoulder Arthroplasty on Generic and Shoulder-Specific Health-Related Quality-of-Life Measures: A Systematic Literature Review and Meta-Analysis,” *J. Bone Joint Surg. Am.*, vol. 94, no. 17, pp. e1271-9, 2012.

[5] S. S. Hasan, J. M. Leith, B. Campbell, R. Kapil, K. L. Smith, and F. A. Matsen, “Characteristics of unsatisfactory shoulder arthroplasties,” *J. Shoulder Elb. Surg.*, vol. 11, no. 5, pp. 431–441, 2002.

[6] N. Bonnevialle *et al.*, “Aseptic glenoid loosening or failure in total shoulder arthroplasty: Revision with glenoid reimplantation,” *J. Shoulder Elb. Surg.*, vol. 22, no. 6, pp. 745–751, 2013.

[7] J. M. Wiater and M. H. Fabing, “Shoulder arthroplasty: prosthetic options and indications.,” *J. Am. Acad. Orthop. Surg.*, vol. 17, no. 7, pp. 415–425, 2009.

[8] P. H. Flurin, M. Janout, C. P. Roche, T. W. Wright, and J. Zuckerman, “Revision of the loose glenoid component in anatomic total shoulder arthroplasty,” *Bull. NYU Hosp. Jt. Dis.*, vol. 71, no. SUPPL. 2, pp. 68–76, 2013.

[9] A. Karelse, S. Leuridan, A. Van Tongel, I. M. Piepers, P. Debeer, and L. F. De Wilde, “A glenoid reaming study: How accurate are current reaming techniques?,” *J. Shoulder Elb. Surg.*, vol. 23, no. 8, pp. 1120–1127, 2014.

[10] A. R. Hopkins, U. N. Hansen, A. A. Amis, and R. Emery, “The effects of glenoid component alignment variations on cement mantle stresses in total shoulder arthroplasty,” *J. Shoulder Elb. Surg.*, vol. 13, no. 6, pp. 668–675, 2004.

[11] J. E. Lang *et al.*, “Robotic systems in orthopaedic surgery.,” *J. Bone Joint Surg. Br.*, vol. 93, no. 10, pp. 1296–9, 2011.

[12] D. J. Jacofsky and M. Allen, “Robotics in Arthroplasty: A Comprehensive Review,” *J. Arthroplasty*, vol. 31, no. 10, pp. 2353–2363, 2016.

[13] N. Sugano, “Computer-assisted orthopaedic surgery and robotic surgery in total

www.manaraa.com

hip arthroplasty," *Clin Orthop Surg*, vol. 5, no. 1, pp. 1–9, 2013.

[14] W. L. W. L. Bargar, "Primary and revision total hip replacement using the Robodoc system.," *Clin. Orthop. Relat. Res.*, no. 354, pp. 82–91, Sep. 1998.

[15] H. A. H. A. Paul, "Development of a surgical robot for cementless total hip arthroplasty.," *Clin. Orthop. Relat. Res.*, no. 285, pp. 57–66, Dec. 1992.

[16] E. H. E. H. Spencer, "The ROBODOC clinical trial: a robotic assistant for total hip arthroplasty.," *Orthop. Nurs.*, vol. 15, no. 1, pp. 9–14, Jan. 1996.

[17] M. Nogler, H. Maurer, C. Wimmer, C. Gegenhuber, C. Bach, and M. Krismer, "Knee pain caused by a fiducial marker in the medial femoral condyle.," *Acta Orthop. Scand.*, vol. 72, no. 5, p. 477–477 1p, 2001.

[18] N. Nakamura, N. Sugano, T. Nishii, H. Miki, A. Kakimoto, and M. Yamamura, "Robot-assisted primary cementless total hip arthroplasty using surface registration techniques: A short-term clinical report," *Int. J. Comput. Assist. Radiol. Surg.*, vol. 4, no. 2, pp. 157–162, 2009.

[19] E.-K. E. K. Song, "Robotic-assisted TKA reduces postoperative alignment outliers and improves gap balance compared to conventional TKA.," *Clin. Orthop. Relat. Res.*, vol. 471, no. 1, pp. 118–126, Jan. 2013.

[20] S. Nishihara, N. Sugano, T. Nishii, H. Miki, N. Nakamura, and H. Yoshikawa, "Comparison Between Hand Rasping and Robotic Milling for Stem Implantation in Cementless Total Hip Arthroplasty," *J. Arthroplasty*, vol. 21, no. 7, pp. 957–966, 2006.

[21] R. Tarwala and L. D. Dorr, "Robotic assisted total hip arthroplasty using the MAKO platform," *Curr. Rev. Musculoskelet. Med.*, vol. 4, no. 3, p. 151, 2011.

[22] B. S.W., A. I., J. B., M. A., and R. P., "Improved accuracy of component positioning with robotic-assisted unicompartmental knee arthroplasty," *J. Bone Jt. Surg. - Am. Vol.*, vol. 98, no. 8, pp. 627–635, 2016.

[23] J. H. Lonner, J. R. Smith, F. Picard, B. Hamlin, P. J. Rowe, and P. E. Riches, "High Degree of Accuracy of a Novel Image-free Handheld Robot for Unicondylar Knee Arthroplasty in a Cadaveric Study," *Clin. Orthop. Relat. Res.*, vol. 473, no. 1, pp. 206–212, 2015.

[24] J. Bodner, H. Wykypiel, G. Wetscher, and T. Schmid, "First experiences with the da Vinci??? operating robot in thoracic surgery," *Eur. J. Cardio-thoracic Surg.*, vol. 25, no. 5, pp. 844–851, 2004.

[25] W. Birkfellner, F. Watzinger, F. Wanschitz, R. Ewers, and H. Bergmann, "Calibration of Tracking Systems in a Surgical Environment," vol. 17, no. 5, pp. 737–742, 1998.

www.manaraa.com

[26] Z. Yaniv, E. Wilson, D. Lindisch, and K. Cleary, “Electromagnetic tracking in the clinical environment,” *Med Phys*, vol. 36, no. 3, pp. 876–892, 2009.

[27] A. D. Wiles, D. G. Thompson, and D. D. Frantz, “Accuracy assessment and interpretation for optical tracking systems,” *Med. Imaging 2004 Vis. Image-guided Preced. Display. Proc. SPIE*, vol. 5367, pp. 421–432, 2004.

[28] M. M. G. Mazumder, S. Kim, S. J. Park, and J. Lee, “Precision and repeatability analysis of optotrak certus as a tool for gait analysis,” *IFAC Proc. Vol.*, vol. 10, no. PART 1, pp. 107–112, 2007.

[29] P. J. Barnes, C. Baldock, S. R. Meikle, and R. R. Fulton, “Benchmarking of a motion sensing system for medical imaging and radiotherapy.,” *Phys. Med. Biol.*, vol. 53, no. 20, pp. 5845–5857, 2008.

[30] J.-Y. Jin, F.-F. Yin, S. E. Tenn, P. M. Medin, and T. D. Solberg, “Use of the BrainLAB ExacTrac X-Ray 6D System in Image-Guided Radiotherapy,” *Med. Dosim.*, vol. 33, no. 2, pp. 124–134, 2008.

[31] T. Koivukangas, J. P. A. Katisko, and J. P. Koivukangas, “Technical accuracy of optical and the electromagnetic tracking systems,” *Springerplus*, vol. 2, p. 90, Mar. 2013.

[32] A. Şumnu, Đ. H. Güzelbey, and M. V. Çakır, “Simulation and PID control of a Stewart platform with linear motor †,” vol. 31, no. 1, pp. 345–356, 2017.

[33] M. A. Amir Ghobakhloo M. Eghtesad, “Position control of a Stewart-Gough platform using inverse dynamics method with full dynamics,” pp. 1–7, 2001.

[34] L.-W. Tsai, *Robot Analysis : The Mechanics of Serial and Parallel Manipulators / L.-W. Tsai*. 1999.

[35] S. Sasaki, “On numerical techniques for kinematics problems of general serial-link robot manipulators,” *Robotica*, vol. 12, no. 4, pp. 309–322, 1994.

[36] J. J. Craig, *Introduction to Robotics: Mechanics and Control*, 2nd ed. Boston, MA, USA: Addison-Wesley Longman Publishing Co., Inc., 1989.

[37] I. Muller, R. M. de Brito, C. E. Pereira, and V. Brusamarello, “Load cells in force sensing analysis -- theory and a novel application,” *IEEE Instrum. Meas. Mag.*, vol. 13, no. 1, pp. 15–19, 2010.

[38] M. Stokes, “Robot Navigation by Bending Forces and Torques,” University of Western Ontario, 2015.

[39] P. Cominos and N. Munro, “PID controllers : recent tuning methods and design to specification,” *Control*, vol. 149, no. I. pp. 46–53, 2002.

www.manaraa.com

[40] O. Ciobanu, W. Xu, and G. Ciobanu, “the Use of 3D Scanning and Rapid Prototyping In Medical Engineering,” *Acad. Brâncuşi*, no. 1, pp. 241–247, 2013.

[41] P. V BOLSTAD, P. GESSLER, and T. M. LILLESAND, “Positional uncertainty in manually digitized map data,” *Int. J. Geogr. Inf. Syst.*, vol. 4, no. 4, pp. 399–412, Oct. 1990.

[42] G. Walch, R. Badet, A. Boulahia, and A. Khoury, “Morphologic study of the Glenoid in primary glenohumeral osteoarthritis,” *J. Arthroplasty*, vol. 14, no. 6, pp. 756–760, 1999.

[43] “TORNIER AEQUALIS™ PERFORM Anatomic Glenoid System Surigcal Technique.” Wright Medical Group, 2017.

[44] “TORNIER AEQUALIS PERFORM + CORTILOC™ Augmented Glenoid SURGICAL TECHNIQUE.” Wright Medical Group, 2017.

[45] Y. He, B. Liang, J. Yang, S. Li, and J. He, “An Iterative Closest Points Algorithm for Registration of 3D Laser Scanner Point Clouds with Geometric Features,” *Sensors*, vol. 17, no. 8, p. 1862, 2017.

[46] E. A. Lalone, T. M. Peters, G. W. King, and J. A. Johnson, “Accuracy assessment of an imaging technique to examine ulnohumeral joint congruency during elbow flexion,” *Comput. Aided Surg.*, vol. 17, no. 3, pp. 142–152, 2012.

[47] L. Chkhartishvili and G. Suryamurthy, *Volume of intersection of six spheres: A special case of practical interest*, vol. 11. 2015.

[48] J. R. Kusins, O. R. Tutunea-Fatan, and L. M. Ferreira, “Experimental analysis of the process parameters affecting bone burring operations,” *Proc. Inst. Mech. Eng. Part H J. Eng. Med.*, p. 954411917742943, Nov. 2017.

[49] J. Kusins, “Experimenal Analysis of Parameters Influencing the Bone Burring Process,” 2015.

[50] Q. L.-Y., W. J.Z., and C. C.-S., “Housing design and testing of a surgical robot developed for orthopaedic surgery,” *J. Orthop. Transl.*, vol. 5, pp. 72–80, 2016.

www.manaraa.com

APPENDICES

APPENDIX A: Assembly Exploded Views

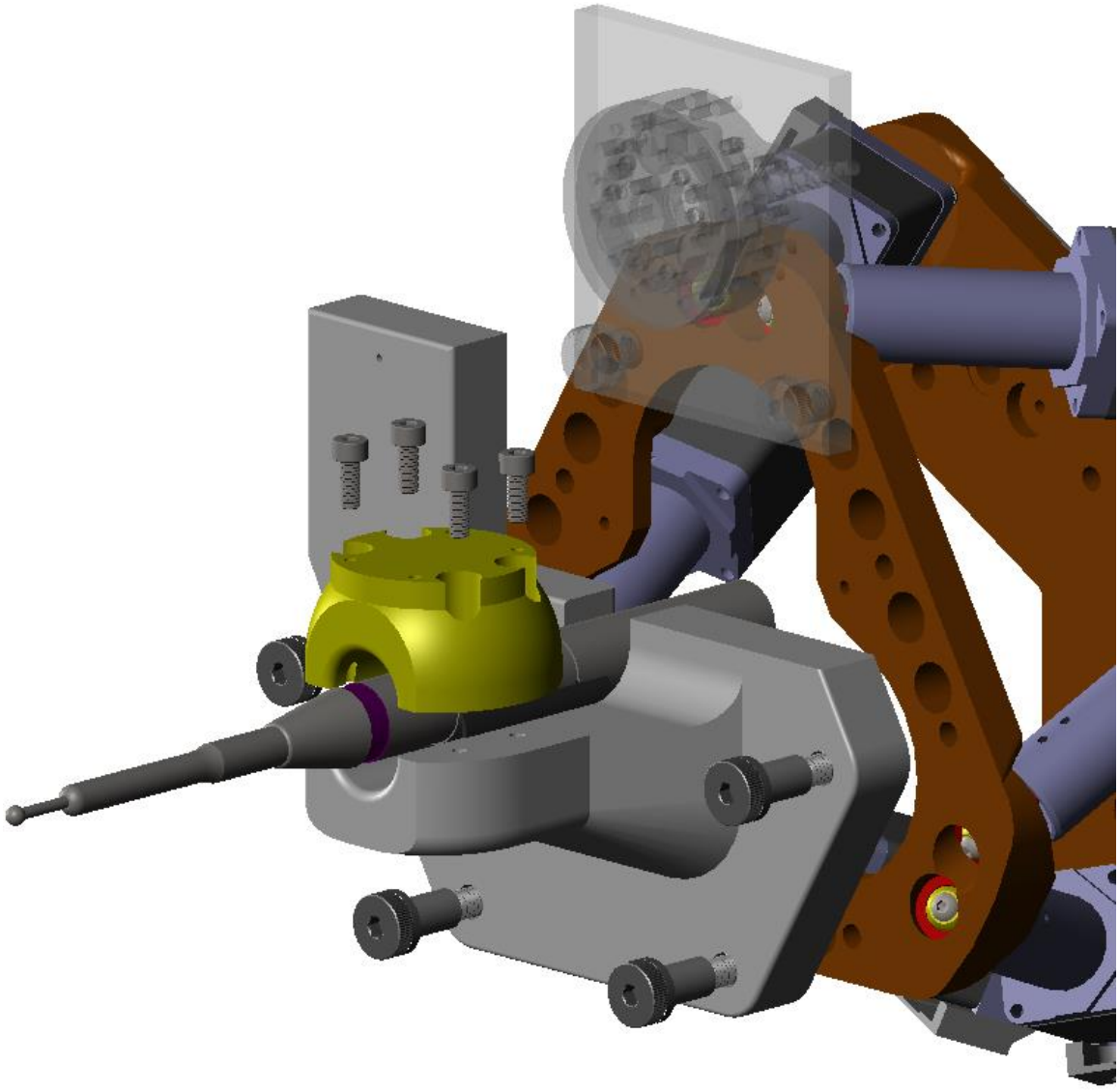

Figure A-1: Tool mount assembly

www.manaraa.com

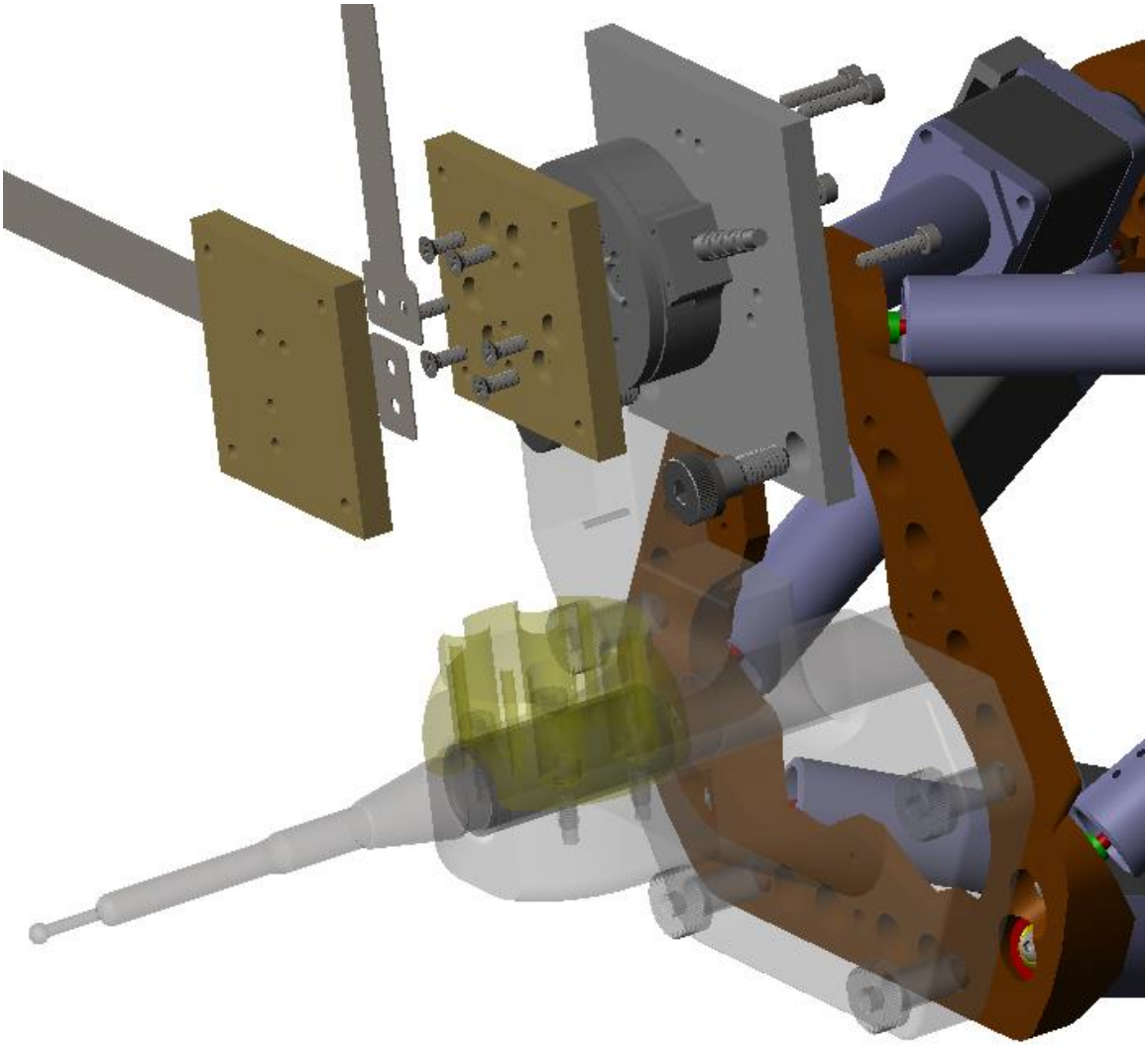

Figure A-2: Load cell and flexible component exploded view assembly

www.manaraa.com

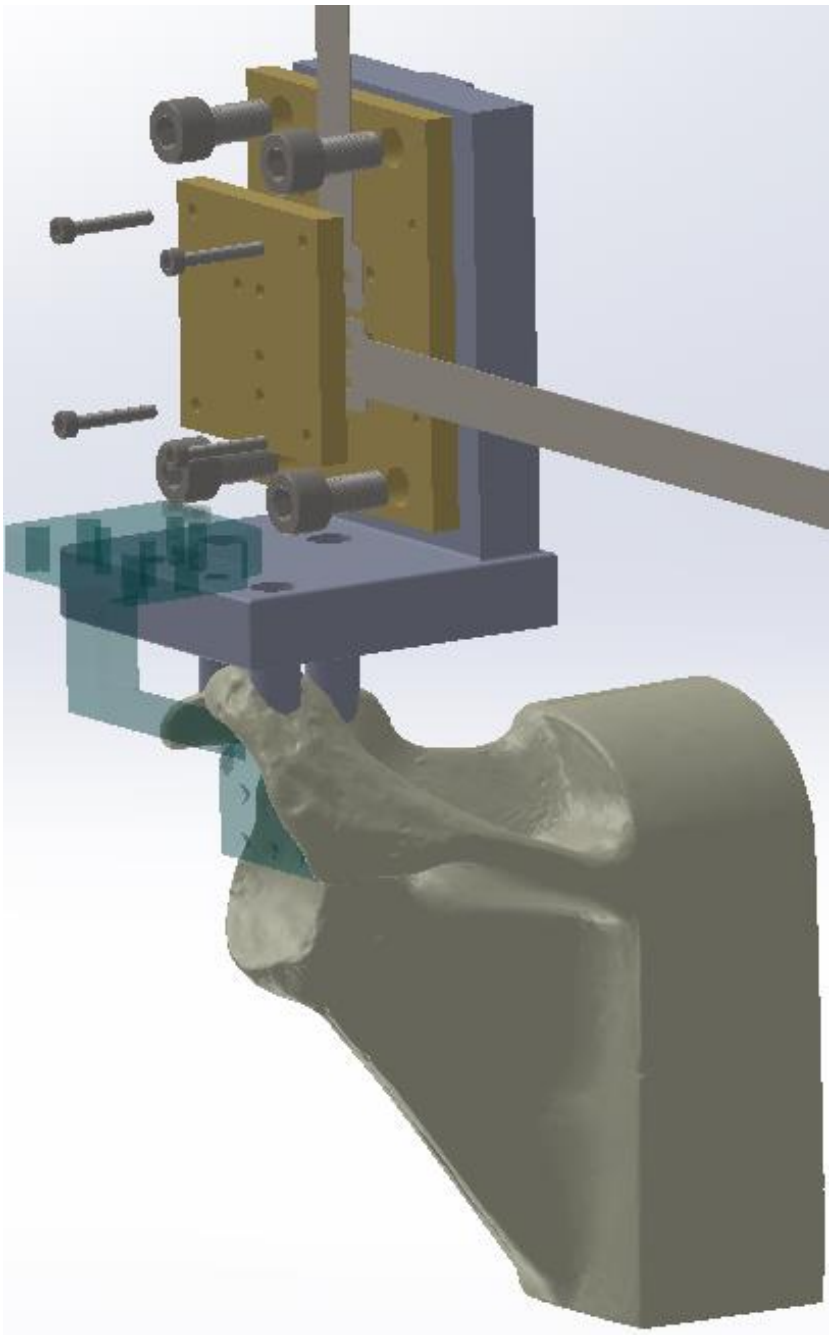

Figure A-3: Patient flexible component exploded view assembly

www.manaraa.com

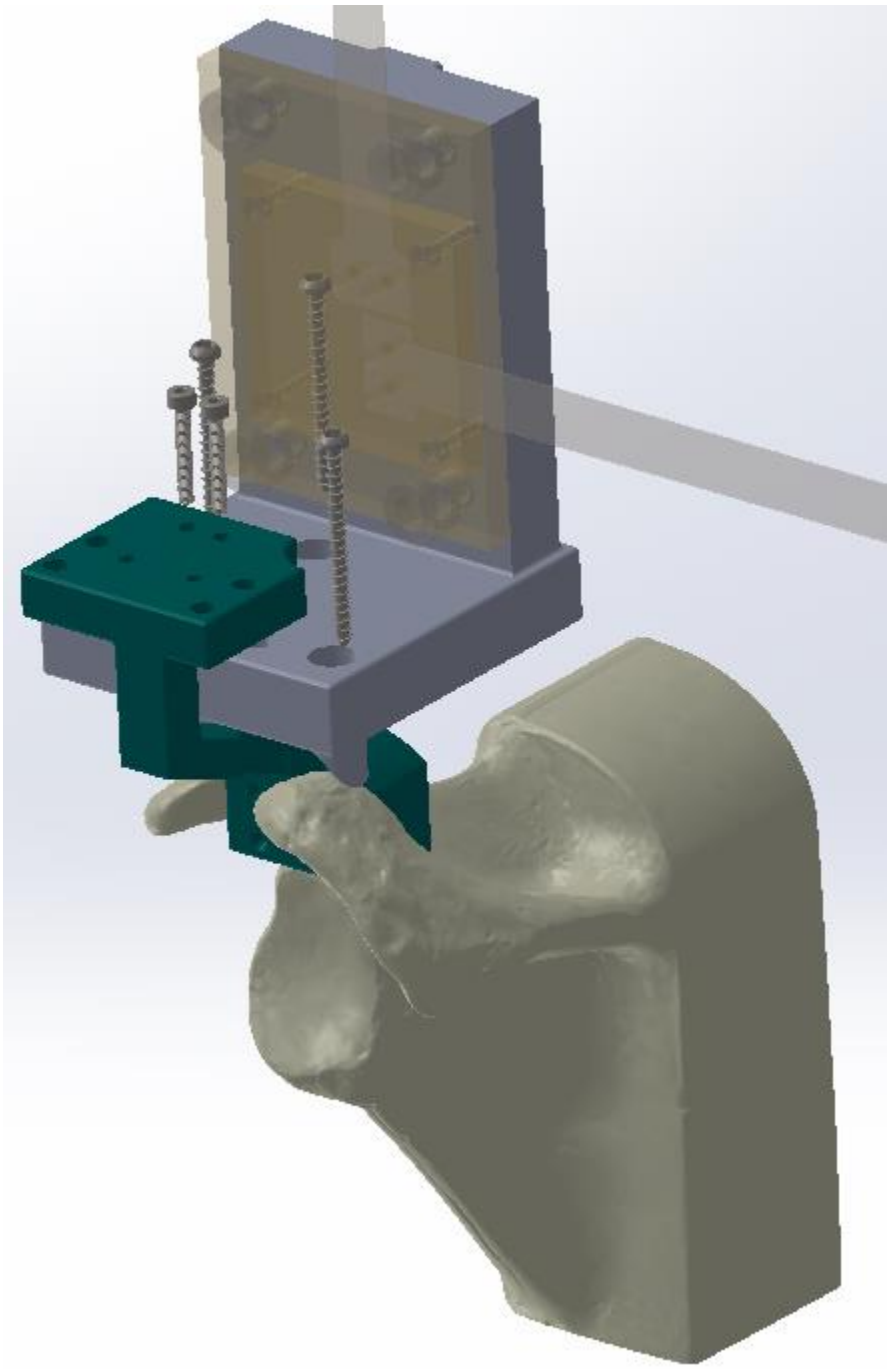

Figure A-4: Patient specific mount exploded view assembly

www.manaraa.com

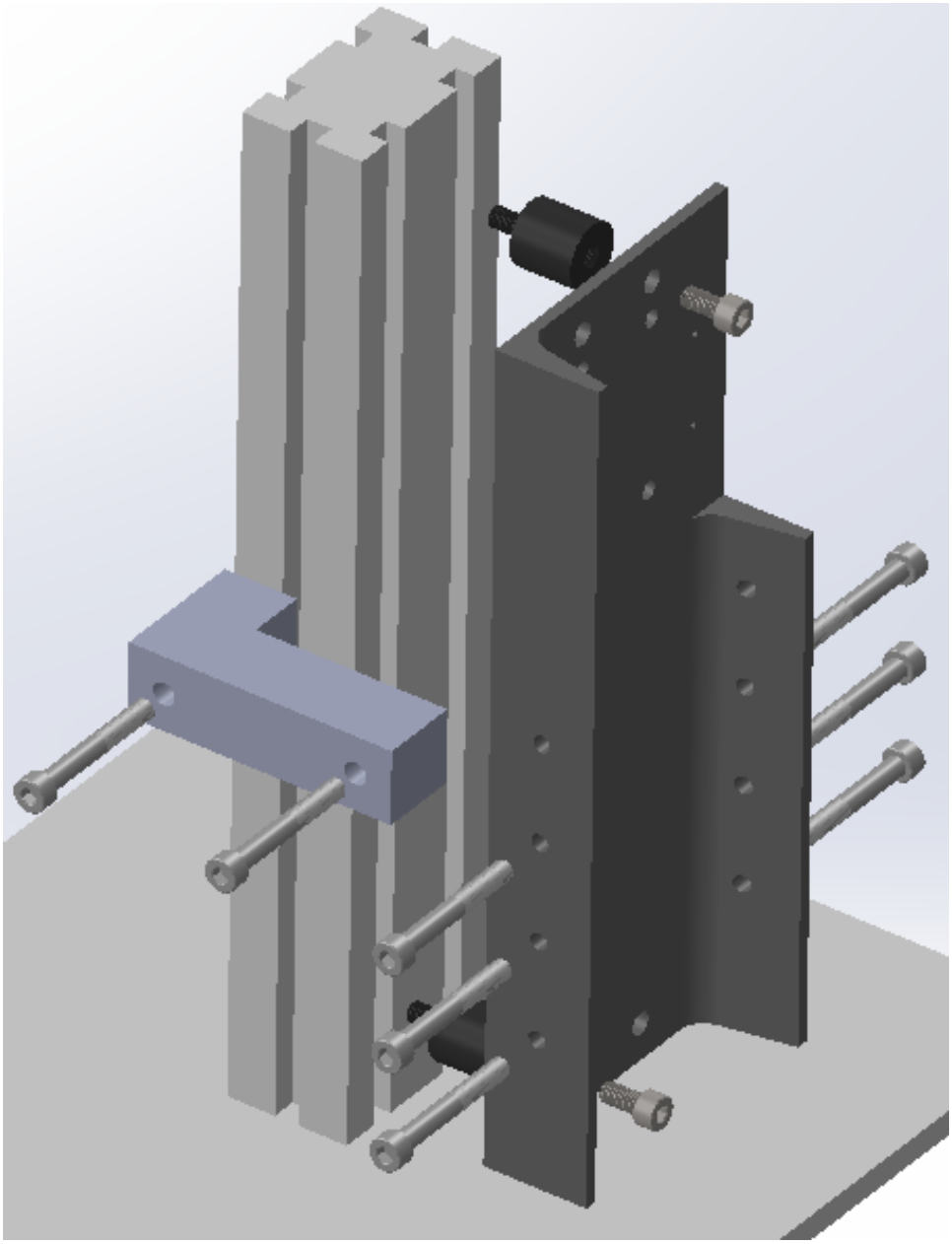

Figure A-5: Flexible mount exploded view

www.manaraa.com

To adapt the end connector of the Spider2 to attach to the robot, a special connector was designed. This connector goes around the cylindrical end connector of the Spider2 and presses it tightly using two parts and four bolts. As well, there was a larger set screw to prevent any rotation in this clamp part. Finally, two bolt holes are made on the ends of the elongated part to attach to the handle component of the robot. This connector was 3D printed in black PLA and can be seen in Figure A-6. Other adaptors could easily be designed and made for other limb positioners if an OR has a different model.

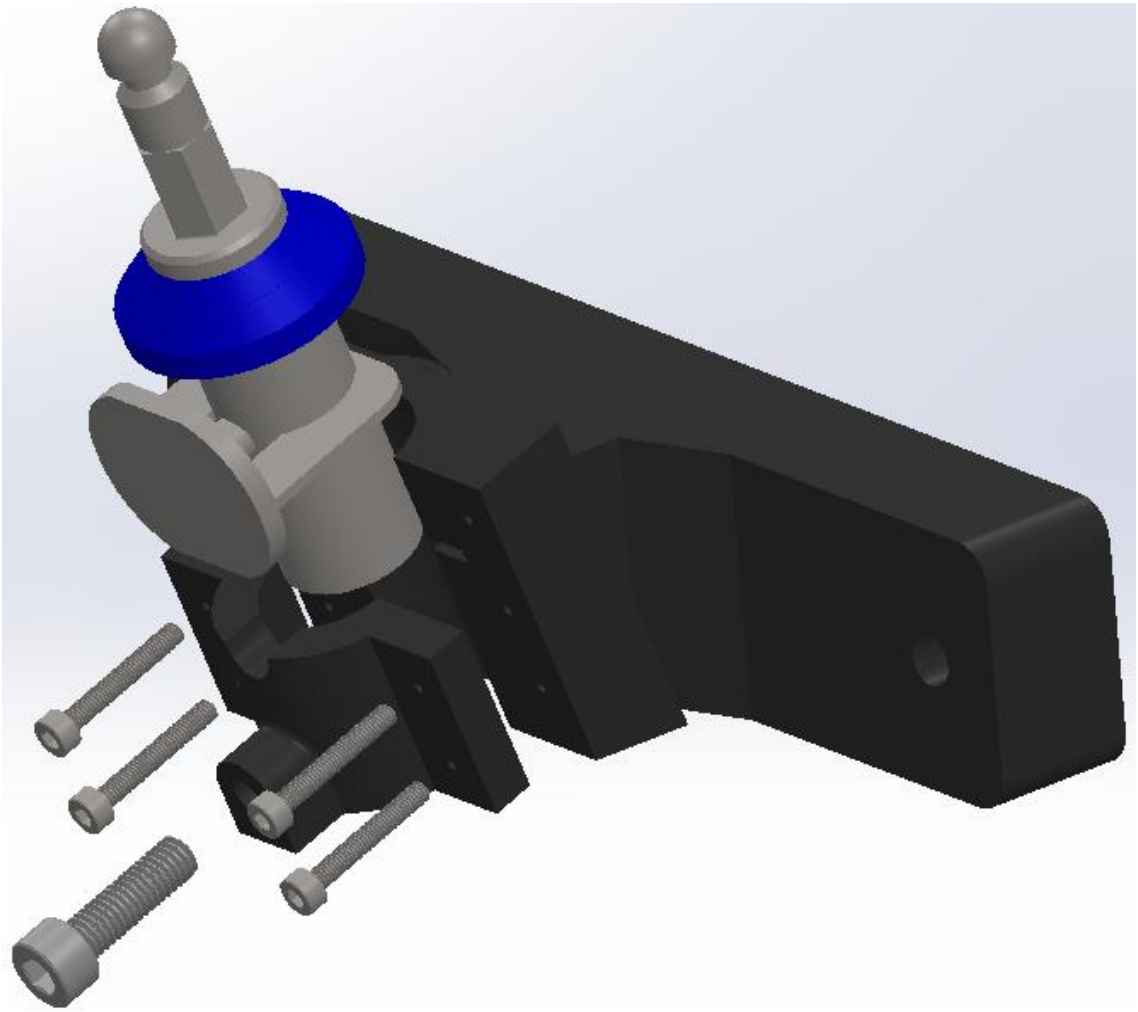

Figure A-6: Spider2 adaptor to connect to robot

www.manaraa.com

APPENDIX B: Hardware Design

A six axis Mini45 load cell from ATI (ATI Technologies, Markham, Ontario) was selected as the load sensing component. The Mini45 has 1/4 N resolution in X, Y and Z directions and sensing ranges up to 580 N in X and Y and 1160 N in Z. The load cell was connected through a 26-pin cable to the ATI power supply which was then plugged into a 120V source. The power supply was also connected to the National Instruments (National Instruments Corporation, Austin, Texas) USB-6211 data acquisition unit (DAQ). The DAQ was wired based on the company standards and was then connected through a Universal Serial Bus (USB) to the desktop computer.

The Stewart Platform was connected to the actuator controller through a 44-pin cable. The controller was plugged into a 120V and was also plugged into a desktop computer through USB cable. The hardware system can be seen in Figure B-1.

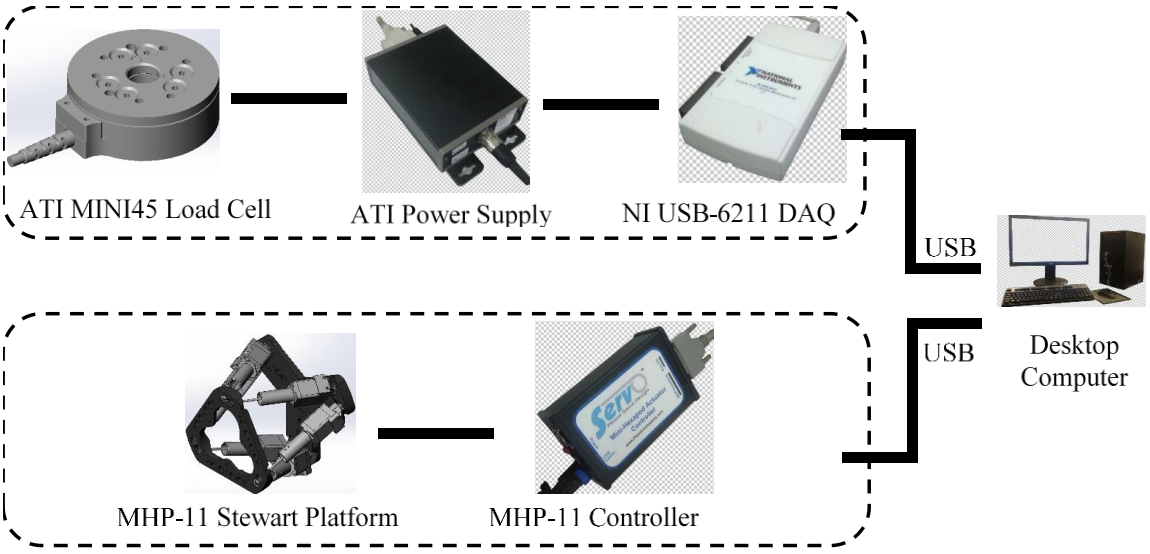

Figure B-1: Hardware Configuration

Load sensing setup shown in the upper path, robot manipulator setup shown in the lower path

www.manaraa.com

APPENDIX C: Drawings

The flexible components were made from wear-resistant 304 spring string. The part was made using a wire cutter. The ends of the component was made to help lock into the clamps that will be discussed later. A drawing of the flexible component can be seen in Figure C-1.

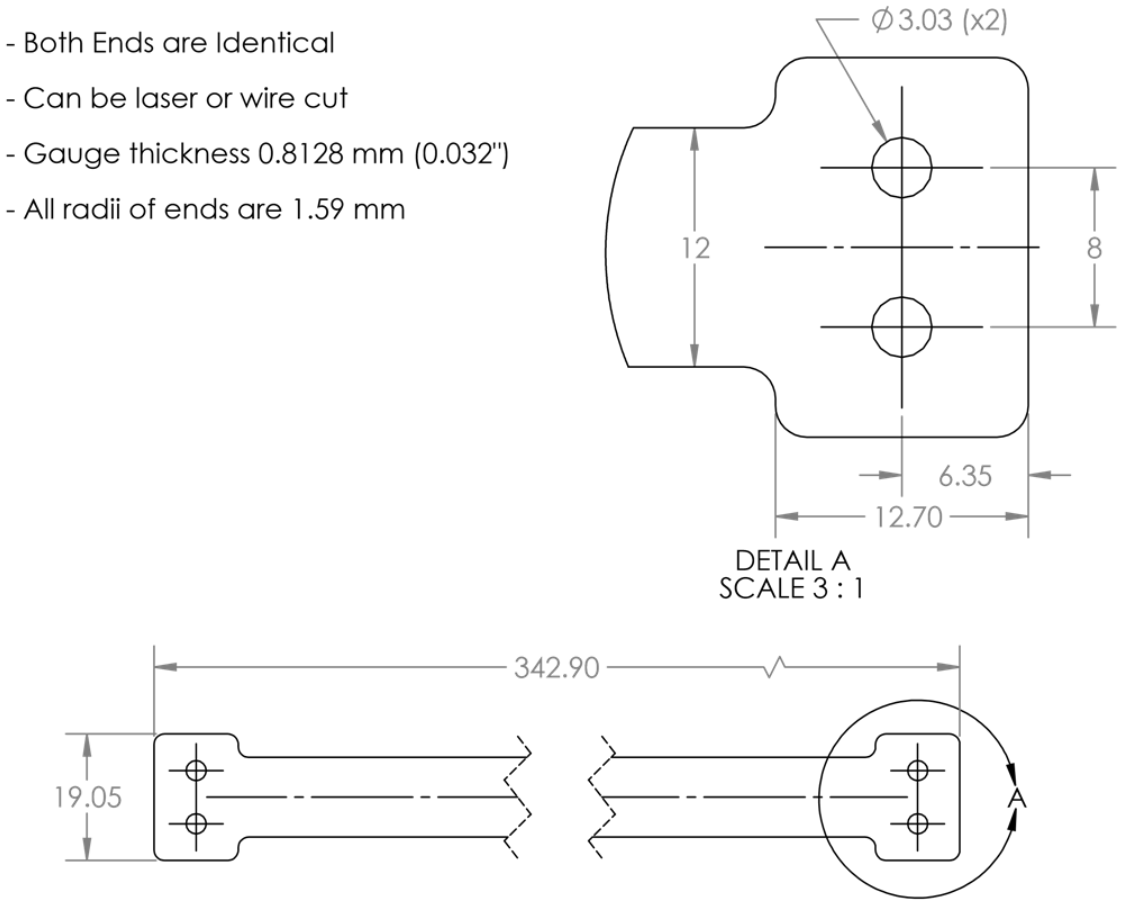

Figure C-1: Flexible component spring steel

www.manaraa.com

The flexible components were secured from one side using a machined brass component that fit to the shape of the end of the spring steel. Two components were made from this part with one being mirrored to accommodate the change in orientation from one end versus the other. The flexible component cover can be seen in Figure C-2.

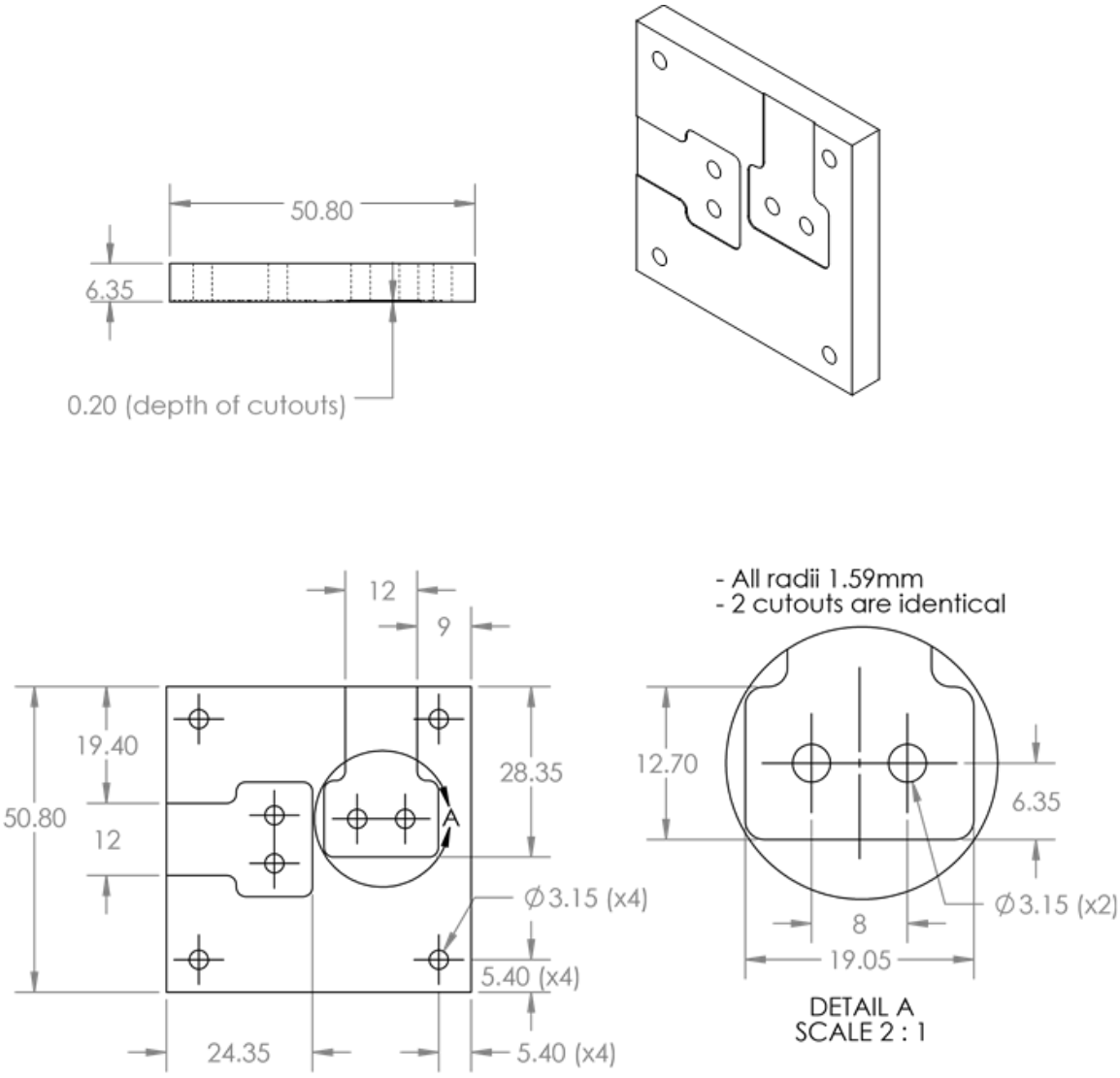

Figure C-2: Flexible component cover

www.manaraa.com

Where the one end of the flexible components attaches to the load cell on the robot, another machined brass component was attached between the load cell and the flexible components. The circle pattern of holes was used to attach to the load cell while the corner holes are used with the cover to clamp the flexible components. The load cell/flexible component bracket can be seen in Figure C-3.

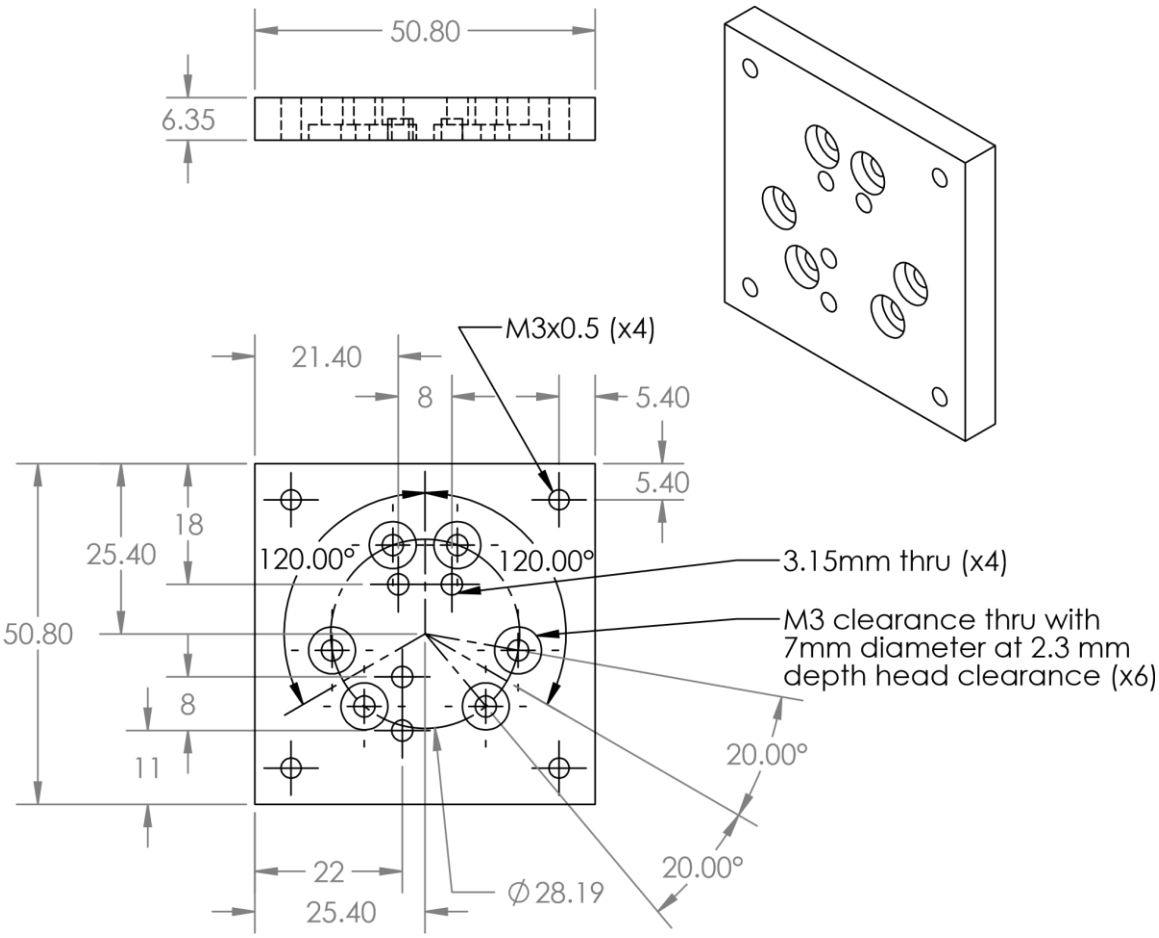

Figure C-3: Load cell/spring steel bracket

www.manaraa.com

To attach the load cell to the robot a delrin bracket was machined. The bracket has a circular hole pattern that the load cell was bolted to. As well, two bolt holes at the bottom of the bracket to bolt to the robot. The load cell bracket attachment can be seen in Figure C-4.

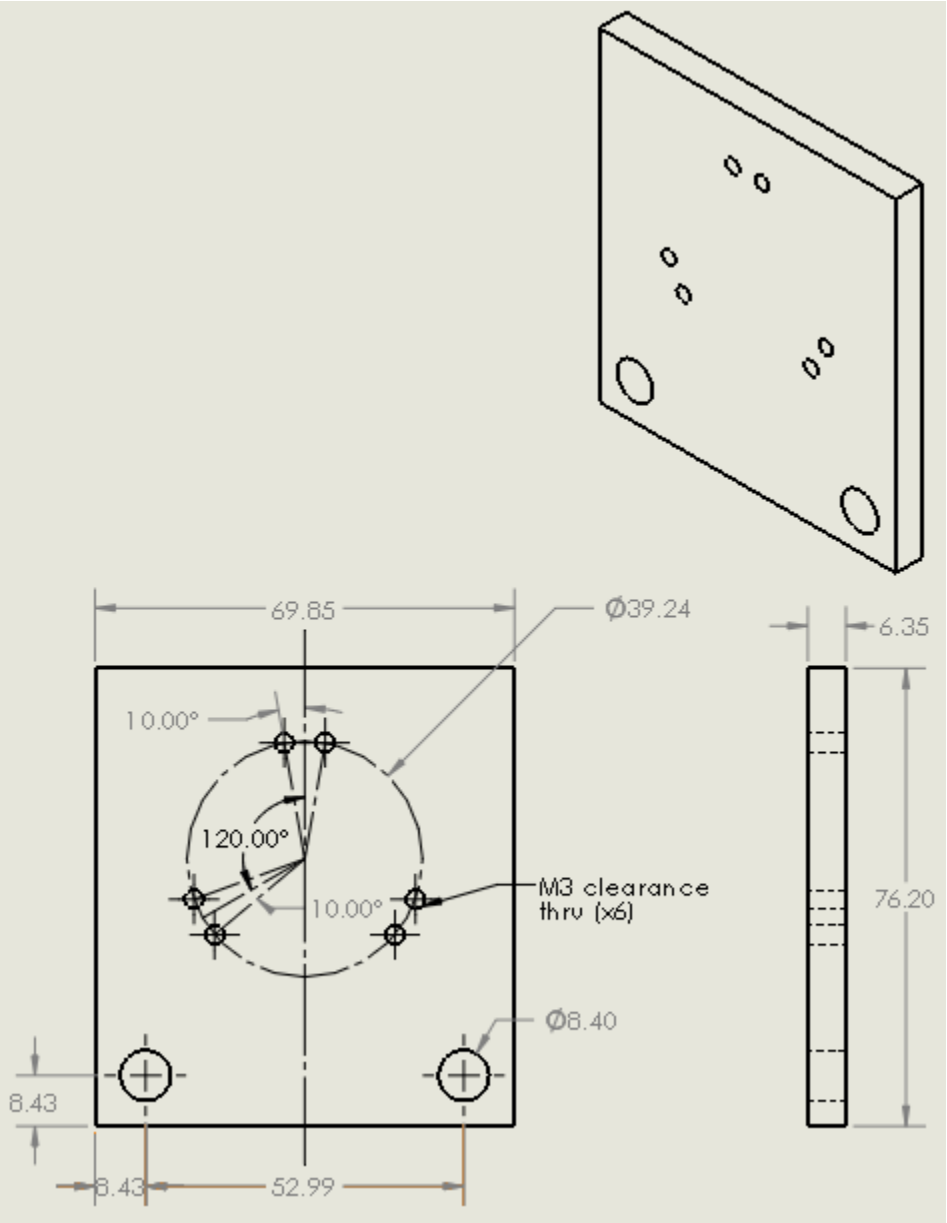

Figure C-4: Load cell bracket attachment to robot

www.manaraa.com

The patient specific mount was a complex component that was custom to each scapula. Due to the complexity the component, it was 3D printed using a Formlabs printed in what they refer to as stiff material. An example of a patient specific mount for a normal scapula model can be seen in Figure C-5. Since it was 3D printed and the part was custom, dimensions are adjusted and many were not shown.

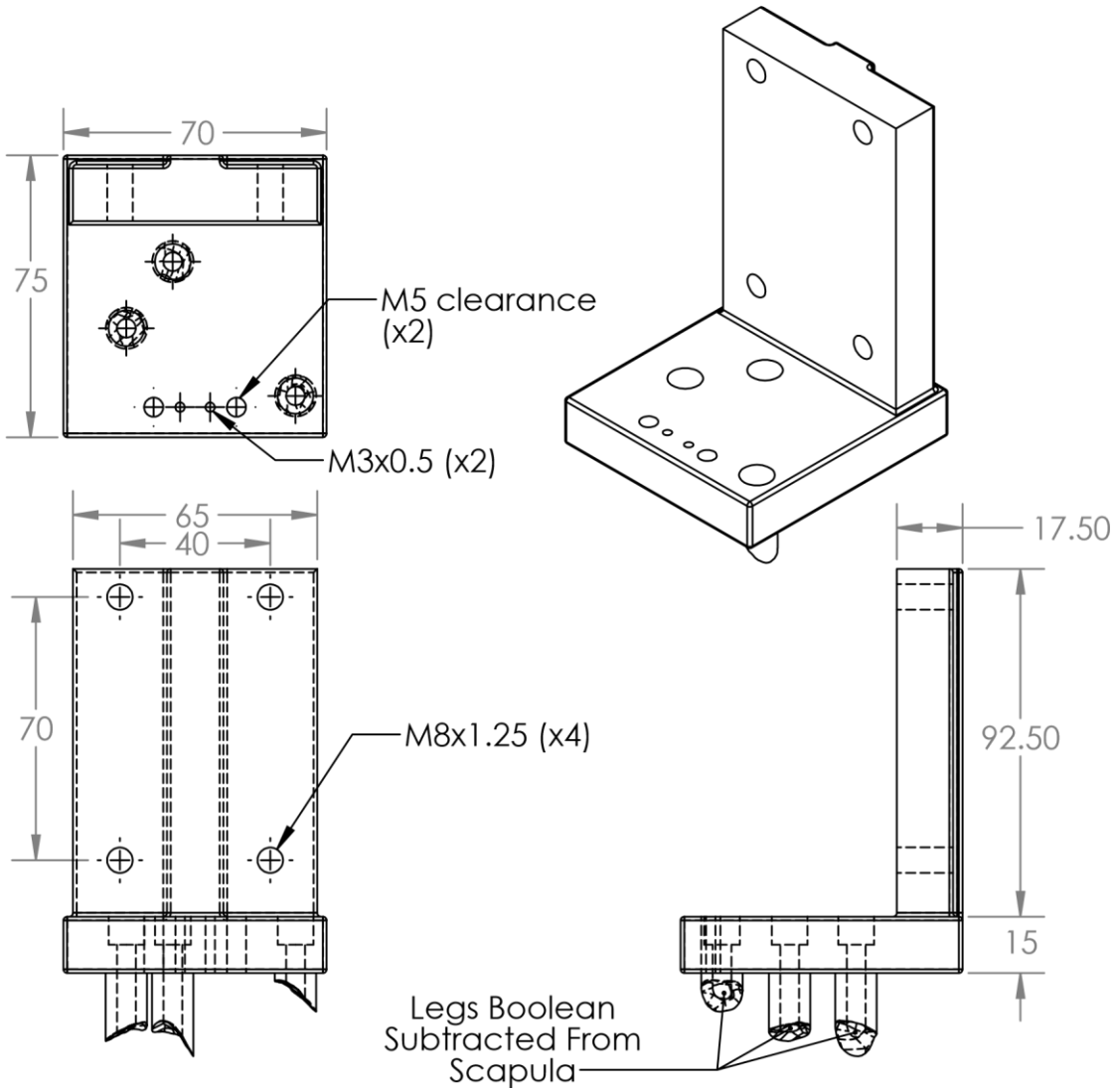

Figure C-5: Patient specific mount for normal scapula

www.manaraa.com

The glenoid mount was also custom to the scapula model. The part was 3D printed in the same stiff material on a Formlabs printer. Again due to this part being 3D printed and the part always changing based on the scapula model, many dimensions were not shown. An example of the glenoid model for a normal scapula model can be seen in Figure C-6.

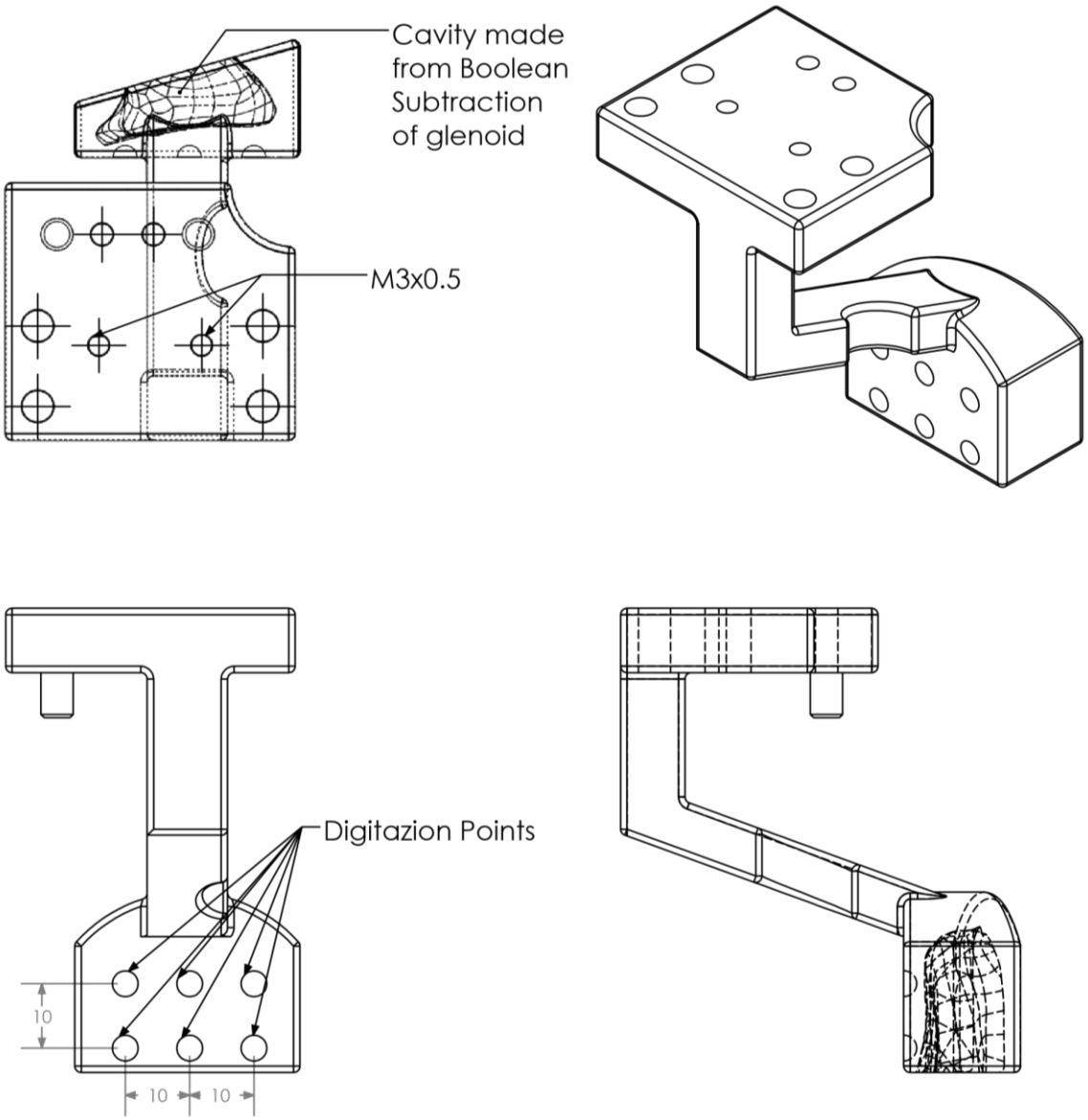

Figure C-6: Glenoid mount for normal scapula model

www.manaraa.com

The other end of the flexible components attaches to the patient. An additional brass bracket was machined that attaches to the patient specific mount and clamps to the flexible component cover. The patient specific mount bracket can be seen in Figure C-7.

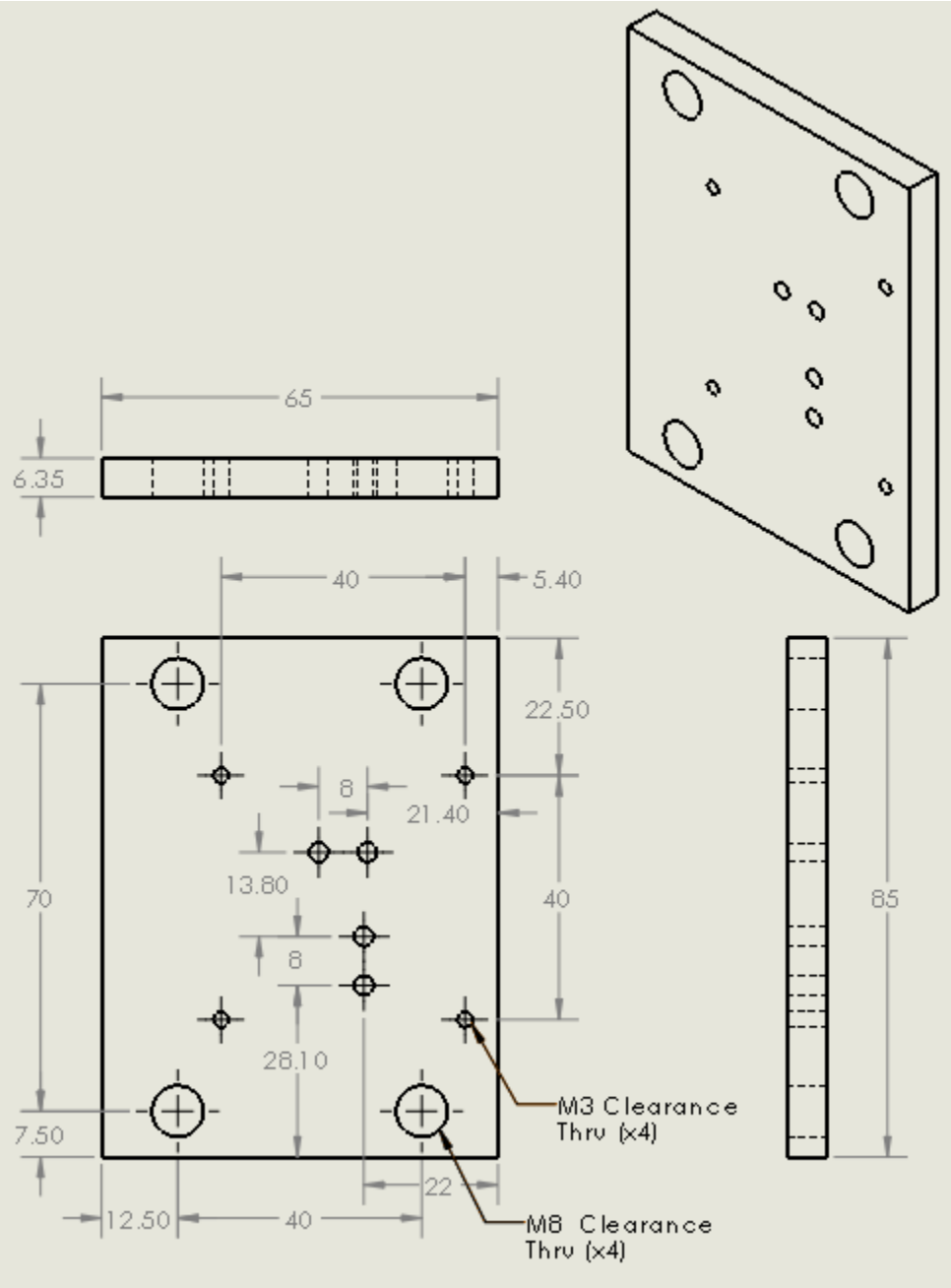

Figure C-7: Patient mount flexible mount bracket

www.manaraa.com

To hold the burring tools in plane, two components were used. The first component attached to the robot through clearance bolt holes. A channel down the middle allows the burring tool to align with the z axis of the robot. This component was extrusion 3D printed in ABS and most dimensions were left off as the part was 3D printed. The bottom tool mount can be seen in Figure C-8.

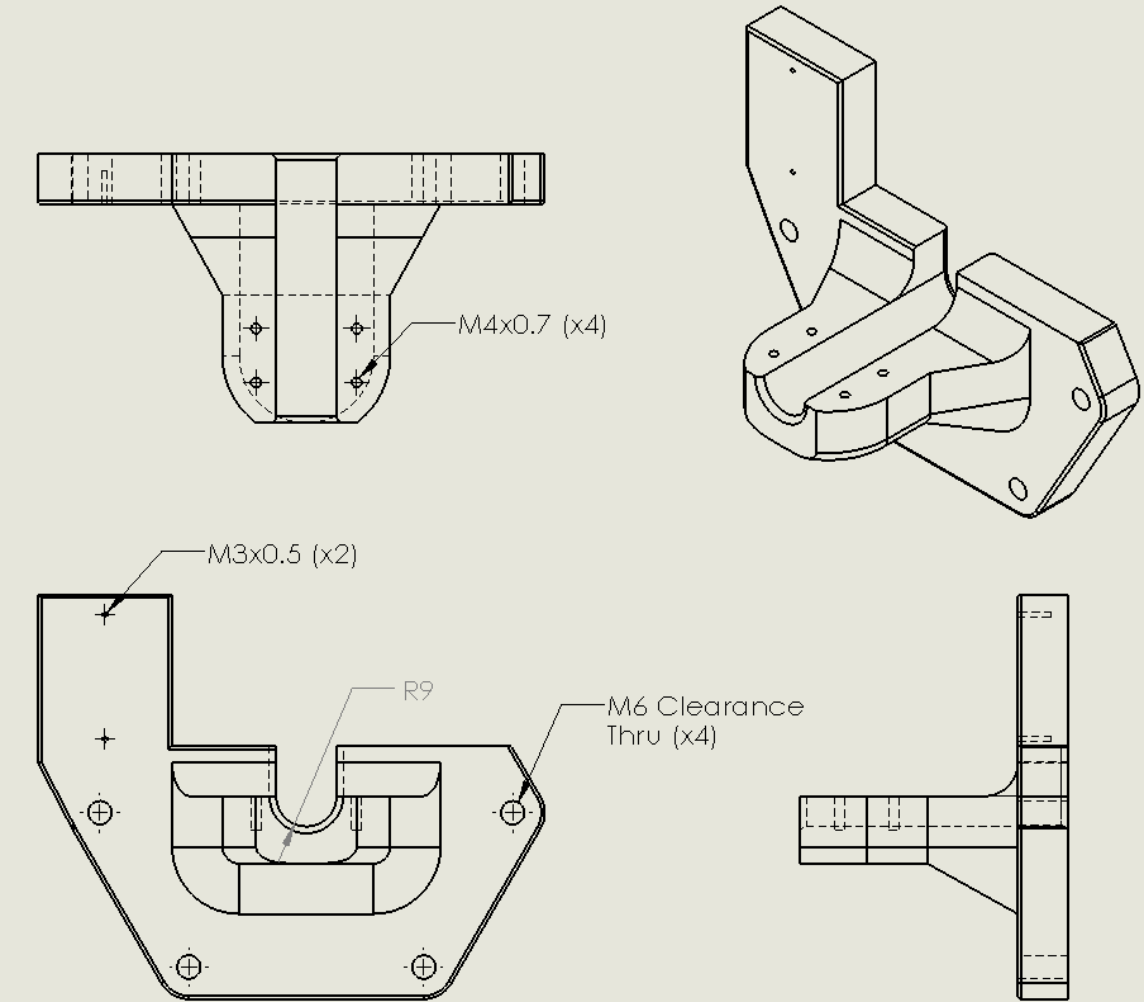

Figure C-8: Bottom tool mount

www.manaraa.com

The second component to hold the burring tool was a cover that went on top of the tool and bolted into the bottom tool mount. A channel through the bottom part allowed the part to fit around the tool. This part was extrusion 3D printed in ABS. The top tool cover can be seen in Figure C-9.

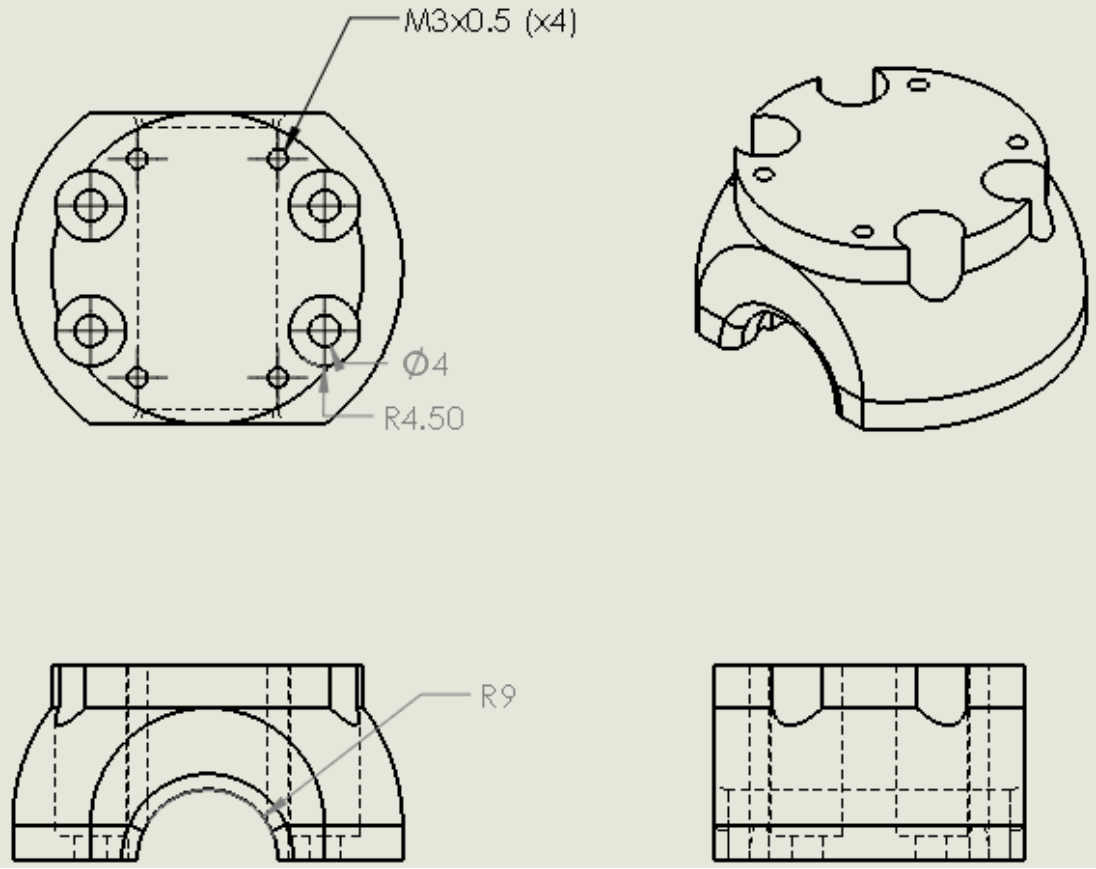

Figure C-9: Top tool mount

www.manaraa.com

For the flexible mount, the only designed component was the steel channel. A piece of a steel C channel had a section in the top corner cut away to not interfere with the spring steel flexible components. Threaded holes down the side allow bolts to hold a scapula model in place. Other holes accommodate the rubber mounts allowing the flexibility of the system. The flexible mount steel channel can be seen in Figure C-10

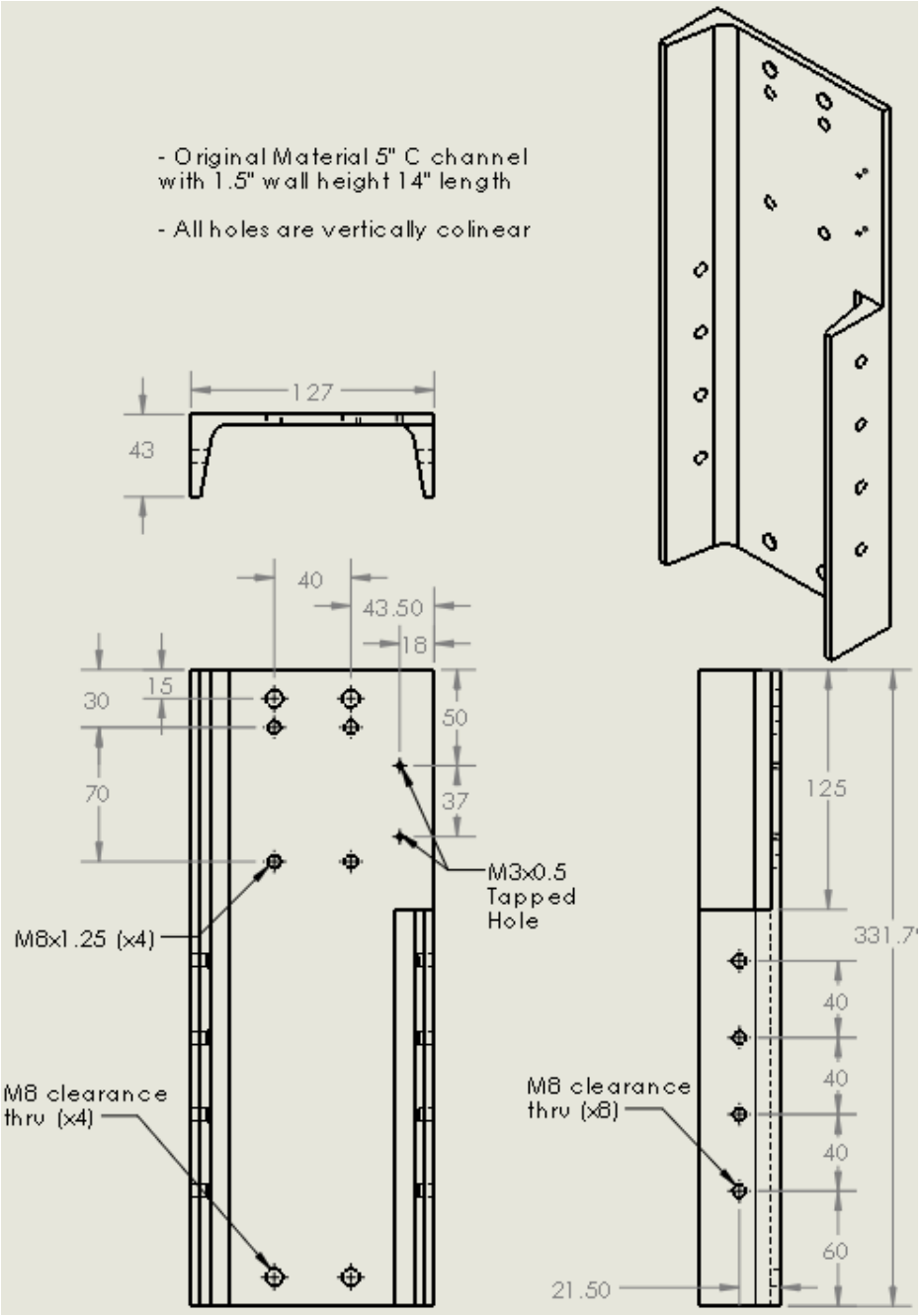

Figure C-10: Flexible mount steel channel

www.manaraa.com

APPENDIX D: Force Navigation Control Loop Code

```
for (int row = 0; row < length; row++)
{
	//===== Move to Zero/Zero Load Cell =====//
	cout << "\n=====================================================\n";
	cout << "\nNow on point: " << row + 1 << " of " << length <<"\n";
	while (1)
	{
		loopcount++;
		//========== Get Initial Loads ==========//
		for (int load_count = 1; load_count <= load_loops; load_count++)
		//takes the average of a number of loops
	{
		lc.GetLoads(loads_msr);
		//Gets loads Fx, Fy, Fz, Mx, My, Mz and stores in load_cell_values
		loads_sum[0] = static_cast<double>(loads_msr[0]) + loads_sum[0];
		loads_sum[1] = static_cast<double>(loads_msr[1]) + loads_sum[1];
		loads_sum[2] = static_cast<double>(loads_msr[2]) + loads_sum[2];
		loads_sum[3] = static_cast<double>(loads_msr[3]) + loads_sum[3];
		loads_sum[4] = static_cast<double>(loads_msr[4]) + loads_sum[4];
		loads_sum[5] = static_cast<double>(loads_msr[5]) + loads_sum[5];
		//converts the float variables to useable vector double and sums up each individual load
	}
	for (int z = 0; z <= 5; z++)
	{
		loads_sum[z] = loads_sum[z] / load_loops;   //averages each individual load
	}
	all_msr_loads.push_back(loads_sum);   //adds vector of the measured loads to the end of this variable
	all_msr_loads.push_back(loads_dsr[row]);    //adds vector of the desired loads to the end of this variable
	//====== Dsr - Msr Load Difference ======//
	for (int term = 0; term < 6; term++)
	{
		loads_delta[term] = loads_sum[term] - loads_dsr[row][term];
	}
	loads_sum = { 0, 0, 0, 0, 0, 0 }; //resets the load sum so that previous load values do not skew values

	//==================== Boolean Limit Check ==================//
	//========== Load Corrections ==========//
	for (int term = 0; term < 6; term++)
	{
		loads_delta_converted[term] = loads_delta[term] * conversion_factor[term];
	}

	try   //try and catch loop needed for error checking
	{
		//======== Check Upper Deadband =========//
		upper_deadbands = MHPSetUpperDeadbands(mhp);
		for (int term = 0; term < 6; term++)
		{
			if (loads_delta_converted[term] < &&
				loads_delta_converted[term] < upper_deadbands[term][0] * 0.25)
				//checks if value is negative and > max neg deadband creating a threshold limit
			{
				loads_delta_converted[term] = upper_deadbands[term][0] * 0.25;
				//sets value to a max step size, limits correction
			}
			if (loads_delta_converted[term] > 0 &&
				loads_delta_converted[term] > upper_deadbands[term][1] * 0.25)
				//checks if value is negative and > max neg deadband creating a threshold limit
			{
```

www.manaraa.com

```
            loads_delta_converted[term] = upper_deadbands[term][1] * 0.25;
            //sets value to a max step size, limits correction
        }
}

for (int term = 0; term < 6; term++)
{
        vec_loads_delta[term] = static_cast<double>(loads_delta[term]);
        vec_loads_delta_converted[term] = static_cast<double>(loads_delta_converted[term]);
        vec_u_limits[term] = static_cast<double>(upper_deadbands[term][1]);
        vec_l_limits[term] = static_cast<double>(upper_deadbands[term][0]);
}
all_loads_delta.push_back(vec_loads_delta);
all_loads_delta_converted.push_back(vec_loads_delta_converted);
all_u_limits.push_back(vec_u_limits);
all_l_limits.push_back(vec_l_limits);

//========= Gets Current Position From MHP Converts it =========//
variant_t pos_var = mhp->GetPositionMatrix(PositionActual, L"Reamer", L"Reamer Zero");
//gets a variant that is 2D of current position

vector<double> cur_pos = DoubleVariantToVector(pos_var);
//currents 2D variant to a useable 1D 16 term vector

cur_pos = MHPTranspose(cur_pos);
//transposes matrix vector to standard matrix form

Eigen::Matrix<float, 4, 4, Eigen::RowMajor> current_pose_matrix;
current_pose_matrix <<
        cur_pos[0], cur_pos[1], cur_pos[2], cur_pos[3],    // [3] -> x
        cur_pos[4], cur_pos[5], cur_pos[6], cur_pos[7],    // [7] -> y
        cur_pos[8], cur_pos[9], cur_pos[10], cur_pos[11],  //[11] -> z
        cur_pos[12], cur_pos[13], cur_pos[14], cur_pos[15];
//turns vector into matrix for easy use of matrix multiplication function

//====== Create Load Cell matrix =======//
Eigen::Matrix<float, 4, 4, Eigen::RowMajor> lc_matrix;
float sA = static_cast<float>(sin(RAD(loads_delta_converted[5])));
//Rz covert to alpha angle
float sB = static_cast<float>(sin(RAD(loads_delta_converted[4])));
//Ry covert to beta angle
float sG = static_cast<float>(sin(RAD(loads_delta_converted[3])));
//Rx covert to gamma angle
float cA = static_cast<float>(cos(RAD(loads_delta_converted[5])));
//Rz covert to alpha angle
float cB = static_cast<float>(cos(RAD(loads_delta_converted[4])));
//Ry covert to beta angle
float cG = static_cast<float>(cos(RAD(loads_delta_converted[3])));
//Rx covert to gamma angle
lc_matrix <<
        cA*cB, (cA*sB*sG) - (sA*cG), (cA*sB*cG) + (sA*sG), loads_delta_converted[0],
        sA*cB, (sA*sB*sG) + (cA*cG), (sA*sB*cG) - (cA*sG), loads_delta_converted[1],
        -sB, cB*sG, cB*cG, loads_delta_converted[2],
        0, 0, 0, 1;                //load cell T matrix for small corrections

//====== Matrix Multiplication To Base Coordinate System =====//
final_pose_matrix = current_pose_matrix * lc_matrix;
//result pose calculation, mutliplcation of current and load cell T matrix

//======== Convert Transform Calculation into Variant ========//
for (unsigned int i = 0; i < 16; ++i)
{
```

www.manaraa.com

```
        next_pose_vec[i] = final_pose_matrix((i / 4), (i % 4));  //assign result pose back to vector
}
vector<double> next_pose_vec_trans = MHPTranspose(next_pose_vec);
//transposes vector so can be sent to MHP using its conventions
variant_t next_pose_var = VectorToVariant(next_pose_vec_trans);
//converts vector to variant to be sent to MHP

//======= Moves platform/stores & displays current pose ======//
mhp->MoveMatrix(VARIANT_TRUE, L"Reamer", L"Reamer Zero", next_pose_var);
//moves the platform based on the matrix sent to it in absolute terms

//=============== Dot Product ===============//
point1 = point2;
point2 = point3;
point3 = { cur_pos[3], cur_pos[7], cur_pos[11] };
if (loopcount > 2 && hold == 'n')
{
        Vi = { point2[0] - point1[0], point2[1] - point1[1], point2[2] - point1[2] };
        Vf = { point3[0] - point2[0], point3[1] - point2[1], point3[2] - point2[2] };
        dot_product = (Vf[0] * Vi[0]) + (Vf[1] * Vi[1]) + (Vf[2] * Vi[2]);
        if (dot_product < 0)
        {
                dot_switch_count++;
        }       //cout << "\n" << dot_switch_count << "\n";
        if (dot_switch_count >= 2 && mhp->Moving)
        {
                break;
        }
}
if (_kbhit())  //checks if keyboard is hit
{
        int stop_char = _getch();
        if (stop_char == 27)
        {
                mhp->Stop();
                goto LABEL;  //exits program with ESC button press
        }
        if (stop_char == 32)
        {
                break;              //skips to next position with space bar press
        }
}                           //escape button press command
pos = mhp->GetPositionMatrix(PositionActual, L"Reamer", L"Reamer Zero");
//gets position of platform with respect to platform zero
pos_ = DoubleVariantToVector(pos);
//converts the get pos variant to vector, after the variant is converted from a array
current_pos_transpose = MHPTranspose(pos_);   //Transposes matrix  to conventional form
for (int r = 0; r <= 15; r++)
{
        current_and_dsr[r] = current_pos_transpose[r];
}
current_and_dsr[16] = loads_dsr[row][6];
current_and_dsr[17] = loads_dsr[row][7];
current_and_dsr[18] = loads_dsr[row][8];
all_poses.push_back(current_and_dsr);

//=============== Get Timestamp and store vector ==============//
timestamp = duration_cast< milliseconds >(
system_clock::now().time_since_epoch());
float time = timestamp.count();
all_timestamps.push_back(timestamp);
```

www.manaraa.com

```
                if ((loads_delta[0] < limits2[0][1] && loads_delta[0] > limits2[0][0]) &&
                   (loads_delta[1] < limits2[1][1] && loads_delta[1] > limits2[1][0]) &&
                   (loads_delta[2] < limits2[2][1] && loads_delta[2] > limits2[2][0]) &&
                   (loads_delta[3] < limits2[3][1] && loads_delta[3] > limits2[3][0]) &&
                   (loads_delta[4] < limits2[4][1] && loads_delta[4] > limits2[4][0]) &&
                   (loads_delta[5] < limits2[5][1] && loads_delta[5] > limits2[5][0]) && hold == 'n')
                   {
                      break;
                   }
            }
            catch (const _com_error& ex)
            {
                cout << "**************************  !!! OUT OF RANGE !!! **********************\n\n";
                for (int term = 0; term < 6; term++)
                {
                    loads_delta_converted[term] = loads_delta_converted[term] * 0.25;
                }
                if (_kbhit())
                {
                    int stop_char = _getch();
                    if (stop_char == 27)
                    {
                        mhp->Stop();
                        goto LABEL;         //exits program with ESC button press
                    }
                    if (stop_char == 32)
                    {
                        break;      //skips to next position with space bar press
                    }
                }

            }
        }
        loopcount = 0;
        dot_switch_count = 0;
}
```

www.manaraa.com

APPENDIX E: Additional Results from Chapter 4 Study

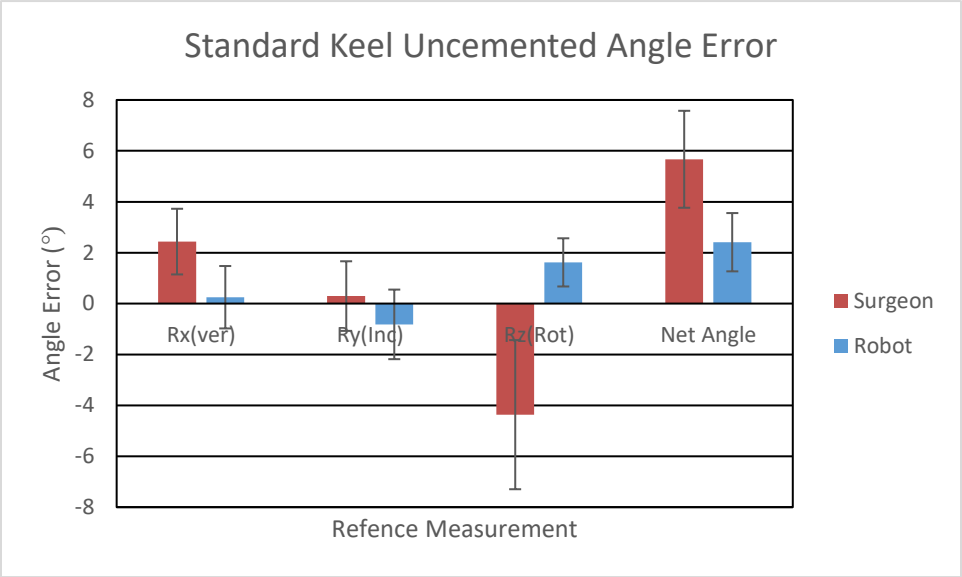

Figure E-1: Average angle error standard implant uncemented

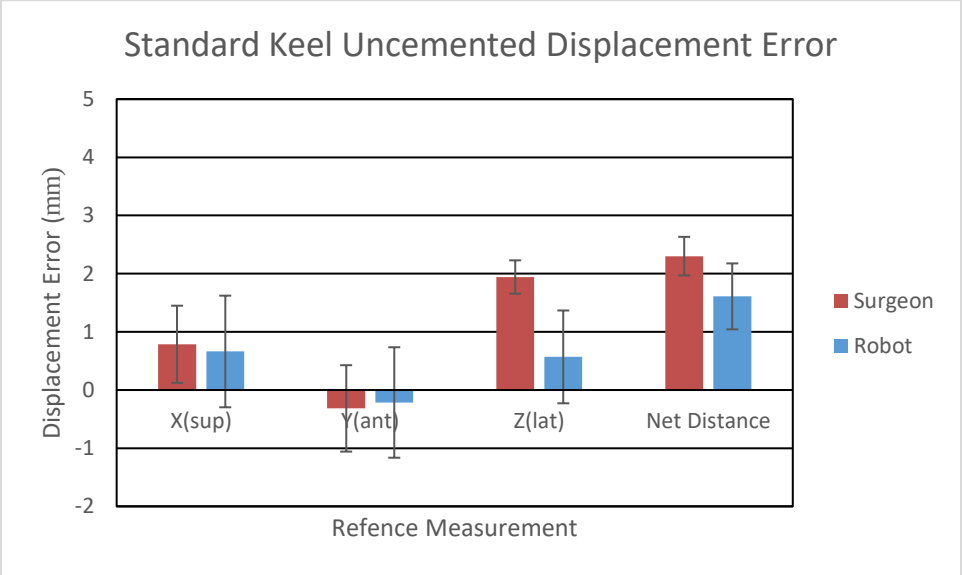

Figure E-2: Average displacement error standard implant uncemented

www.manaraa.com

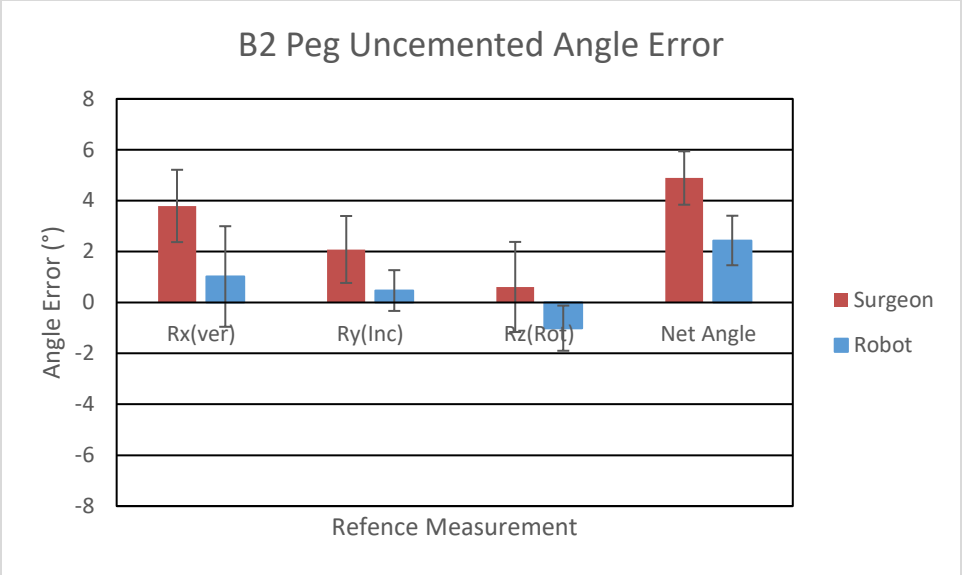

Figure E-3: Average angle error B2 implant uncemented

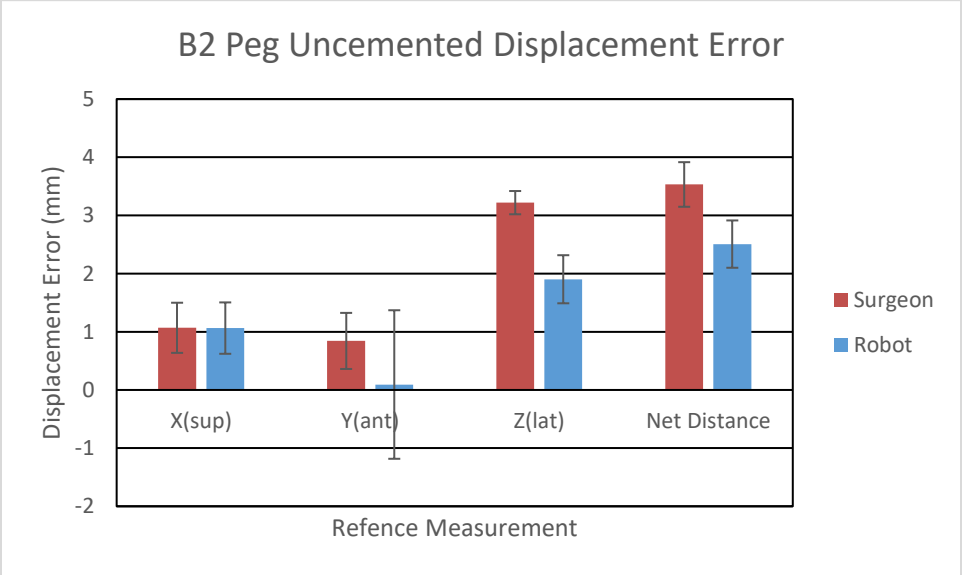

Figure E-4: Average displacement error B2 implant uncemented

www.manaraa.com

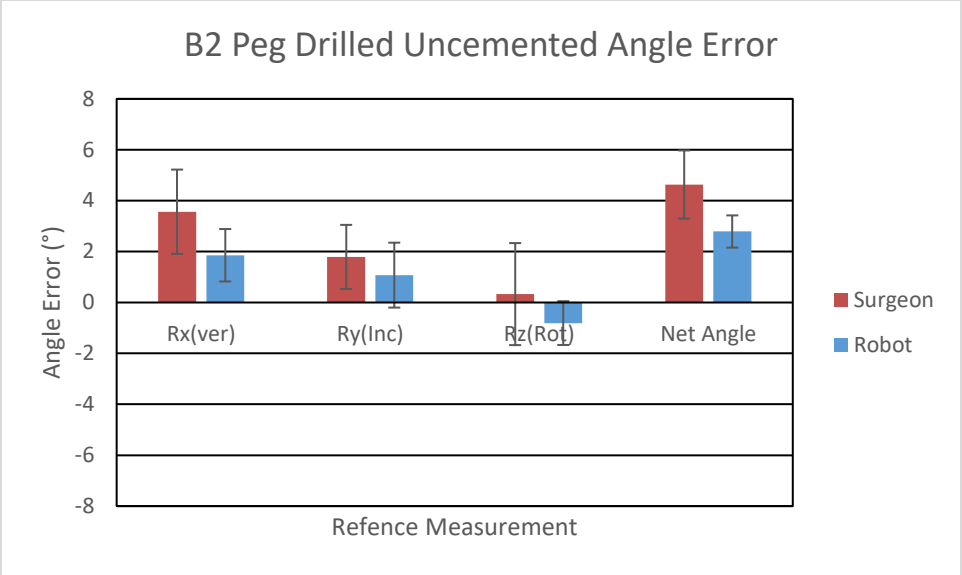

Figure E-5: Average angle error drilled B2 implant uncemented

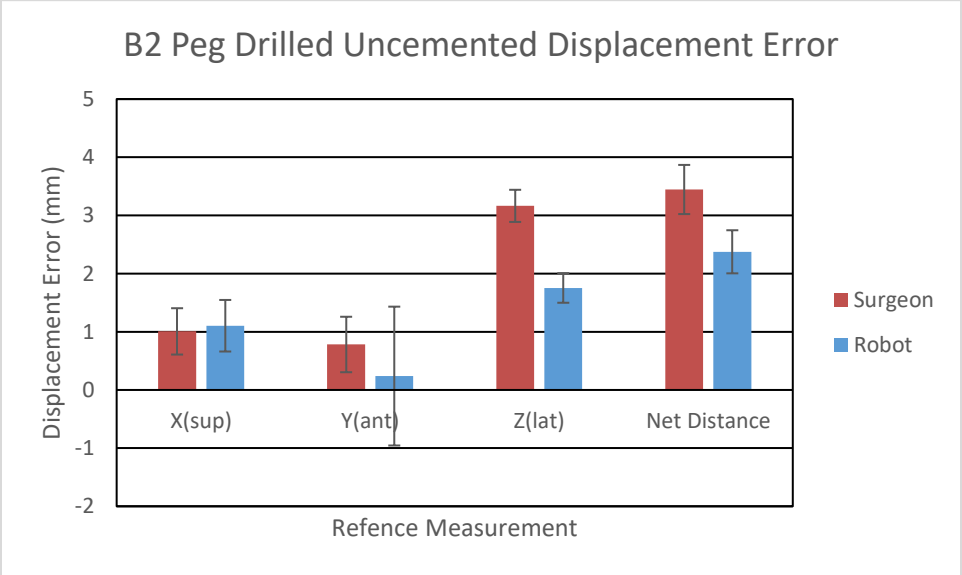

Figure E-6: Average displacement error drilled B2 uncemented

www.manaraa.com

Table E-1: Robot vs Surgeon Standard Uncemented MANOVA Test Results

Measure	Robot (I)	Surgeon (J)	Mean Difference (I-J)	Std. Error	Significance (p<0.05)*	95% Confidence Interval for Difference	
						Lower Bound	Upper Bound
Rx	1	2	-2.186	0.702	0.026*	-3.990	-0.382
	2	1	2.186	0.702	0.026*	0.382	3.990
Ry	1	2	-1.112	0.939	0.289	-3.525	1.300
	2	1	1.112	0.939	0.289	-1.300	3.525
Rz	1	2	5.984	1.441	0.009*	2.280	9.688
	2	1	-5.984	1.441	0.009*	-9.688	-2.280
Net Angle	1	2	-3.258	0.698	0.006*	-5.054	-1.463
	2	1	3.258	0.698	0.006*	1.463	5.054
X	1	2	-0.124	0.581	0.839	-1.618	1.369
	2	1	0.124	0.581	0.839	-1.369	1.618
Y	1	2	0.101	0.485	0.842	-1.145	1.347
	2	1	-0.101	0.485	0.842	-1.347	1.145
Z	1	2	-1.373	0.295	0.006*	-2.132	-0.615
	2	1	1.373	0.295	0.006*	0.615	2.132
Net Distance	1	2	-0.691	0.326	0.088	-1.530	0.148
	2	1	0.691	0.326	0.088	-0.148	1.530

Table E-2: Robot and Surgeon Standard Uncemented Implant T-Test

Measure	t	df	Significance (2-tailed) (p<0.05)*	Mean Difference	95% Confidence Interval of the Difference	
					Lower	Upper
Robot Rx	0.498	5	0.640	0.249	-1.037	1.535
Surgeon Rx	4.626	5	0.006*	2.435	1.082	3.789
Robot Ry	-1.466	5	0.203	-0.818	-2.252	0.617
Surgeon Ry	0.528	5	0.620	0.295	-1.140	1.730
Robot Rz	4.187	5	0.009*	1.619	0.625	2.612
Surgeon Rz	-3.650	5	0.015*	-4.365	-7.440	-1.291
Robot Net Angle	5.156	5	0.004*	2.411	1.209	3.613
Surgeon Net Angle	7.289	5	0.001*	5.670	3.670	7.669
Robot X	1.692	5	0.151	0.663	-0.344	1.670
Surgeon X	2.910	5	0.033*	0.787	0.092	1.482
Robot Y	-0.553	5	0.604	-0.215	-1.211	0.782
Surgeon Y	-1.042	5	0.345	-0.316	-1.095	0.463
Robot Z	1.748	5	0.141	0.569	-0.268	1.407
Surgeon Z	16.597	5	0.000*	1.942	1.642	2.243
Robot Net Distance	6.956	5	0.001*	1.610	1.015	2.204
Surgeon Net Distance	16.963	5	0.000*	2.301	1.952	2.649

www.manaraa.com

Table E-3: Robot vs Surgeon B2 Uncemented MANOVA Test Results

Measure	Robot (I)	Surgeon (J)	Mean Difference (I-J)	Std. Error	Significance (p<0.05)*	95% Confidence Interval for Difference	
						Lower Bound	Upper Bound
Rx	1	2	-2.773	0.957	0.034*	-5.233	-0.312
	2	1	2.773	0.957	0.034*	0.312	5.233
Ry	1	2	-1.614	0.654	0.057	-3.294	0.066
	2	1	1.614	0.654	0.057	-0.066	3.294
Rz	1	2	-1.619	0.865	0.120	-3.842	0.604
	2	1	1.619	0.865	0.120	-0.604	3.842
Net Angle	1	2	-2.455	0.772	0.025*	-4.439	-0.471
	2	1	2.455	0.772	0.025*	0.471	4.439
X	1	2	-0.005	0.236	0.983	-0.611	0.601
	2	1	0.005	0.236	0.983	-0.601	0.611
Y	1	2	-0.749	0.575	0.250	-2.229	0.73
	2	1	0.749	0.575	0.250	-0.73	2.229
Z	1	2	-1.317	0.196	0.001*	-1.82	-0.813
	2	1	1.317	0.196	0.001*	0.813	1.82
Net Distance	1	2	-1.025*	0.149	0.001*	-1.408	-0.642
	2	1	1.025*	0.149	0.001*	0.642	1.408

Table E-4: Robot and Surgeon B2 Uncemented Shoulder T-Test

Measure	t	df	Significance (2-tailed) (p<0.05)*	Mean Difference	95% Confidence Interval of the Difference	
					Lower	Upper
Robot Rx	1.266	5	0.261	1.022	-1.052	3.095
Surgeon Rx	6.540	5	0.001*	3.794	2.303	5.286
Robot Ry	1.438	5	0.210	0.470	-0.370	1.311
Surgeon Ry	3.880	5	0.012*	2.084	0.703	3.464
Robot Rz	-2.783	5	0.039*	-1.009	-1.940	-0.077
Surgeon Rz	0.845	5	0.437	0.611	-1.247	2.469
Robot Net Angle	6.138	5	0.002*	2.437	1.416	3.457
Surgeon Net Angle	11.420	5	0.000*	4.892	3.791	5.993
Robot X	5.896	5	0.002*	1.063	0.600	1.527
Surgeon X	6.074	5	0.002*	1.069	0.616	1.521
Robot Y	0.179	5	0.865	0.093	-1.247	1.433
Surgeon Y	4.281	5	0.008*	0.843	0.337	1.348
Robot Z	11.275	5	0.000*	1.903	1.469	2.337
Surgeon Z	39.456	5	0.000*	3.219	3.010	3.429
Robot Net Distance	15.095	5	0.000*	2.507	2.080	2.934
Surgeon Net Distance	22.572	5	0.000*	3.532	3.130	3.934

www.manaraa.com

Table E-5: Robot vs Surgeon Drilled Pegs B2 Uncemented MANOVA Test Results

Measure	Robot (I)	Surgeon (J)	Mean Difference (I-J)	Std. Error	Significance (p<0.05)*	95% Confidence Interval for Difference	
						Lower Bound	Upper Bound
Rx	1	2	-1.710	0.956	0.134	-4.168	0.748
	2	1	1.710	0.956	0.134	-0.748	4.168
Ry	1	2	-0.493	0.567	0.424	-1.950	0.964
	2	1	0.493	0.567	0.424	-0.964	1.950
Rz	1	2	-0.653	0.648	0.360	-2.318	1.012
	2	1	0.653	0.648	0.360	-1.012	2.318
Net Angle	1	2	-1.847	0.742	0.055	-3.756	0.062
	2	1	1.847	0.742	0.055	-0.062	3.756
X	1	2	0.097	0.229	0.689	-0.492	0.686
	2	1	-0.097	0.229	0.689	-0.686	0.492
Y	1	2	0.129	0.187	0.522	-0.352	0.610
	2	1	-0.129	0.187	0.522	-0.610	0.352
Z	1	2	-1.411	0.193	0.001*	-1.907	-0.915
	2	1	1.411	0.193	0.001*	0.915	1.907
Net Distance	1	2	-1.071	0.143	0.001*	-1.439	-0.703
	2	1	1.071	0.143	0.001*	0.703	1.439

Table E-6: Robot and Surgeon Drilled Pegs B2 Uncemented Shoulder T-Test

Measure	t	df	Significance (2-tailed) (p<0.05)*	Mean Difference	95% Confidence Interval of the Difference	
					Lower	Upper
Robot Rx	4.415	5	0.007*	1.857	0.776	2.938
Surgeon Rx	5.277	5	0.003*	3.567	1.829	5.305
Robot Ry	3.181	5	0.024*	1.297	0.249	2.345
Surgeon Ry	3.480	5	0.018*	1.790	0.468	3.113
Robot Rz	2.392	5	0.062	0.824	-0.062	1.709
Surgeon Rz	2.923	5	0.033*	1.477	0.178	2.775
Robot Net Angle	10.793	5	0.000*	2.790	2.125	3.454
Surgeon Net Angle	8.488	5	0.000*	4.637	3.233	6.041
Robot X	6.102	5	0.002*	1.104	0.639	1.569
Surgeon X	6.195	5	0.002*	1.007	0.589	1.424
Robot Y	3.160	5	0.025*	0.910	0.170	1.651
Surgeon Y	4.015	5	0.010*	0.782	0.281	1.282
Robot Z	16.868	5	0.000*	1.754	1.486	2.021
Surgeon Z	28.057	5	0.000*	3.165	2.875	3.454
Robot Net Distance	15.705	5	0.000*	2.375	1.986	2.764
Surgeon Net Distance	19.976	5	0.000*	3.446	3.003	3.889

المنارة للاستشارات
www.manaraa.com

Curriculum Vitae

COREY SMITH

EDUCATION

2015 – present **Candidate for MESc (Biomedical Engineering)**
Surgical Robotics Research, Expected: 2018
Supervisor: Dr. Louis Ferreira
The University of Western Ontario, London Canada

2011 – 2015 **BESc (Mechanical Engineering)**
Graduated with Distinction
The University of Western Ontario, London Canada

HONOURS AND AWARDS

2015 - 2016 **Western Graduate Research Scholarship**
The University of Western Ontario, London Canada

2014 **UWO In-Course Scholarships Year IV**
The University of Western Ontario, London Canada

2012 **UWO In-Course Scholarships Year II**
The University of Western Ontario, London Canada

2011- 2015 **Dean's Honour List**
The University of Western Ontario, London Canada

2011 - 2014 **Queen Elizabeth II Aiming for the Top Scholarship**
The University of Western Ontario, London Canada

2011 **The Western Scholarship of Excellence**
The University of Western Ontario, London Canada

2011 **The Ken Shea Memorial Scholarship**

RELATED WORK EXPERIENCE

2015 - 2017 **The University of Western Ontario, London Canada**
Teaching Assistant (Mechanics of Materials, Robotics and Automation Manufacturing, Introduction to Mechatronic Design)
Department of Mechanical and Materials Engineering
Department of Mechatronics Systems Engineering

2015 - 2017 **Dashwood Industries Inc., Centralia, Ontario**
Production Engineer in Training
The University of Western Ontario, London Canada

www.manaraa.com